Master program in
Nuclear physics

Master thesis

Inclusive J/ψ cross section in proton-proton collisions at $\sqrt{s} = 13$ TeV with ALICE

By: Ingrid McKibben Lofnes
Supervisor: Prof. Dieter Röhrich
Co-supervisor: Lucas Altenkämper

November 20, 2018

Abstract

This thesis describes the inclusive cross section measurement of the J/ψ meson in the di-electron channel measured at mid-rapidity in proton-proton collisions at the center-of-mass energy 13 TeV. The analyzed data sample includes all proton-proton data recorded by the ALICE detector during the period 2016 to 2017 and consists of 1.4 billion minimum bias events. The electron track selection relies on particle identification from the Time Projection Chamber in the ALICE central barrel. The raw J/ψ signal is extracted through bin counting in the signal window $2.92 \leq m_{\text{inv., e}^+\text{e}^-} \leq 3.16$ GeV/c^2 of the invariant mass spectrum after background subtraction. The background is estimated combining an invariant mass spectrum built from pairs from different events with an empirical fit. The obtained yield is corrected for the detector acceptance and efficiency determined from a Monte Carlo sample anchored to the corresponding data sample. The inclusive cross section is $\frac{\mathrm{d}\sigma}{\mathrm{d}y} = 9.46 \pm 0.28\,(\text{stat.}) \pm 0.43\,(\text{syst.}) \pm 0.48\,(\text{global})$ μb.

Acknowledgment

I would like to thank my supervisor Professor Dieter Röhrich for giving me the opportunity to work in such a good academic environment. Your courses on subatomic and heavy ion physics inspired me to continue deeper into this exciting field. Lucas Altenkämper, thank you for your patience with all my stupid and hopefully somewhat more intelligent questions throughout this whole analysis and for reading through my thesis. I am so grateful for all your help, both in understanding the physics and with all technical issues I've run into along the way. Ionut Arsene, your expertise and insightful comments have been very helpful. I am thankful for the opportunity to be a part of the Jpsi2ee physics working group and for all the feedback I have received from people in this group. I would like to thank my fellow master students, especially Simon Huiberts, for all our good discussions. A warm thanks to my parents for the willingness to discuss and proofread my thesis even though this is not even closely within your fields of expertise. To my wonderful husband, I would not have been able to finish this thesis without your constant encouragement and support. And to my darling daughter Karianne, thank you for every day reminding me of what are really the important things in life. I love seeing the world through your eyes, don't ever grow out of being curious.

I.M.L

Contents

List of Figures

List of Tables

Chapter 1

Introduction

The era of modern physics brought the need for increasingly higher accelerator energies and the Large Hadron Collider (LHC) [1] at the European Organization for Nuclear Research (CERN) operates at the highest center-of-mass energy ever achieved, $\sqrt{s} = 13$ TeV, and an instantaneous luminosity of 2.1×10^{34} cm^{-2} s^{-1} for proton-proton (pp) collisions. A further upgrade of the LHC energy and luminosity is scheduled, and starting in 2021, the LHC will run at the energy $\sqrt{s} = 14$ TeV and with an instantaneous luminosity of 3.0×10^{34} cm^{-2} s^{-1} [2]. The main goal of energetic, high luminosity accelerators has been to investigate physics of the standard model and beyond. A high center-of-mass energy makes it possible to create heavy particles, thereby increasing the possibility of discovering new particles. The amount of statistics that can be achieved is determined by the luminosity and is important in the search for rare signatures.

In addition to pp collisions, heavy ion collisions are also performed at the LHC. The main investigation in these collisions is the formation of the Quark-Gluon Plasma (QGP), a state of matter where quarks and gluons are deconfined, due to the asymptotic freedom of the strong interaction. Studying the formation of the QGP, gives deeper insight into Quantum Chromodynamics (QCD), the theory describing the strong interaction.

The J/ψ meson, a bound state consisting of a charm and an anti-charm, serves as an interesting probe in the study of the QGP, as it undergoes a suppression with respect to the production in pp collisions. Free color charges in the QGP break up the bound state, thus reducing the measured J/ψ yield. Hereby, the J/ψ measurements in pp collisions are important as a reference value to heavy ion measurements.

Also, the production mechanism for quarkonia, bound heavy quark and anti-quark states, is not fully understood even in pp collisions and the study of this is important for a basic understanding of the strong interaction. The J/ψ production mechanism involves relativistic and non-relativistic regimes, making it an interesting study of the interplay between non-perturbative and perturbative QCD. There are several leading models for quarkonium production, none of which are able to fully describe all experimental observables simultaneously. The J/ψ cross section is one of the most prominent observables. Other observables include the J/ψ polarization and J/ψ-hadron

correlation.

A Large Ion Collider Experiment (ALICE) is one of 4 large experiments at the LHC dedicated to the study of heavy ion collisions. As such, it is optimized for low p_{T} and high multiplicity measurements and provides great particle identification (PID) capabilities. This is beneficial for the J/ψ cross section measurement, as no extrapolation is needed for determining the total cross section.

The focus of this thesis is the measurement of the inclusive J/ψ cross section via the di-lepton channel. The following chapter provides an overview of the theoretical background, while chapter 3 describes quarkonium systems in detail. The experimental apparatus is described in chapter 4, with an emphasis on the subdetectors used in this analysis. Chapter 5 describes the J/ψ cross section analysis in detail, including a description of the analyzed data set, the signal extraction as well as acceptance and efficiency corrections. The calculation of systematic uncertainties is presented in chapter 6, followed by chapter 7 presenting the obtained results. The thesis concludes with a chapter discussing the outlook to future development.

Chapter 2

Theoretical background

Our current theoretical understanding of how the universe is built up is summed up in the Standard Model (SM), a theory describing three of the four fundamental forces in nature[1], as well as the basic building blocks of matter. The weak and electromagnetic interactions are described in the quantum field theory Quantum Electrodynamics (QED), while the strong force, responsible for holding nuclei and nucleons together, is described by the field theory QCD. The next section will present the theory of QCD and the formation of the QGP as a testing ground for a deeper understanding of the strong interaction.

2.1 Quantum Chromodynamics

QCD is a relativistic gauge field theory describing the strong interaction. Quarks, color charged particles, are bound together by the strong force into color-neutral hadrons. In analogy to QED, where the electromagnetic interaction is mediated by one chargeless photon, the strong interaction is mediated via the exchange of gluons. However, in contrast to QED, color charge can take one of three values, named red, green and blue. Gluons carry both color and anti-color charge, enabling the gluons to change the color charge of quarks. Furthermore, the gluons can interact with themselves, a phenomenon responsible for the QCD property named asymptotic freedom.

The gauge invariant Lagrangian of the QCD can be written as

$$\mathcal{L} = \bar{\psi}[i(\gamma^\mu D_\mu) - m]\psi - \frac{1}{4}G_{\mu\nu}G^{\mu\nu}, \tag{2.1}$$

where ψ represents the Dirac spinor of the quark field, m is the quark mass, D_μ is the covariant derivative ensuring gauge invariance for SU(3) transformations, and $G_{\mu\nu}$ represents the gluon field strength tensor, including the contributions from gluon self-interactions. The gluon self-interaction is described in theory by the non-commuting relation of the SU(3) generators, i.e. QCD is a non-Abelian gauge theory [3].

[1] Gravity, the interaction keeping planets in their orbit, is not yet incorporated in a unified theory.

The strong coupling constant α_s is encoded in the covariant derivative. In reality, the coupling constant is not a constant but depends on the energy scale of the interaction or, in other words, on the momentum transfer Q^2. The running, i.e. the energy scale dependence, of α_s is closely related to the concept of renormalization, a method used to treat infinities arising during calculations of the effect of self-interaction [3]. The energy dependence of α_s in terms of the momentum scale μ is expressed as

$$\alpha_s(Q^2) = \frac{\alpha_s\left(\mu^2\right)}{1 + B\alpha_s\left(\mu^2\right)\ln\left(\frac{Q^2}{\mu^2}\right)}, \tag{2.2}$$

where B depends on the number of quark and gluon loops. The number of quark flavors N_f and quark colors N_c enters the equation as

$$B = \frac{11N_c - 2N_f}{12\pi}. \tag{2.3}$$

For three quark colors and 6 possible flavors, α_s decreases with increasing Q^2, quite unlike the energy dependence of the QED coupling constant, which increases with increasing momentum transfer. The value of α_s is determined by experiment at a given energy scale. Figure 2.1 shows the energy dependence of α_s from measurements at the Compact Muon Solenoid experiment (CMS) together with the scale dependence of $\alpha_s\left(M_z\right)$ determined from a two-loop solution to the renormalization group equation [4].

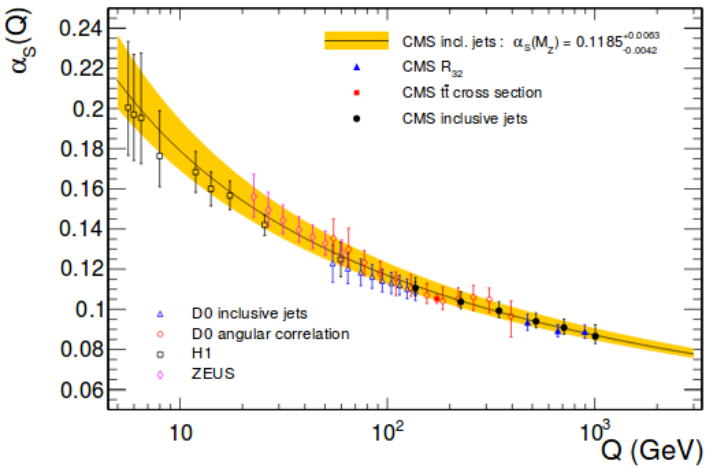

FIGURE 2.1: CMS measurements of α_s and the momentum scale dependence of $\alpha_s\left(M_z\right)$ using a two-loop renormalization group equation [4].

At large momentum transfers, or correspondingly small distances, the value of α_s becomes sufficiently small and QCD calculations can be done perturbatively. This is not possible at a low energy scale, where $\alpha_s \sim \mathcal{O}(1)$ and higher order contributions do not converge. In the non-perturbative energy regime, QCD calculations can be performed on a lattice of discretized space-time points [5].

The QCD potential for a bound quark-anti-quark state is given by the Cornell potential [6],

$$V = -\frac{4}{3}\frac{\alpha_s}{r} + kr, \tag{2.4}$$

which resembles the Coulomb potential at small distances r. For increasing distances, the linear term becomes dominant. This term originates from the experimental observation of quark confinement, i.e. the fact that colored objects are confined into color singlet states. Intuitively one can think of the interaction between two quarks as the exchange of virtual gluons, where the energy stored in the field is proportional to the separation distance. This resembles the forces in a rubber band, increasing as one pulls the ends apart. When trying to pull two quarks apart, the energy increases constantly until enough energy is present to create a new pair of quarks, combining the quarks into new hadrons. This process is called fragmentation or hadronization and is sketched in figure 2.2. Due to this, free quarks are never observed.

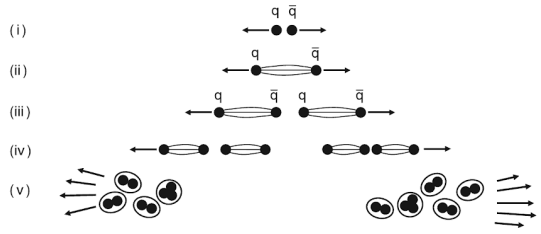

FIGURE 2.2: Qualitative picture of the steps in the hadronization process. [3]

Nevertheless, at very small distances, the quarks become quasi-free. Experiments show that at distances less than the size of hadrons, quarks seem to be moving freely. This is known as asymptotic freedom and figure 2.1 shows how the strong interaction weakens for increasing momentum transfer. David Gross, Frank Wilczek, and David Politzer were awarded the Nobel Prize in 2004 for their work predicting the asymptotic freedom [7, 8].

2.2 The Quark-Gluon Plasma

Heavy ion experiments at the Ring Imaging Cherenkov detector (RICH) at Brookhaven National Laboratory (BNL) and the LHC at CERN aim to create and characterize a deconfined state of matter, known as the QGP [9]. This is a hot and dense fireball, where quarks and gluons act as quasi-free particles.

2.2.1 Phase diagram of the QGP

The deconfinement of quarks and gluons requires a vanishing coupling constant which is achieved either by increasing the energy or by decreasing the distance between the confined constituents. Increasing the temperature T of the strongly interacting matter increases the energy, while an increased density will reduce the distance between the hadronic constituents, i.e. the quarks and gluons. The Hagedorn bootstrap model [10] proposed a maximum temperature for strongly interacting matter. Above this temperature, matter is no longer confined into color-neutral hadrons.

The phase diagram of strongly interacting matter in thermal equilibrium is shown in the left panel of figure 2.3. Strongly interacting matter can have different states characterized by its temperature and the baryon chemical potential μ_B which is related to the net baryon density. The phase diagram is only known schematically, with a crossover region and a critical point that has not yet been experimentally established [11]. At low T and μ_B, the matter is confined into hadrons. At higher temperatures a crossover into a deconfined and chirally restored matter takes place. At high chemical potential and low temperature, supposedly a color superconductor phase takes place, but no precise boundaries are known. At vanishing μ_B, Lattice QCD (LQCD) predictions are able to predict crossover temperatures ranging from $150 - 170$ MeV [12, 13].

A phase transition to the QGP was first observed by the Super Proton Synchrotron (SPS) at CERN, followed by experiments at Relativistic Heavy Ion Collider (RHIC) achieving a larger and hotter fireball [14–18]. Results from RHIC gave the surprising discovery that the QGP was not a gaseous state, but a nearly perfect liquid [17].

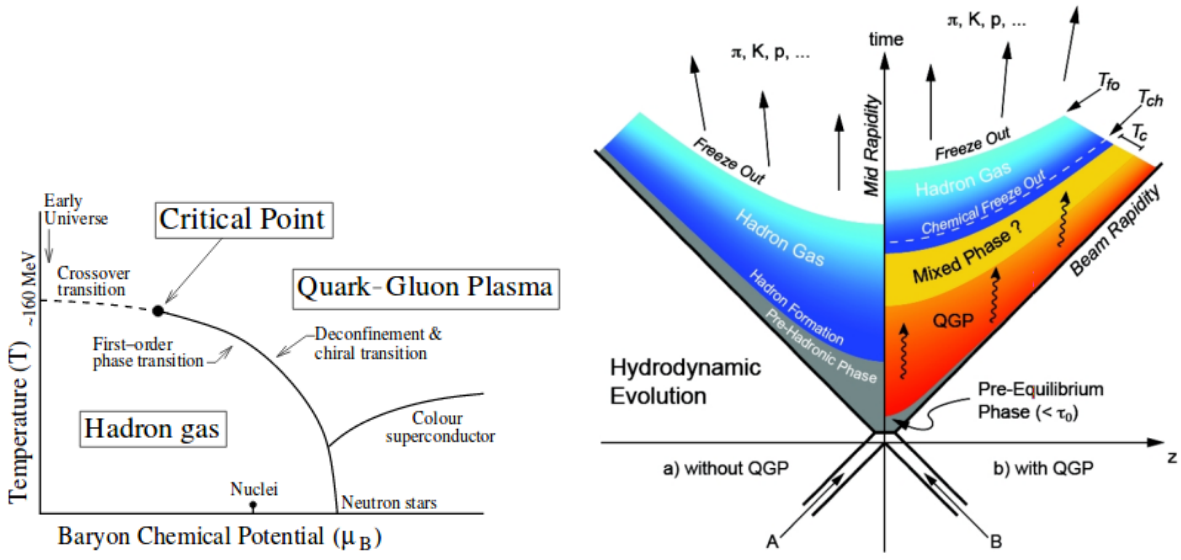

FIGURE 2.3: *Left*: The phase diagram of strongly interacting matter in thermal equilibrium [11]. *Right*: The space-time evolution of a collision, where the figure a shows the evolution without a QGP, and figure b shows the evolution with the QGP [19].

2.2.2 QGP evolution

The right panel of figure 2.3 shows the space-time evolution of a highly energetic collision, with and without the formation of the QGP, according to the Bjorken model [20]. Time is displayed along the y-axis and the spacial direction z along the x-axis. The initial collision happens at the origin, and if the temperature and energy density exceeds the critical value, the system evolves into a QGP. At low energies, the critical temperature for QGP formation is not reached, and the system undergoes a hydrodynamic evolution, where quarks and gluons are bound within hadrons, but formation of new hadrons is possible. High energy collisions, on the other hand, reach the critical temperature where the system can evolve into a QGP during a timescale of about 1 fm. During the pre-equilibrium phase, i.e. before the QGP formation takes place, direct photons, heavy quark pairs, and high p_{T} particles are produced. While the produced photons will traverse the medium unaffected, hadronic matter will undergo modifications, thus jets and high p_{T} particles can be studied as probes of the QGP. Due to the interaction of many partons, the system equilibrates into a deconfined state of matter, namely the QGP. Further, the internal pressure causes a rapid expansion. During this expansion, the temperature drops below the critical value, and the quasi-free quarks hadronize. The degrees of freedom are no longer the gluons and quarks, but the hadrons. This is called chemical freeze-out. The system continues to expand, and a kinetic freeze-out is reached when the mean distance between the interacting hadrons becomes larger than the range of the strong interaction. The phases of the QGP evolution do not necessarily have clear boundaries, and mixed phases can exist.

2.2.3 Signatures of the QGP

When studying the QGP, different key signatures indicating the creation of a fireball, are examined. Possible signatures of such a state include bulk properties of the medium, such as azimuthal asymmetry of the fireball, modification ("quenching") of jets and high p_{T}-particles passing through the medium, and the suppression of $Q\bar{Q}$ bound states created in the collision. This is not a complete list of possible signatures, but a small selection that will be described briefly in the following paragraphs.

Bulk properties: Two colliding nuclei, depending on their separation, will have an almond-shaped overlap in the plane perpendicular to the beam axis. The constituents of the system interact until a thermal equilibrium is reached after about 1 fm/c. The equilibrated system can be described by hydrodynamics with strong pressure gradients.

Jet modification: Two colliding partons carrying a significant fraction of the initial beam momentum will hadronize, emitting particles in a narrow cone around the direction of the parton momentum [21]. This is known as a jet. The hard partons are created at an early stage of the collision and can be used to probe the initial state of the QGP. A jet traversing the QGP will experience energy loss, due to gluon radiation and elastic scattering. The energy loss will depend on the path length. For back-to-back high p_{T} jets occurring close to the boundary of the QGP,

one of the jets will be greatly modified, due to a long path length through the medium, while the other will be hardly modified. Such an event shows a high p_{T}/energy leading jet accompanied by a suppressed jet signature on the away side.

Quarkonia suppression: Another key signature is the suppression of heavy quarkonia, such as the J/ψ, created during the pre-equilibrium phase. This is discussed in greater detail in chapter 3.4.

Chapter 3

Quarkonia

Quarkonia are bound states consisting of a heavy quark and an anti-quark. Hereby, bound $c\bar{c}$ states are referred to as charmonium, and bound $b\bar{b}$ states are called bottomonium. Since the lifetime of the top quark is smaller then the hadronization time, no $t\bar{t}$ states are formed.

The production of heavy quark pairs happens at an early stage of the collisions which further evolve into bound quarkonium states. These states are therefore good probes of the QGP. Due to the heavy quark mass, the quarkonium evolution is described using different non-relativistic approaches. A deeper understanding of the elementary production process in pp collisions is important, both as a reference value for heavy-ion collisions and for a basic understanding of QCD.

3.1 Quarkonia history

The first observed charmonium state was discovered in November 1974 by two separate groups at BNL [22] and Stanford Linear Accelerator Center (SLAC) [23]. The state, named J/ψ, became a revolution within the world of particle physics, as it confirmed the theoretical prediction of a fourth quark, the charm quark [24]. The detection of the first excited state, $\psi(2S)$ followed shortly after [25]. In 1976, representatives from BNL and SLAC were awarded the Nobel Prize for the discovery of the charm quark. The following year, a large resonance at 9.5 GeV/c^2 with a very broad width, was observed at Fermi National Accelerator Laboratory (FNAL), and determined to be several narrow resonances of the bottomonium system [26]. Due to its very heavy mass and thereby short lifetime, the top quark was not discovered until 1995 [27]. In order to form a quarkonium state, the lifetime of the quark constituents must exceed the QCD timescale $\Lambda_{\mathrm{QCD}}^{-1} \sim 10^{-23}$ s [28]. This is not the case for the top quark, which has a lifetime of $0.5 \cdot 10^{-24}$ s [29]. Therefore, no top quarkonium states are formed.

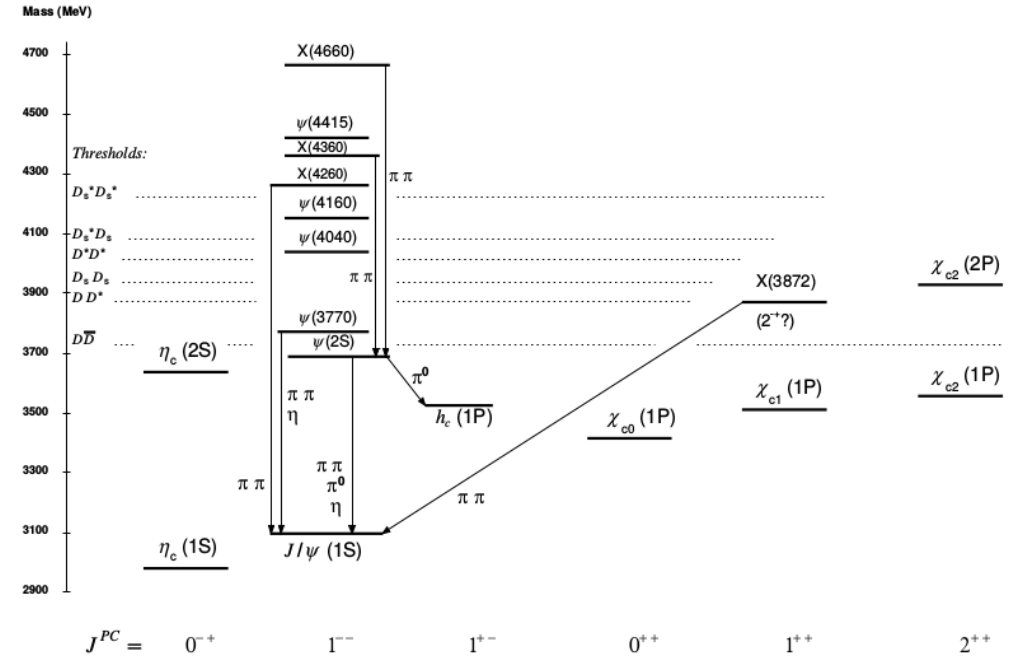

FIGURE 3.1: The level scheme of the $c\bar{c}$ bound states showing experimentally established states with solid lines. Figure from [29].

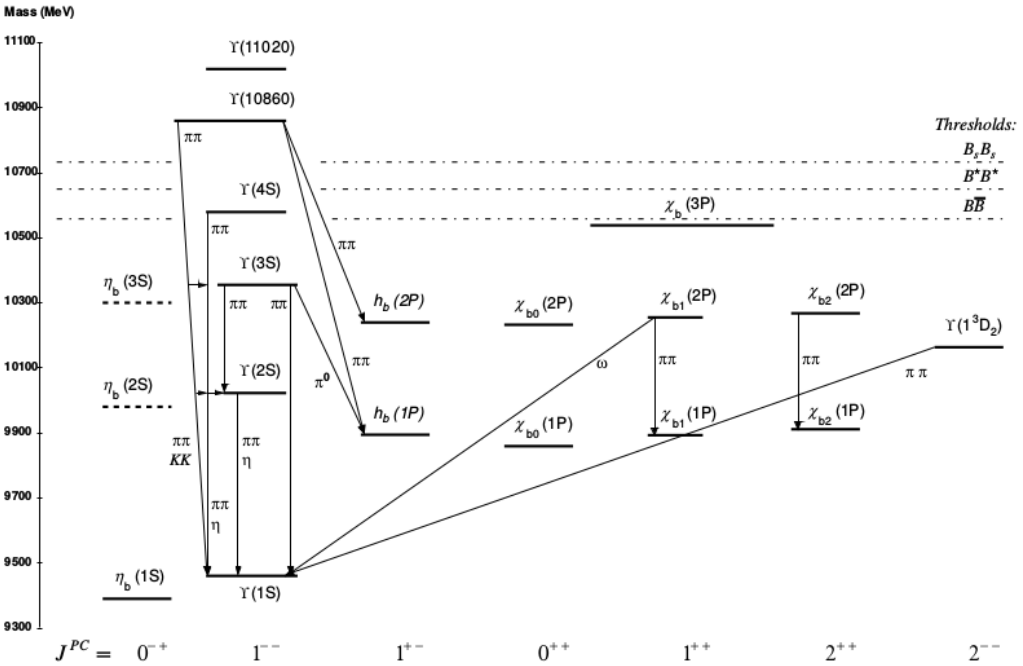

FIGURE 3.2: The level scheme of the $b\bar{b}$ bound states showing experimentally established states with solid lines. Figure from [29].

3.2 Properties of the J/ψ

The mass spectrum of the quarkonium systems can be predicted from the Cornell potential which is given by equation 2.4 as proposed in [30]. The different charmonium and bottomonium states are shown in figures 3.1 and 3.2, respectively.

The J/ψ is the s-wave orbital state of charmonia, with spin-1, odd parity, and zero charge. It is the spin-1 charmonium ground state, with a rest mass of 3.1 GeV [29]. The resonance width of the J/ψ is surprisingly narrow, indicating a relatively long lifetime. The mass of the J/ψ is below the open charm threshold, i.e. the mass required to form a pair of mesons consisting of a charm and a light quark, such as the D-mesons. Therefore the J/ψ must decay through $c\bar{c}$ annihilation. Due to the color-singlet state of the J/ψ, decays into hadrons cannot happen through a single gluon line. Additionally, the odd parity prevents decay through an even number of gluon lines. Thus, the strong decay of the J/ψ includes a minimum of three gluon lines, and the coupling becomes proportional to that of the electromagnetic decay channel. Therefore, the decay rate into leptons has a quite high branching ratio.

J/ψ created in collider experiments are typically separated into two categories: prompt-J/ψ denotes J/ψ mesons created through strong interaction in the initial collision or coming from the decay of other charmonium states, while J/ψ mesons decaying from B hadrons are referred to as non-prompt. The prompt J/ψ originate from the primary vertex within the available experimental resolution. The fraction of non-prompt J/ψ can be identified with a secondary vertex displaced from the primary one.

The charmonium production is dominated by gluon fusion at the TeV energy scale for transverse momenta $p_{\mathrm{T}} < 120$ GeV/c [31]. For the probed Bjorken-x range of 10^{-2} to 10^{-4} gluons dominate, thus gluon fusion is the Leading Order (LO) process. However, charm production has significant contributions from Next-to-Leading Order (NLO) $gg \to gg$ processes [32].

3.3 Quarkonium production

Due to the large mass of the heavy quarks, quarkonium production can be treated non-relativistically. The process happens at different dynamic scales and the interplay between the perturbative and non-perturbative regimes makes it an interesting study of QCD. The production happens in two steps, the creation of a $Q\bar{Q}$ pair, which then evolves into a bound state. The creation of such a heavy quark pair requires a large momentum transfer Q_{hard} meaning that the process happens at short distances $\frac{1}{Q_{\mathrm{hard}}}$. This short distance process can be calculated perturbatively.

The evolution of the quark pair into a bound state requires the relative momentum in the rest frame to be low compared to the quark mass so that the quarks are not separated and create open flavor mesons. Thus, the evolution is a long distance process which cannot be calculated

perturbatively. Figure 3.3 shows a sketch of the quarkonium production. Two partons with given parton distribution functions (PDF), collide in a hard scattering creating a heavy quark pair which can be calculated perturbatively. The quark pair then evolves through a soft process into a bound state H. The evolution is described by different models, represented by the non-relativistic QCD (NRQCD) factorization approach in this figure.

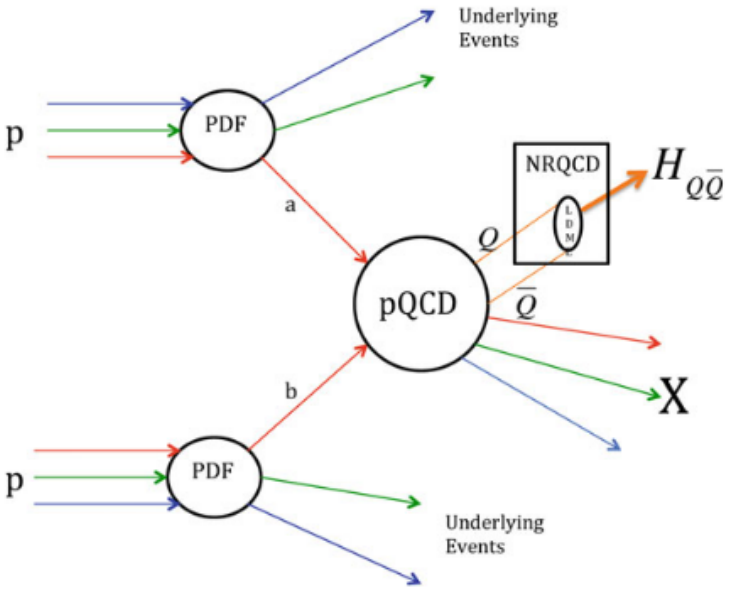

FIGURE 3.3: Illustration of the quarkonium production mechanism, where partons a and b collide with a large momentum transfer creating a heavy quark pair $Q\bar{Q}$ which evolves into a bound state H. The evolution is described by different effective models, here represented by NRQCD matrix elements. Graphics from [33].

For this intuitive picture of the quarkonium production to be a valid description of nature, one must be able to separate the perturbative and non-perturbative terms completely. This is done by factorizing the amplitude or cross section into a sum of products of infrared safe short-distance coefficients with well defined long-distance operator matrix elements [34]. The non-perturbative physics is thereby contained in the matrix elements and the coefficients are calculated perturbatively. Different theoretical models try to describe the non-perturbative evolution of the quark pair into a final bound color-singlet system. The most notable effective models are the Color-singlet model (CSM), the Color-evaporation model (CEM) and the NRQCD factorization approach. An overview of the models can be found in [34].

3.3.1 The Color-Singlet Model

In the color-singlet model the inclusive cross section is factorized into two separate parts in the following way:

$$\mathrm{d}\sigma\left(\mathscr{Q}+X\right)=d\widehat{\sigma}\left(Q\bar{Q}\left(1,{}^{L}S_{J}\right)+X\right)\left|R_{\mathscr{Q}}(0)\right|^{2}. \tag{3.1}$$

Here, $d\hat{\sigma}$ is the probability that a quark pair with quantum numbers L, S, and J (orbital angular momentum, spin, and total angular momentum, respectively) will be created, which can be calculated perturbatively. The CSM assumes that the initial quark pair does not change color or spin quantum numbers during the evolution into a bound quark system. As the final bound quarkonium is in a color-singlet state, this means that the initial quark also has to be in a color-singlet state. All non-perturbative effects are absorbed into universal wave function factors, $R_{\mathscr{Q}}(0)$. The wave functions may be determined from looking at decay processes in data or from potential models. The CMS was one of the early predictions for quarkonium production and described data at low energies quite well, but when confronted with data from TEVATRON [35], calculations at lowest order in α_s failed to describe the data, especially for $\psi(2S)$. The model has no relativistic corrections and does not include the possibility of the initial quark pair to be in a color-octet state. Furthermore, the leading contribution is gluon fusion [36,37]. Recently NLO and Next-to-Next-to Leading Order (NNLO) corrections have shown an improvement to the CSM predictions [34]. Figure 3.4 shows the p_{T} differential $\psi(2S)$ cross section together with NLO (black band) and NNLO (red band) calculations. The NNLO corrections are closer to the experimental values but do not fully describe the data.

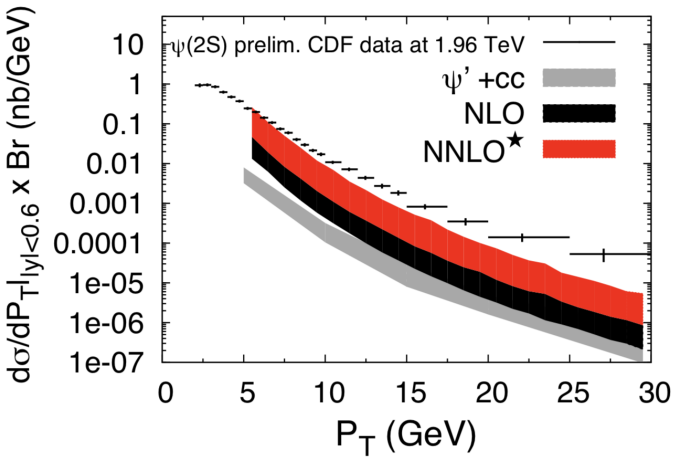

FIGURE 3.4: $\psi(2S)$ cross section measurements from TEVATRON together with NLO and NNLO calculations [38].

3.3.2 The Color Evaporation Model

In the CEM [32,34,37,39], the charmonium production is described by the same dynamics as the production of $D\bar{D}$, i.e. pairs of mesons containing one charm (anti-charm). The model predicts that all produced quark pairs with invariant mass lower than the threshold for producing open flavor mesons will form a bound quarkonium. The color state of the initial quark pair is arbitrary, unlike in the CSM. The color neutralization process happens through color evaporation from multiple soft gluon interactions during the non-perturbative evolution into a color-singlet bound quarkonium state. Color is treated in a statistical manner, and the probability for each possible

state can be obtained from SU(3) algebra [32]. The probability of the bound state to be a color-singlet is $\frac{1}{9}$. The cross section for a color-singlet state is thereby given as [37]:

$$\sigma_{\text{charmonium}} = \frac{1}{9}\int_{2m_Q}^{2m_{qQ}} dm \frac{d\sigma_{QQ}}{dm}, \tag{3.2}$$

where the total cross section of a quarkonium state, is found by integrating from the lower limit of twice the quark mass to the open flavor threshold. The probability for the quark pair to evolve into a quarkonium state H (e.g. J/ψ), is assumed to be constant f_H. The cross section for state H is then given as

$$\sigma_H = f_H \sigma_{\text{charmonium}}. \tag{3.3}$$

The constant f_H is independent of the production process as well as the energy and momentum. By comparing to data, f_H is fixed, and CEM can predict the momentum distribution of the quarkonium production rates [34]. The fit quality of f_H is generally poor, and CEM is unable to describe the observed variations for different production mechanisms, as f_H is process independent.

3.3.3 The NRQCD factorization approach

In the NRQCD factorization approach [34,40], the evolution into a bound state H is described by a non-relativistic quantum field, while the light quarks and gluons are described by relativistic QCD fields. Unlike the CSM, the NRQCD approach includes contributions from initial quark pairs in both color-singlet and color-octet states. It is an effective field theory, where the evolution of the initial quark pair into a bound state is treated non-relativistically due to the heavy quark mass. This formulation of QCD has a finite ultra-violet cutoff at the heavy quark mass, excluding the relativistic states. The relativistic state effects are then incorporated through the renormalization of the infinite number of coupling constant terms. The probability of the quark pair evolving into a bound quarkonium is expressed by matrix elements of NRQCD operators. The theory predicts an infinite number of matrix elements, but by expanding the elements in terms of the heavy quark velocity v the series can be truncated at a fixed order of v. This way only a few of the matrix elements remain, which are fixed from experimental data. The NRQCD formulation for the total cross section thus becomes an expansion of the strong coupling constant α_s and the heavy quark velocity v. It is formulated as a sum of products between coefficients which describe the hard scale physics and long distance matrix elements describing physics happening at a soft scale.

The cross section is given as:

$$\sigma(H) = \sum_n \sigma_n(\Lambda)\langle \mathscr{O}_n^H(\Lambda)\rangle, \tag{3.4}$$

where Λ is the ultra-violet cutoff and σ_n is the expansion in v of the $Q\bar{Q}$ cross section in quantum state n. $\langle \mathscr{O}_n^H(\Lambda)\rangle$ is the vacuum expectation values of the 4-fermion operators, which describes the transition into the bound state H.

The NRQCD approach is more successful in describing a more comprehensive set of cross section

measurement then the CSM and CEM. There are still some open questions about NRQCD, as the approach depends on the validity of truncating for higher orders of v, the possibility of calculating the quark pair cross section perturbatively, and the universality of the long-distance matrix elements [34]. Nevertheless, NRQCD predictions seem to agree well with experimental data.

Figure 3.5 shows the inclusive J/ψ cross section measurements through the di-muon decay channel in pp collisions at $\sqrt{s} = 13$ TeV detected by ALICE [41]. The left panel shows measurements compared to NRQCD predictions of prompt J/ψ in gray, NRQCD coupled to a Color Glass Condensate in blue, and a Fixed-Order-Next-to-Leading Logarithm (FONLL) calculation describing the non-prompt J/ψ. At higher p_{T} the NRQCD predictions of prompt J/ψ do not match the inclusive J/ψ measurements, explained by the increasing non-prompt contribution according to FONLL. The right panel shows a sum of the NRQCD and FONLL predictions, done separately for the low and high p_{T} predictions, obtaining a good description of the data.

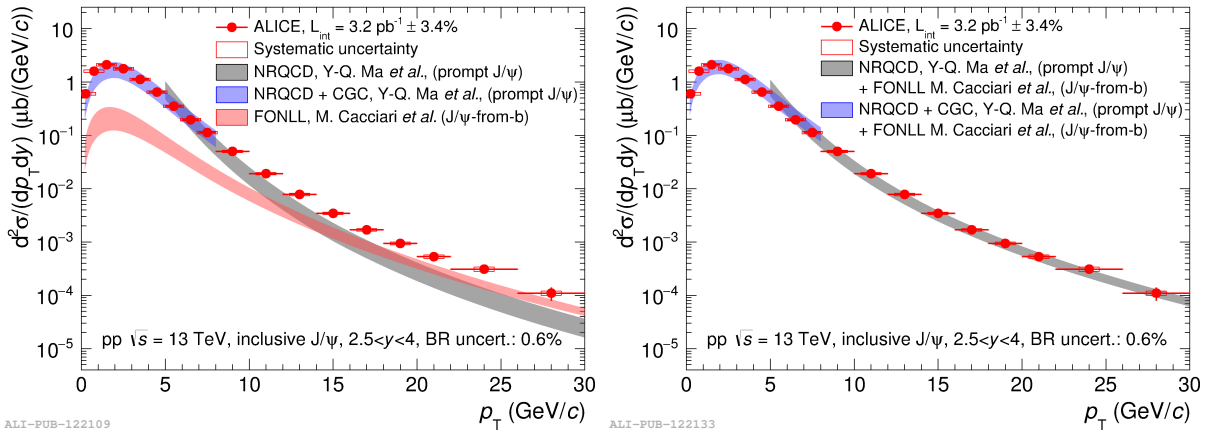

FIGURE 3.5: J/ψ differential cross sections (red circles) in pp collisions at $\sqrt{s} = 13$ TeV. *Left:* Measurements compared to NLO NRQCD (grey), LO NRQCD coupled with CGC (blue) and FONLL (red) *Right:* The non-prompt J/psi contribution estimated with FONLL is summed to the two calculations: NLO NRQCD (grey), LO NRQCD coupled with CGC (blue) for prompt J/psi production and compared to the same data [41].

3.3.4 Polarization

Quarkonium cross section measurements are important testing grounds for the effective production models. Another experimental observable is the polarization of quarkonium. The polarization is specified by three parameters, (λ_θ, $\lambda_{\lambda_\varphi}$, $\lambda_{\theta\varphi}$) corresponding to the decay amplitudes of the angular momentum states [42]. A polarization of (1,0,0) and (-1,0,0) corresponds to fully transverse and fully longitudinal polarization, respectively. Figure 3.6 shows ALICE measurements of the inclusive J/ψ polarization parameters in pp collisions at $\sqrt{s} = 8$ TeV together with NLO CMS and NRQCD predictions. The measurements are shown for two different frames of reference, namely the Collins-Sopher and Helicity frame. The CMS and NRQCD predictions have an opposite

p_{T} dependence for all polarization parameters in both frames. The polarization measurements show very little polarization, while the CMS predicts a longitudinal polarization and the NRQCD predicts a transverse polarization. Thus, neither of the polarization predictions describe the data very well.

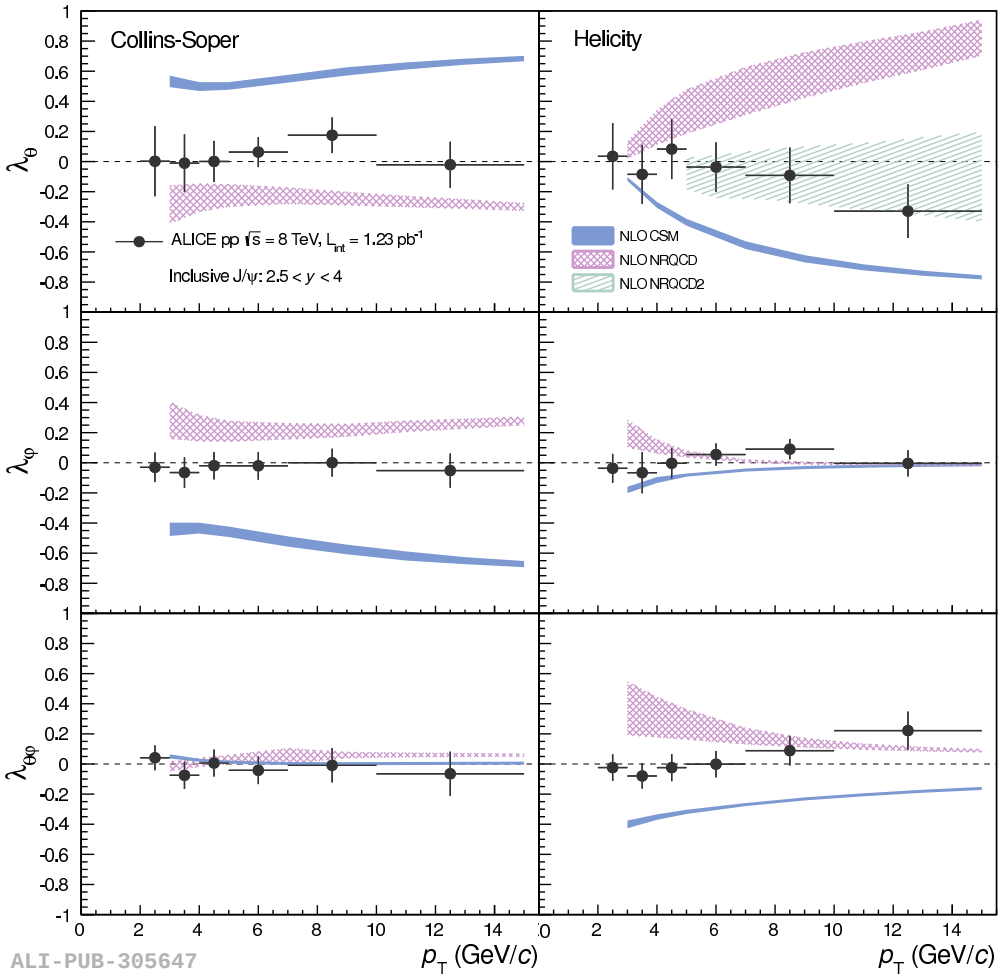

FIGURE 3.6: Inclusive J/ψ polarization parameters in pp collisions at $\sqrt{s} = 8$ TeV (black points, error bars represent the total uncertainties) compared with model predictions: NLO CSM (blue filled bands), NRQCD (red shaded bands) and NRQCD2 (light blue hatched band). Left and right plots show the results in the Collins-Soper and helicity frames, respectively, for λ_θ (top plots), λ_φ (middle plots) and $\lambda_{\theta\varphi}$ (bottom plots) [42].

3.4 Quarkonia as probes of the QGP

The creation of heavy quark pairs requires a hard process and therefore happens during the pre-equilibrium phase of heavy ion collisions. Therefore, quarkonia can serve as probes of the QGP.

When a hot, deconfined medium is produced, the quarkonia yield is modified. A color screening, analogous to the Debye screening of an electromagnetic field in a plasma, was first proposed by T. Matsui and H. Satz [43]. The general idea was that the high amount of gluons and free color charges would break up the bound $Q\bar{Q}$ states, thus reducing the number of detected quarkonia. The quarkonium potential in the presence of the QGP is given as,

$$V_{Q\bar{Q}}(r,T) \sim -\frac{4}{3}\frac{\alpha_s}{r}e^{-r/\lambda_D(T)}, \tag{3.5}$$

where r is the quarkonium binding radius and $\lambda_D(T)$ is the Debye length, which depends on the temperature of the plasma. The screening will only effect quarkonium states with a binding radius larger than the Debye length. Thus, the screening effect is both temperature sensitive and depends on the quarkonium size, causing a sequential disappearance of the quarkonium states. Hence the melting of quarkonia can be used as a "thermometer" of the QGP [44].

During the chemical freezeout, the quarks will arbitrarily recombine with neighboring quarks, as shown in the top part of figure 3.7a. For a hotter medium, the number of heavy quarks present in the deconfined matter increases, increasing the likelihood for statistical recombination of a quarkonium state. An enhancement of quarkonium production at the LHC energies with respect to RHIC energies was proposed around 2000, due to additional charmonium production, either through statistical production at the phase boundary or through coalescence of heavy quarks in the plasma [21]. This is sketched in the lower part of figure 3.7a.

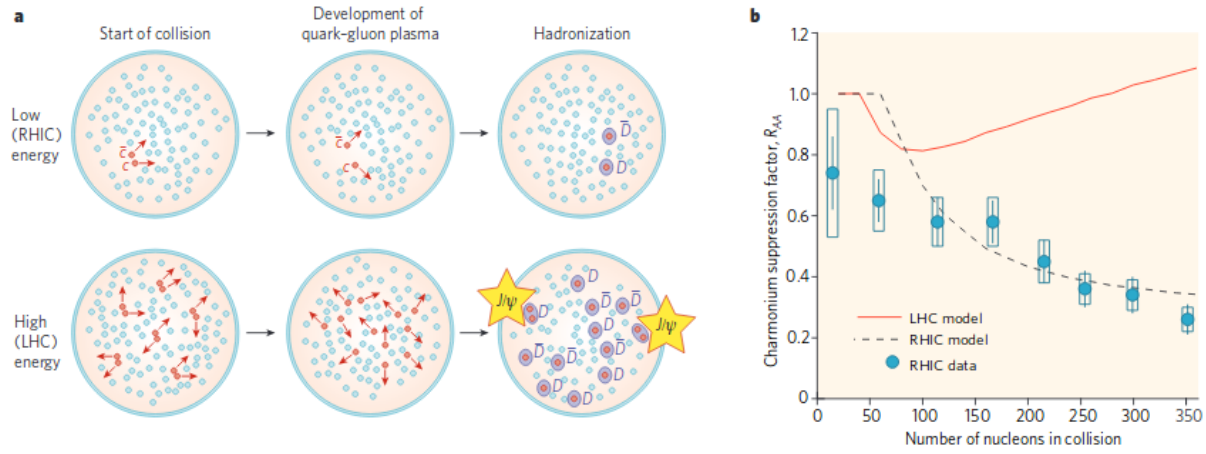

FIGURE 3.7: *Left:* Illustration of the color screening effects at low and high collision energies. At low energies, the QGP screens the interaction between the created charm pair (red dots) and the charm quarks hadronize into open flavor mesons (purple circles). At higher energies, more charm pairs are produced, and the probability for a charm and anti-charm to combine into a J/ψ (yellow stars) increases. *Right:* The charmonium suppression factor of RHIC data together with models of RHIC suppression (dotted line) and proposed LHC enhancement in red. Graphics from [21].

To quantify the modification of the quarkonium yield, the nuclear modification factor R_{AA} is used. This is the ratio of A–A collision spectrum to the pp collision spectrum, scaled by the number of

binary collisions,

$$R_{AA} = \frac{\text{Yield}_{\text{AA}}}{\langle N_{\text{coll.}} \rangle \text{Yield}_{\text{pp}}}. \tag{3.6}$$

An R_{AA} value less then 1 indicates suppression of the yield with respect to the pp collisions and a value greater than 1 points to enhancement. Thus, pp cross section measurements serve as a baseline for measured nuclear modification in A–A collisions.

Figure 3.7b shows the R_{AA} of measured charmonium at RHIC together with the proposed enhancement model for LHC energies in red. A clear charmonium suppression can be seen in the RHIC data. Figure 3.8 shows the inclusive J/ψ R_{AA} measured with ALICE in Xe–Xe (red) and Pb–Pb (blue) collisions at $\sqrt{s_{\text{NN}}} = 5.44$ TeV and $\sqrt{s_{\text{NN}}} = 5.02$ TeV, respectively. The measurements are compared to the J/ψ R_{AA} measured by Pioneering High Energy Nuclear Interactions eXperiment (PHENIX) in Au–Au collisions at $\sqrt{s_{\text{NN}}} = 0.2$ TeV. The low energy measurements from PHENIX show a large suppression, while the suppression is less at LHC energies due to regeneration.

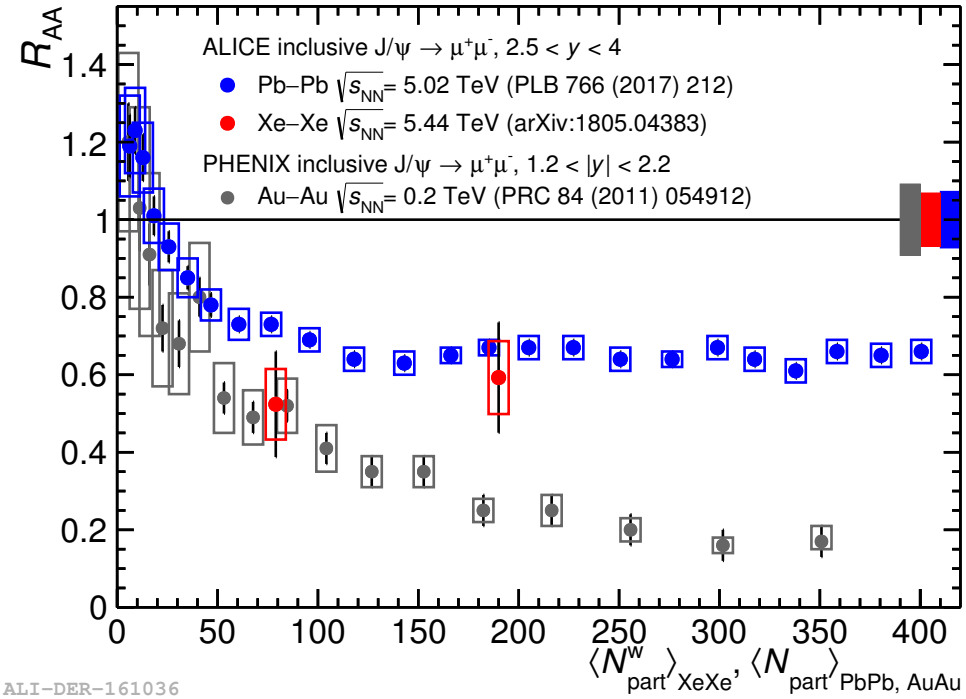

FIGURE 3.8: Inclusive J/ψ R_{AA} as a function of centrality in Xe–Xe and Pb–Pb. Results are compared to the J/ψ R_{AA} measured by PHENIX. The figure is derived from [45–47].

Chapter 4

Experimental setup

In this chapter, the Large Hadron Collider (LHC) and the ALICE detector system will be presented. The LHC will be described with a focus on proton-proton runs, and thereafter the ALICE detector-system will be introduced. The main focus will be on the sub-detectors relevant for this analysis.

4.1 The Large Hadron Collider

The LHC [48] is a circular particle accelerator, aka synchrotron, placed underground at the French-Swiss border, near Geneva, Switzerland. The accelerator has a circumference of 26.7 km, containing two separate beam pipes allowing for beams circulating clock- and counter-clockwise. Beam particles are accelerated in opposite direction and are brought to collision at dedicated interaction points. There are four collision points along the LHC, where experimental data is collected, in addition to several smaller experimental sites. Figure 4.1 shows an overview of the LHC and the different experimental sites. The LHC is designed to accelerate protons to beam energies of up to 7 TeV, which translates into a center-of-mass energy of $\sqrt{s} = 14$ TeV. Currently, the accelerator is operating with the center-of-mass energy of $\sqrt{s} = 13$ TeV. The LHC also performs lead-lead beams at $\sqrt{s_{\mathrm{NN}}} = 5.02$ TeV, and proton-lead beams at $\sqrt{s} = 8.16$ TeV. When searching for rare processes, such as the creation of J/ψ mesons investigated in this thesis, the level of statistics that can be achieved is important. This is determined by the luminosity, proportional to the number of events per second. The LHC proton beam is divided into high-intensity bunches with $1.15 \cdot 10^{11}$ protons in each bunch [49]. The bunches have a nominal spacing of 25 ns, with a maximum 2808 bunches per ring.

The four large experimental sites along the LHC are ALICE [1], A Toroidal LHC Apparatus (ATLAS) [50], CMS [51] and the LHC beauty experiment (LHCb) [52]. ATLAS and CMS are multipurpose experiments, studying a vast range of physics. Both detectors have a large phase space coverage and are constructed to handle the high luminosities delivered by the LHC. The experiments are ideal for studying rare processes. One of the big discoveries from these experiments

was the Higgs boson, announced in July 2012 [53, 54]. LHCb is a low luminosity experiment, mainly focused on bottom quark physics. Measurements such as CP-violation and looking for rare B hadron decays are performed. ALICE is dedicated to heavy ion collisions, exploring the QGP and QCD properties.

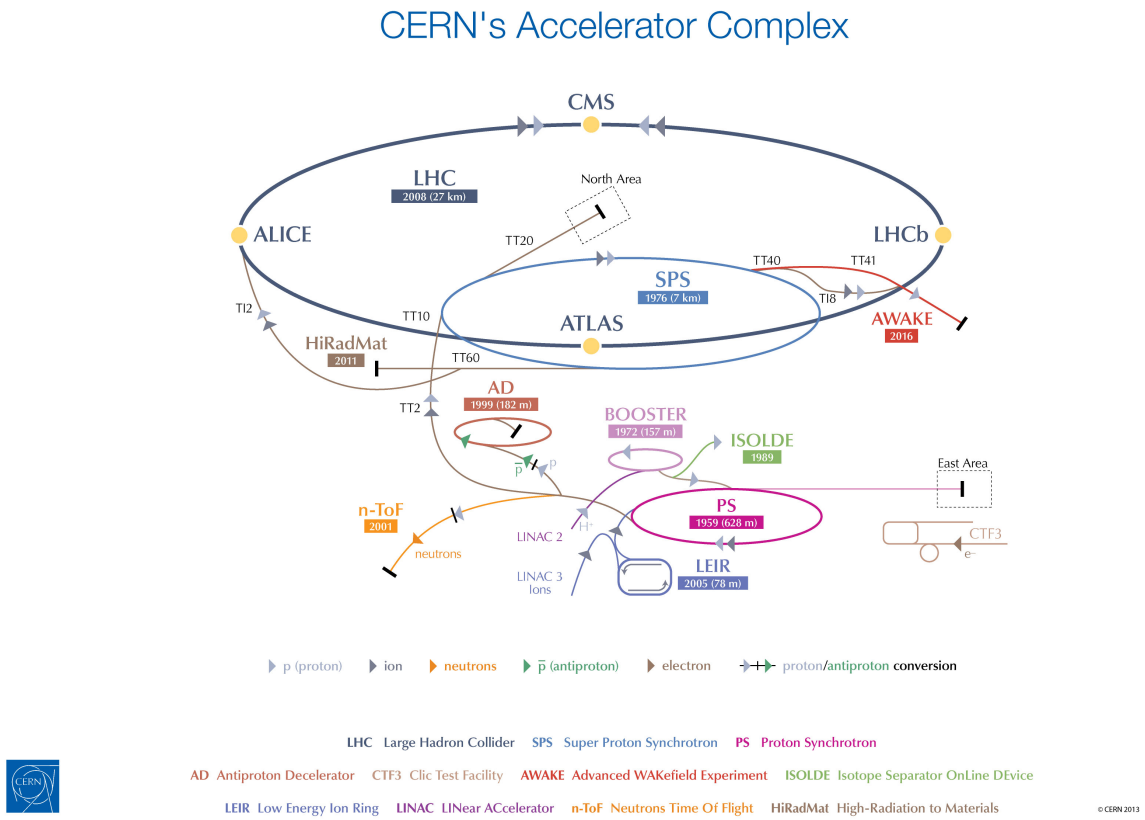

FIGURE 4.1: The LHC and different experimental sites. Graphics from [55].

4.2 The ALICE detector

A Large Ion Collider Experiment (ALICE) [1] is a detector dedicated to the study of heavy ion collisions at the LHC. Therefore, the detector is specifically designed to handle high multiplicity events, with good PID and tracking down to low momenta. To fully study these events, identifying the different particles is important, and ALICE makes use of a variety of PID methods, such as determining the particles specific energy loss, time of flight, transition and Cherenkov radiation. In addition, the Electromagnetic Calorimeter (EMCal), muon filters, and topological decay reconstruction can be used to determine particle species.

ALICE also collects data from pp collisions but does not match triggering at the ATLAS, CMS, and LHCb interaction rate. This is due to the main tracking device, the TPC, with a drifting time window of about 100 μs [56]. However, the ALICE detector is ideal for identifying a vast number of particles. At mid-rapidity, the bulk of produced particles has a transverse momentum less than 1 GeV/c, and ALICE is capable of performing measurements down to very low p_{T}, also at mid-rapidity [57]. ALICE provides good PID for transverse momentum ranging from 0.1 GeV/c to 20 GeV/c [56, 57].

All the major LHC experiments perform charmonium measurements. The ATLAS and CMS designs are optimal for the dimuon channel, as the detectors have a large acceptance for the muons. Due to the large magnetic field covering the central region of ATLAS and CMS, triggering at mid-rapidity is only efficient down to 7 GeV/c for the dilepton channel [31]. The ALICE experiment measures charmonium both at forward- and mid-rapidity, making use of the detectors well performing PID and low momentum measurement capabilities. At mid-rapidity the dielectron channel of the J/ψ is measured, making use of PID from the energy loss, and measurements down to $p_{\mathrm{T}} = 0$ are possible.

The ALICE detector, shown in figure 4.2, contains 18 different detector systems allowing the study of hadrons, electrons, muons, and photons created in the collisions. The detectors can be divided into the central barrel detectors, the forward detectors, and the muon spectrometer. The central barrel contains the Inner Tracking System (ITS), a six-layer silicon detector, surrounded by the cylindrical TPC, the Transition Radiation Detector (TRD), used for identifying electrons, and the Time-Of-Flight detector (TOF) system, discriminating between light and heavy particles using the particles flight time. These detectors have a $|\eta| < 0.9$ coverage, apart from the TRD covering $|\eta| < 0.8$. The central barrel also includes the High Momentum Particle Identification Detector (HMPID) Cherenkov detectors, and the electromagnetic calorimeters, the Photon Spectrometer (PHOS), EMCal and Di-jet Calorimeter (DCal), having slightly smaller pseudorapidity ranges of $|\eta| < 0.6$, 0.12, 0.7 and 0.7, respectively. The detectors in the central barrel are surrounded by a solenoid giving a magnetic field of 0.5 T. The magnetic field gives charged particle tracks a curvature and this can be used to identify particle momenta and charge. Situated atop the central barrel is the ALICE cosmic ray detector (ACORDE), triggering on cosmic rays.

The muons are detected by the forward muon spectrometer, covering a rapidity range of $-4.0 < \eta < -2.5$ [1]. The spectrometer consists of absorbers limiting the hadronic background, a dipole magnet providing a nominal field of 0.7 T, and tracking and triggering chambers. The tracking chambers provide a spatial resolution of 100 μm. There are 5 tracking stations, each with two chamber planes consisting of two cathode planes, thus providing two-dimensional hit information.

Along the beam line, several smaller detectors, such as the Zero Degree Calorimeter (ZDC), the Photon Multiplicity Detector (PMD), the Forward Multiplicity Detector (FMD), the Timing and Trigger detector at ALICE (TZERO), and the VZERO (V0) are situated. These detectors are used for event characterization and triggering.

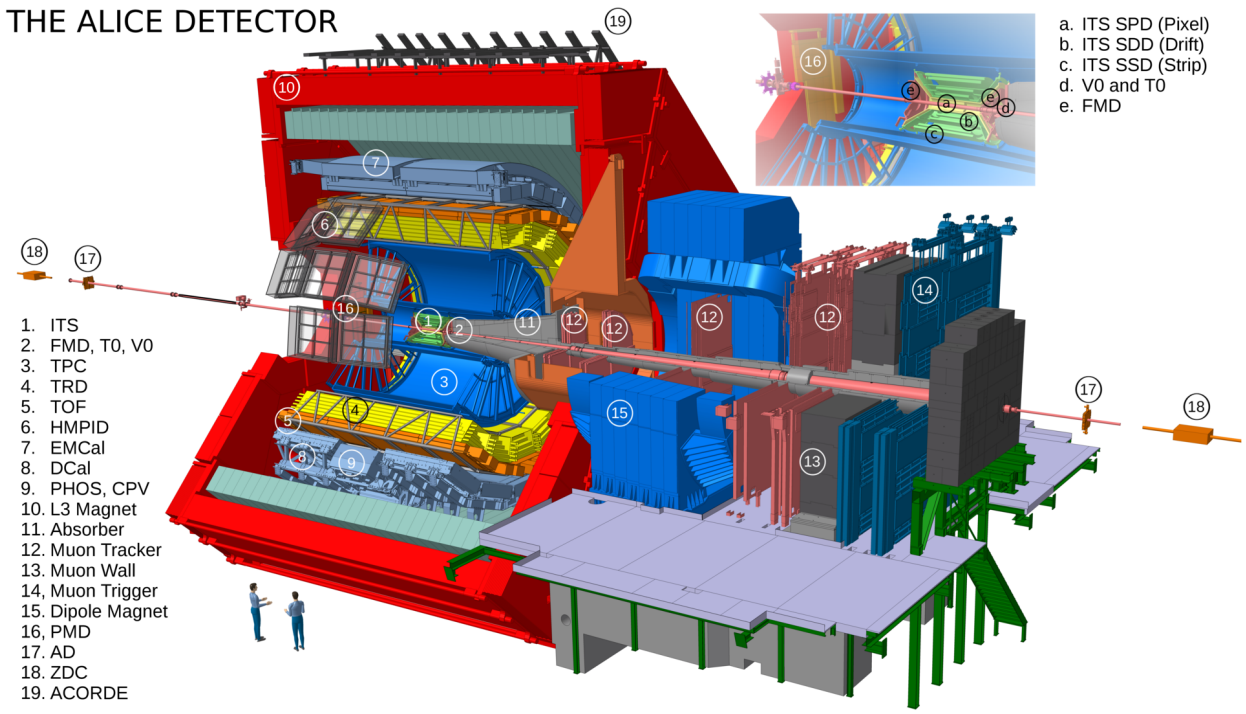

FIGURE 4.2: Schematic overview of the ALICE detector, and its subsystems. Figure from [58].

The Inner Tracking System (ITS) [1] is a six-layer pixel detector with the main purpose of reconstructing the primary vertex with a resolution better than 100 μm and secondary vertices. The ITS also improves the momentum and angle resolution for tracks reconstructed with the other detectors. For pions with p_{T} between 0.1 GeV/c and 3 GeV/c, the detector provides a relative momentum resolution better than 2%.

To minimize electrons from gamma conversions, the material budget for the inner layers is as low as 7.66% of the radiation length[1]. The six pixel layers exploit three different pad designs. The two innermost layers are Silicon Pixel Detectors (SPD), with high precision and granularity. The detectors determine the position of the primary vertex as well as the impact parameter of secondary tracks from weak decays. In order to cope with the high particle densities expected in heavy ion collisions, the two middle layers are Silicon Drift Detectors (SDD), with good multitrack capabilities. The two outer layers consist of Silicon Strip Detectors (SSD), which together with the SDD layers contribute to the identification of particles, based on the measured energy deposition.

For the measurements performed in this analysis, a requirement of track points from the ITS suppresses the background contamination from photon conversions occurring in the ITS material [31].

[1]The radiation length is the characteristic amount of matter high-energy photons (or electrons) traverse losing energy through pair production (bremsstrahlung) [29]

The Time-Projection Chamber (TPC) [1] is a cylindrical, ionization chamber situated around the ITS. It is the main tracking detector in ALICE, with both tracking and PID capabilities. The detector covers a 90 m^3 volume with a radius ranging from 85 cm up to 250 cm and extending 500 cm along the beam line. This results in a full coverage of the azimuthal angle and the pseudorapidity range of $|\eta| < 0.9$. The TPC is filled with a gas mixture of Ar (90%) and CO_2 (10%). The field cage is divided by a central electrode providing an electrical field gradient of 400 V/m. Charged particles traveling through the gaseous volume will ionize the gas along its path, resulting in free electrons drifting towards the endcaps with a maximum drift time of 92 μs. Both endcaps consist of multi-wire-proportional chambers (MWPC), divided into 18 sectors covering the full azimuthal angle. Electrons drifting through the gas, create an avalanche, amplifying the signal read out by the MWPC. Tracks for particles traveling through the TPC are reconstructed from three-dimensional space-time points determined from the readout position and the cluster drift time. The curvature of the reconstructed tracks in the transverse plane is used to determine the transverse momentum. At low momentum, the track curvature becomes strong, limiting the radial distance traversed in the TPC. The TPC delivers good momentum resolution in the p_{T} range 0.1 - 100 GeV/c.

In addition to being the main tracking device, the TPC also performs PID based on the specific energy loss of traversing charged particles. A maximum of 159 pad rows crossed by charged particles, permits a precise measurement of the deposited energy loss. This is further described in section 4.4.

The VZERO (V0) [1] detectors are situated up- and down-stream of the interaction point, at 3.3 m and 0.9 m from the nominal vertex $z = 0$. The two detectors, V0A and V0C, consist of scintillator counters, with the main purpose of triggering for Minimum Bias (MB) events and as a centrality trigger for lead-lead collisions. The V0 detectors also provide an estimation of the event plane. The detectors have limited pseudorapidity coverage of $2.8 < |\eta| < 5.1$ and $3.7 < |\eta| < -1.7$ for the V0A and V0C, respectively.

The V0 detector triggers on the coincidence of signal in V0A and V0C, further referred to as V0AND. In addition to MB event and centrality triggering, the V0 is used for rejecting beam-gas events and used when determining the luminosity.

4.3 Track reconstruction with ALICE

The first step when reconstructing particle tracks in the central barrel is a preliminary determination of the interaction vertex [56]. This is done using a linear extrapolation of hit pairs in the two innermost ITS layers, namely the SPD layers. Tracks are then reconstructed through a Kalman filter algorithm, with an inward-outward-inward scheme. Starting at the outer edge of the TPC and moving inwards, tracks are found by combining clusters. This is done with and without the constraint of the track points pointing to the preliminary vertex. The TPC tracks are then used

as seeds for the track finding in the ITS, relying on the same track reconstruction algorithm. Furthermore, the Kalman filter approach is reversed, using the combination of ITS and TPC tracks as seeds for an outward propagation. The outward track matching is continued out in an attempt to match tracks reaching the TRD and TOF. Finally, an inward refitting of the reconstructed tracks is performed, starting at the outer edge of the TPC. The refitting is done, both with and without the assumption of tracks pointing to the interaction vertex. Tracks where the refitting procedure successfully followed the track through the ITS and TPC are labeled $\mathrm{ITS_{refit}}$ and $\mathrm{TPC_{refit}}$, respectively. After the final track reconstruction, the interaction vertex is determined with a higher precision using the global track information, i.e. the ITS and TPC track reconstruction.

4.4 Particle identification with the TPC

The particle identification performed with ALICE exploits a variety of subdetectors and PID techniques, covering a wide momentum range. The main PID detector is the TPC, where particles are identified by their energy loss due to ionization (and atomic excitation) of the TPC gas. The TPC measures the energy loss, charge, and momentum of particles traversing the detector volume. For a given gas the energy loss $\frac{\mathrm{d}E}{\mathrm{d}x}$ depends only on

$$\beta\gamma = \frac{p}{mc}, \tag{4.1}$$

where β is the particle velocity, γ is the Lorentz factor, and p and m are the particle momenta and mass, respectively. Thus particles can be identified based on a deviation from theoretical parametrizations of the Bethe Bloch energy loss given as [56]:

$$f\left(\beta\gamma\right) = \frac{P_1}{\beta^{P_4}}\left(P_2 - \beta^{P_4} - \ln\left(p_3 + \frac{1}{\left(\beta\gamma\right)^{P_5}}\right)\right), \tag{4.2}$$

where P_{1-5} are fit parameters tuned to the data.

The PID resolution depends on the charged particle density, being 5.5% for pp and 6.5% for Pb–Pb [1]. For particles with a low momentum ($p \leq 1$ GeV/c), PID can be done on a track-by-track basis, while at higher momentum particles are separated on a statistical basis. At high momentum, the Bethe Bloch lines approach each other, and distinguishing particles is no longer possible.

For this analysis, the TPC is used for identifying electrons. Other methods for PID such as the measured energy loss in the ITS and electron identification using the TRD are not used. Combining PID information from these subdetectors with the TPC information would make a somewhat cleaner electron sample, but with the cost of a huge loss in statistics. For cross section measurements, achieving high statistics is important while the purity of the selected electron sample has a lower priority. Therefore, the PID is performed using only TPC information.

Figure 4.3, taken from [59], visualizes the idea of the electron selection performed in this analysis. Here, the energy loss of different particles is displayed in grayscale, where the black lines are the expected Bethe Bloch curves. The highlighted area is the selected $n\sigma_{\mathrm{e}}$, i.e. deviation from the electron curve according to equation 5.7.

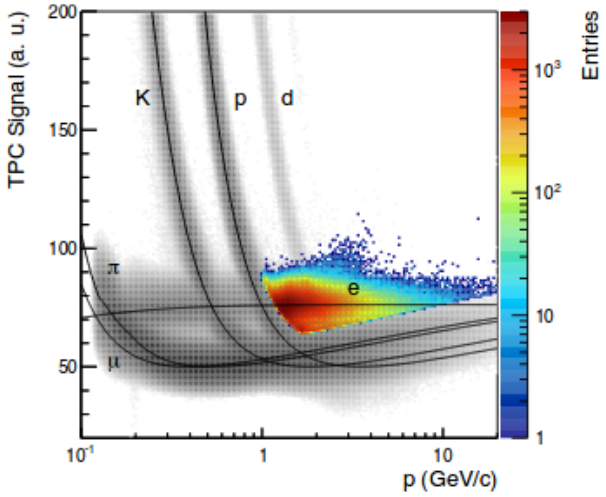

FIGURE 4.3: A visualization of electron track selection, showing the TPC signal in arbitrary units vs the momentum as reconstructed by the TPC where the grayscale shows all tracks passing lose cuts, and the colored area are tracks passing the electron cuts. The black lines are the expected Bethe Bloch energy loss curves. The figure is taken from [59] and is used only as a representation of the performed PID selection.

Chapter 5

J/ψ analysis

This chapter presents the measurement of the inclusive J/ψ cross section in pp collisions at $\sqrt{s}$ = 13 TeV, as a function of p_{T}. The data set and Monte Carlo simulations are described, as well as the different event and track selections. Further, the signal extraction, acceptance and efficiency corrections are introduced and finally the cross section is presented.

5.1 ALICE analysis framework

This analysis is performed using the ALICE analysis framework, namely the packages AliRoot [60] and AliPhysics [61]. Both packages are based on ROOT [62], an object-oriented programming framework, using the C++ language. The AliRoot package is used for processing raw data and handles Monte Carlo (MC) based event simulation through event generators like PYTHIA [63], and particle transportation through the detector using detector simulations like GEANT [64]. The generated events deposit energy in the detector, which is transformed into real detector response, including any possible electronic signal manipulation, such as digitalization [65]. The reconstruction procedure, as described in section 4.3, is the same for both raw data and MC generated events. The output form of the reconstructed event is the Event Summary Data (ESD) file, which for MC also includes the full information about the generated particles, namely the particle species and momentum. The AliPhysics package includes software tools used for the analysis of real and simulated data. To access ALICE specific simulation or analysis data, event handlers are used for ESD and MC files [66]. Specific analysis tasks are performed on the ESDs through the train framework on the ALICE computing Grid [67], creating files containing only necessary event and track information using a smaller data storage space. These files can be used for local analysis.

5.2 Data samples and Monte Carlo simulations

In this thesis, data from proton-proton collisions at the LHC at $\sqrt{s} = 13$ TeV taken during the period from 2016 to 2017 is analyzed together with MC simulations anchored to the same data runs. The following section describes the analyzed data and MC productions.

5.2.1 Data samples

The analyzed events are minimum bias (MB) events, based on the coincidence between V0A and V0C signals. This trigger configuration is referred to interchangeably as V0AND and INT7. The MB trigger is used to trigger on hadronic events, while simultaneously rejecting beam-gas events via offline timing cuts. The analyzed pp events are divided into periods named LHC16a-p and LHC17c-r corresponding to the 2016 and 2017 data sets, respectively. The periods contain different runs, where a run is a continuous time of data taking, i.e all data taking conditions were consistent. The list of runs used are good runs for the central barrel tracking, according to the ALICE Data Preparation Group (DPG)[1]. The run lists provided by the DPG can be found in [68].

$\mathrm{TPC}_{\mathrm{acceptance}}$		N_{runs}	$N^{\mathrm{sel}}_{\mathrm{V0AND}}$	$N^{\mathrm{corr}}_{\mathrm{V0AND}}$		$N_{\mathrm{runs,\ MC}}$	$N_{\mathrm{evts.,\ MC}}$
	MB triggered data				*MC anchored to data, J/ψ injected*		
Complete	LHC16[d-p]	510	4.88×10^8		LHC17h2[a-k]	510	1.73×10^7
Incomplete		55	7.73×10^7			55	2.37×10^6
Total		565	5.65×10^8	5.51×10^8		565	1.97×10^7
Complete	LHC17[c-r]	757	8.14×10^8		LHC18b1a[c-r]	757	7.54×10^7
Incomplete		39	1.73×10^7			39	1.63×10^6
Total		796	8.31×10^8	8.10×10^8		796	7.70×10^7
Complete	TOTAL	1267	1.30×10^9		TOTAL MC	1267	9.27×10^7
Incomplete		94	9.45×10^7			94	3.99×10^6
Total		1361	1.40×10^9	1.36×10^9		1361	9.67×10^7

TABLE 5.1: Number of runs and selected events for the selection of good runs with complete, reduced, and including reduced TPC acceptance for data and MC periods used in this analysis. The number of events after correction, due to a cut on the z vertex, is also shown.

The requirement for good runs in the central barrel is full SSD, SPD, SDD, and V0 information. In addition, the TPC acceptance must be good, but as this analysis is statistically hungry, runs with incomplete TPC acceptance are also included. The MC simulations of these incomplete TPC runs are found to describe the data well, thus the runs are included as they are found not to pose any bias to the analysis. Table 5.1 shows the total number of runs as well as physics and trigger selected events $N^{\mathrm{sel}}_{\mathrm{V0AND}}$ that are used in the analysis for each year of data taking. This number is furthermore corrected for a cut applied on the vertex position along the beamline,

[1]The DPG is a working group within ALICE responsible for steering and coordinating data reconstruction and MC simulation, as well as organizing the quality assurance of aforementioned data and MC reconstruction. Further information can be found on http://alice-offline.web.cern.ch/Activities/alice-data-preparation-group.

which is explained in greater detail in section 5.3. In total, about 1.4 billion events are analyzed, corresponding to 1361 runs. The period-wise summaries can be found in appendix A.

5.2.2 Monte Carlo productions

In addition to the analyzed data sample, a PYTHIA generated event simulation is used. Hereby, all data taking conditions are reproduced, e.g. the reproduction of incomplete TPC sectors. This MC sample is used to obtain the corrections for detector acceptance and efficiency, which will be described in section 5.6. Further, the MC signal shape of the J/ψ is used in the signal extraction method discussed in section 5.5. The MC sample consists of minimum bias events, but with additional J/ψ mesons added on top of the pp collision. This is due to the fact that the J/ψ is a rare signature, and to improve statistics every simulated event is enhanced with a J/ψ meson. The used MC sample consists of 95 million events from 1361 runs. The total event statistics is shown in table 5.1, while statistics for each period can be found in appendix A. The injected J/ψ are added as 70% and 30% being prompt and non-prompt, respectively. The prompt J/ψ mesons are produced following a "natural" p_{T} spectrum for $p_{\mathrm{T}} > 0$ GeV/c and in addition following a flat spectrum for $p_{\mathrm{T}} > 6$ GeV/c. Non-prompt J/ψ mesons come from the decay of B-hadrons, and this is incorporated in PYTHIA. The decay of the J/ψ mesons is handled using PHOTOS [69], an algorithm for QED simulations in MC. More information on the MC setup can be found here [70].

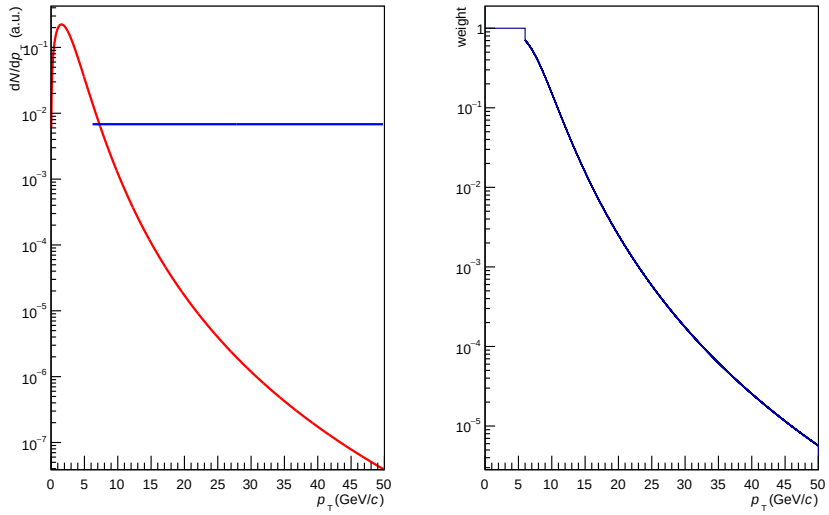

FIGURE 5.1: *Left:* The J/ψ injected p_{T} spectra in the MC sample. *Right:* The weighted p_{T} spectra.

The left panel of figure 5.1 shows the J/ψ injected p_{T} spectra in the MC sample. A correction of the p_{T} spectra must be applied, due to the injected J/ψ following a flat p_{T} distribution at higher

p_{T}. This is taken into account by giving each MC-truth J/ψ candidate a weight, and randomly rejecting candidates with a weight less than 1. For candidates with $p_{\mathrm{T}} > 6$ GeV/c the assigned weight is the fraction of the flat p_{T} spectrum to the total p_{T} spectrum. The J/ψ candidates following a natural p_{T} spectrum are assigned the weight 1 and are not rejected. The right panel of figure 5.1 shows the weighted p_{T} spectra.

5.2.3 Data quality assurance

To ensure a good quality of the data, the consistency between data and MC is investigated, as well as the data quality itself. Different quantities used in the selection of events (described in section 5.3), such as the number of SPD tracklets, i.e. line segments built using clusters in the two layers of the SPD, and vertex contributors, are compared. The runwise comparison of average event selection quantities between data and MC can be found in appendix B.1 to B.5. A good agreement between selected data and MC events is observed.

Further, the agreement between data and MC for quantities used in the selection of tracks (described in section 5.4.2) are investigated. Due to the J/ψ enhanced MC production, primary electrons from J/ψ decays are dominant in the MC sample. This is not the case for the data, where the electron sample is a mixture of primary electrons from multiple sources, secondary electrons from photon conversions, and misidentified hadrons. Thus, some track selection quantities show a larger discrepancy between data and MC. The runwise quantities can be found in appendix B.7 to B.13 where the most notable discrepancies between data and MC are the number of ITS and TPC clusters and the ITS and TPC χ^2 values, as can be seen in figures B.10 to B.13. Hard primary electrons usually have more ITS clusters per track, thus the average number of ITS clusters is higher in the MC sample than for the data sample. The observed discrepancy in the average number of TPC clusters is due to the fact that pileup tracks (described in section 5.3.1) present in the TPC slightly decreases the charge of a given cluster, modifying the energy loss such that some clusters might not be found. This leads to a slightly lower number of TPC clusters than observed for the MC sample, where there is no pileup. Due to the observed discrepancies, cuts are kept as open as possible in order to minimize the systematic uncertainties.

Figure B.6 shows the mean η distribution fluctuating around 0 for both data and MC. In figure B.7 the average φ distribution can be seen situated roughly at π in both data and MC. For period LHC17o there is a jump in the φ distribution for some runs. The runs showing an offset are runs with incomplete TPC acceptance. This is better displayed in figure 5.2, where the left panel shows the run selection including runs with incomplete TPC acceptance, and the right panel shows only runs with complete TPC acceptance. For the runs showing an offset, the MC is in good agreement with the data, and it is therefore determined that these runs need not be removed from the data sample.

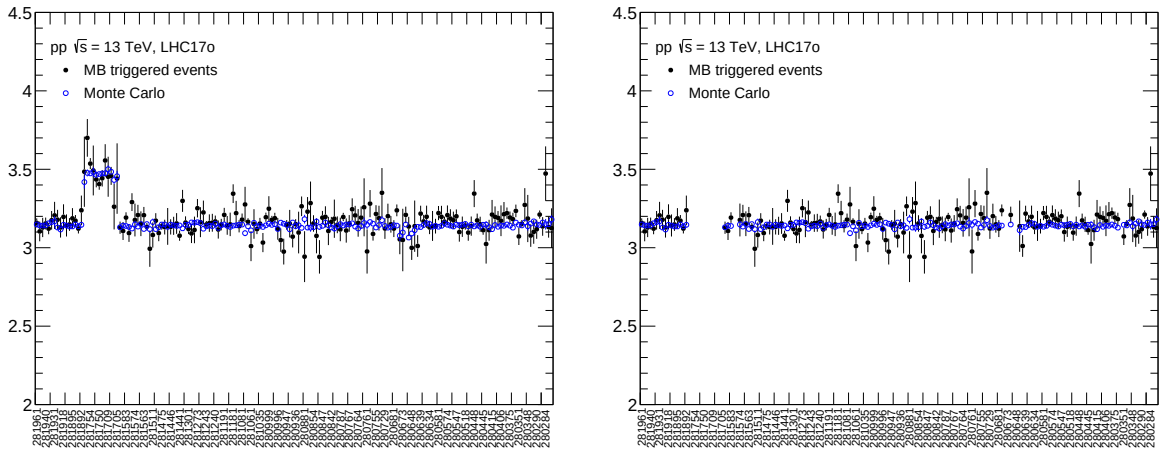

FIGURE 5.2: Runwise average φ for selected electron tracks in period LHC17o, for the total run selection including runs with incomplete TPC acceptance on the left and for runs with complete TPC acceptance on the right. The labels along the x axis show the run number of every third run.

Four of the produced periods do not have dedicated TPC splines, i.e. Bethe-Bloch parametrizations tuned to the specific data period. The PID selection (described in section 5.4.3) for these periods show a greater discrepancy between data and MC than the remaining periods. The discrepancy can be seen in figure 5.3, showing the average TPC $n\sigma_e$ for each run, i.e. the deviation of the measured energy loss to the expected energy loss in terms of the resolution of the energy loss measurement according to equation 5.7. The periods missing dedicated TPC splines are LHC16k (turquoise), LHC16l (yellow), LHC17e (blue) and LHC17k (red). For these periods, a post calibration, further described in section 5.4.4, is performed. Figure 5.4 shows the runwise TPC $n\sigma_e$ after the calibration, where the agreement between MC and data is good. A pure electron sample would have a TPC $n\sigma_e$ value centered around 0, but due to the pion rejection cut (5.4.3), the MC average is shifted upwards. This can be seen from figure 4.3 where the pion rejection closes in on the electron band at high p_{T}, thus shifing the average of the distribution. For the data, there is some contamination from the pion band in addition to the pion cut, and the average value gets a slightly negative shift.

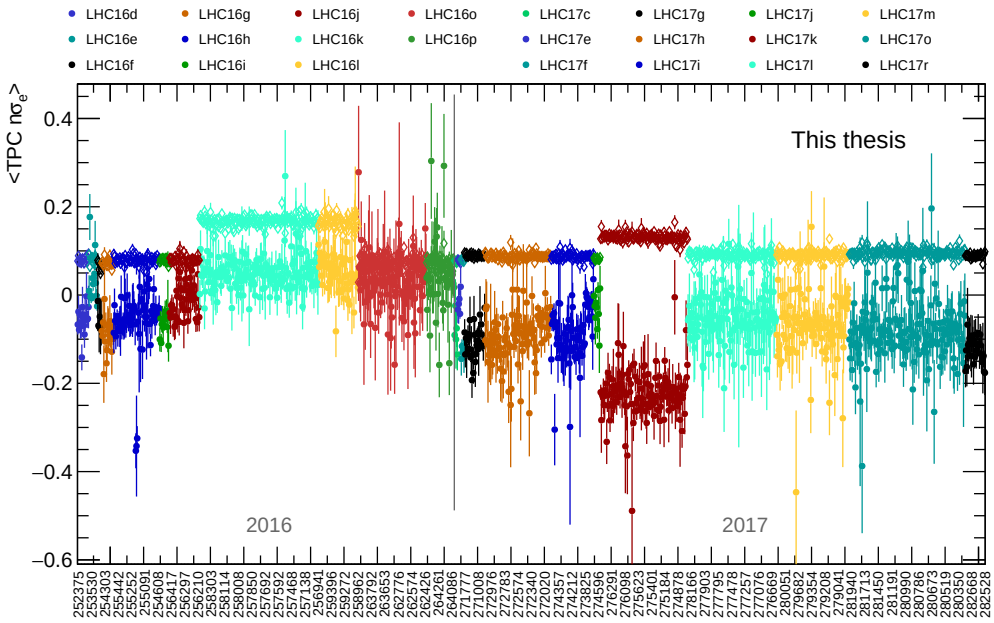

FIGURE 5.3: Average TPC $n\sigma_e$ for selected electron tracks per run for MB events and corresponding MC events in open and closed points, respectively. The labels along the x-axis show the run number of every 20th run.

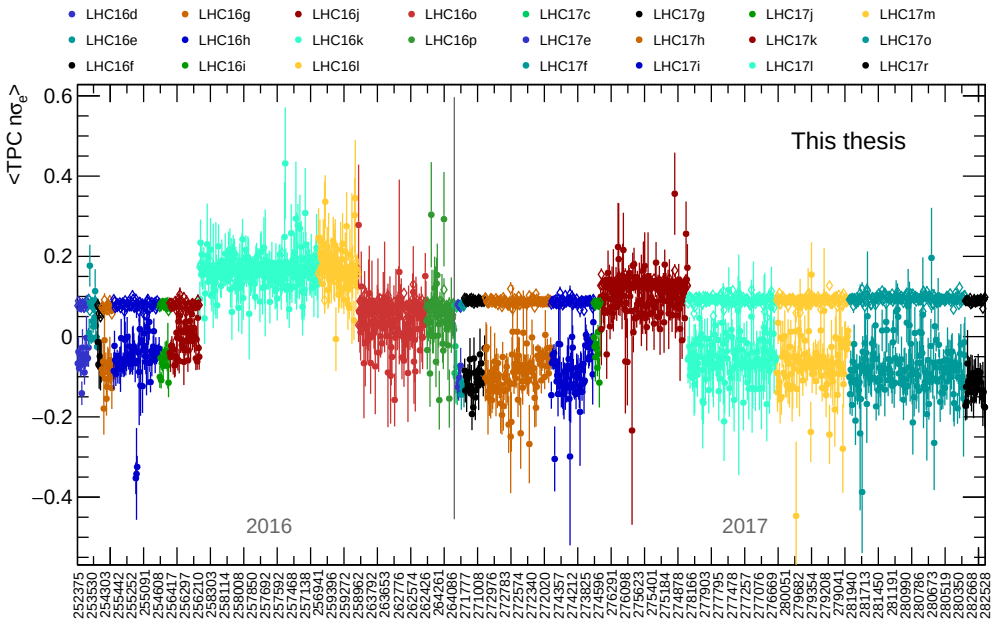

FIGURE 5.4: Average TPC $n\sigma_e$ for selected electron tracks per run for MB events and corresponding MC events after performing a TPC calibration in open and closed points, respectively. The labels along the x-axis show the run number of every 20th run.

5.3 Event selection

Only events with good collision candidates, i.e events where a beam crossing actually took place, are included in this analysis. The beam crossing happens at a small angle, causing a small spread of the primary vertex position. While the spread in the transverse plane is negligible, the spread along the beam direction is of the order of a few cm. To ensure that selected events are well within the geometrical acceptance of the central barrel detector, a cut on the vertex position along the beam axis (z) is performed. Events must have a collision vertex position of $|z| < 10$ cm. In addition, events are required to have a vertex with at least one vertex contributor, i.e. associated tracklet.

5.3.1 Pileup rejection

The selected events can be contaminated by so-called pileup. Pileup due to the overlap of several events from the same bunch crossing is referred to as in-bunch pileup, while out-of-bunch pileup denotes signals from earlier bunch crossings overlapping the current event. Out-of-bunch pileup is due to the slow readout time of certain detectors, e.g. the TPC has a readout of around 100 μs which is several times larger than the bunch spacing of 25 ns.

In-bunch pileup contribution is minimized by applying a default pileup rejection procedure available in the event analysis, where all events having an additional vertex with at least 3 contributors and a minimal distance of 0.8 cm to the primary vertex in the z-direction found using SPD information are rejected. For a pileup event, a certain number of clusters will have less associated tracklets than a good event with the same amount of clusters. Thus, the correlation between the number of SPD clusters and the number of SPD tracklets can be used to further reject pileup events. In addition, a multi-vertexer cut is applied, rejecting events with several vertices. This cut is similar to the SPD based pileup event rejection but is not limited to only SPD information. The rejection rejects events with a minimum of 5 vertices and a maximum χ^2 of the contributors of 5.

The number of events N per bunch crossing follows a Poisson distribution,

$$P(\mu, N) = \frac{\mu^N}{N!} e^{-\mu}, \tag{5.1}$$

where μ is the average number of inelastic collisions per bunch crossing. Thus, the relative contamination from in-bunch pileup to a good event can be expressed as:

$$
\begin{aligned}
f_{\text{pileup}}(\mu) &= \frac{P(\mu, N>1)}{P(\mu,1)} \\
&= \frac{1 - P(\mu,1) - P(\mu,0)}{P(\mu,1)} \\
&= \frac{1 - \mu\,\exp(-\mu) - \exp(-\mu)}{\mu\exp(-\mu)}\,,
\end{aligned} \tag{5.2}
$$

where $P(\mu, N > 1)$ is the probability according to equation (5.1) to observe more than one event per bunch crossing, and $P(\mu, 1)$ and $P(\mu, 0)$ are the probabilities of detecting one or no event during a bunch crossing. Table 5.2 shows the maximum μ values for the corresponding periods together with the in-bunch pileup rate f_{pileup}. The contamination from in-bunch pileup is less than 1% for most periods and less than 3.5% for all periods. Most of these undetected in-bunch pileup events have less than 3 associated tracklets (due to the SPD cut), i.e. a low multiplicity, thus the probability of the event containing a J/ψ is small. Hence, no bias is introduced to the measurement from in-bunch pileup.

Period	max. μ	$P(N=0)$	$P(N=1)$	f_{pileup}
LHC16d	0.0659	0.9362	0.06170	0.034
LHC16e	0.0663	0.9359	0.06205	0.034
LHC16f	0.0122	0.9879	0.01205	0.006
LHC16g	0.0122	0.9879	0.01205	0.006
LHC16h	0.0127	0.9874	0.01254	0.006
LHC16i	0.0122	0.9879	0.01205	0.006
LHC16j	0.0127	0.9874	0.01254	0.006
LHC16k	0.0070	0.9930	0.00695	0.004
LHC16l	0.0210	0.9792	0.02056	0.011
LHC16o	0.0231	0.9772	0.02257	0.012
LHC16p	0.0060	0.9940	0.00596	0.003
LHC17c	0.0636	0.9384	0.05968	0.032
LHC17e	0.0627	0.9392	0.05889	0.032
LHC17f	0.0676	0.9346	0.06318	0.035
LHC17g	0.0132	0.9869	0.01303	0.007
LHC17h	0.0163	0.9838	0.01604	0.008
LHC17i	0.0128	0.9873	0.01264	0.006
LHC17j	0.0636	0.9384	0.05968	0.032
LHC17k	0.0130	0.9871	0.01283	0.007
LHC17l	0.0167	0.9834	0.01642	0.008
LHC17m	0.0166	0.9835	0.01633	0.008
LHC17o	0.0250	0.9753	0.02438	0.013
LHC17r	0.0163	0.9838	0.01604	0.008

TABLE 5.2: Average number of inelastic collisions per bunch crossing (μ) and corresponding pileup rate per period for 2016-2017 data.

Some events containing out-of-bunch pileup tracks may also be rejected by these event cuts, but due to the readout time of the detectors, pileup from different bunches can show up on track level. Thus, further tracking cuts must be applied to remove out-of-bunch pileup, as is described in section 5.4.2.

5.3.2 Luminosity

The determination of the integrated luminosity is based on the measurement of a reference cross section, obtained from a Van der Meer (vdM) scan [71]. The vdM scan is performed by moving the two particle beams across each other in the transverse direction. The head-on luminosity for a pair of colliding bunches with particle intensities N_1 and N_2 is determined from measurements of a given process rate R as a function of the beam separation Δx and Δy [56]. The luminosity is determined as

$$\mathscr{L} = \frac{N_1 N_2 f_{\text{rev}}}{h_x h_y}\,, \tag{5.3}$$

where h_x and h_y are the effective beam widths in x and y-direction, and f_{rev} is the LHC revolution frequency. The reference cross section σ_R is given by:

$$\sigma_R = \frac{R(0,0)}{\mathscr{L}}\,, \tag{5.4}$$

where $R(0,0)$ is the head-on rate.

For this analysis, the trigger cross section σ_{V0AND} is used as the reference cross section. The $\sqrt{s} = 13$ TeV reference cross section for pp collisions is [72]:

$$\sigma_{\text{V0AND}} = 57.8 \text{ mb} \pm 5\%(\text{syst.})\,.$$

The integrated luminosity is determined from the number of minimum biased (V0AND) triggered events, divided by the trigger cross section,

$$\mathscr{L} = \frac{N^{\text{corr.}}_{\text{V0AND}}}{\sigma_{\text{V0AND}}}\,. \tag{5.5}$$

The number of events $N^{\text{corr.}}_{\text{V0AND}}$ includes events with and without a reconstructed vertex within the vertex requirement $|z| < 10$ cm. A reconstructed vertex requires at least one track in the central barrel acceptance and not all MB events have a reconstructed vertex. Thus, the number of events with a reconstructed vertex within the vertex requirement can be determined directly, while the number of events without a reconstructed vertex can only be estimated. This is illustrated in figure 5.5, where the black circle represents the physics and trigger selected events, the blue circle represents events with a vertex position within $|z| < 10$ cm, and the red circle represents events with a reconstructed vertex. The event numbers represented by the black and red circle are

available in the analysis data, while the correct event number, represented by the blue circle can only be estimated.

By assuming that events without a reconstructed vertex follow the same vertex distribution as reconstructed events, the number of events, including events without a reconstructed vertex, is estimated from the fraction f_z. Here, f_z is the fraction of reconstructed events within a z-vertex requirement $|z| < 10$ cm to the number of reconstructed events without a z-vertex requirement, taken from a smaller unbiased sample.

The number of events is estimated by multiplying the number of physics and trigger selected events $N^{\text{sel.}}_{\text{V0AND}}$ with the fraction f_z. Thus, the number of minimum bias events is given by

$$N^{\text{corr.}}_{\text{V0AND}} = f_z \cdot N^{\text{sel.}}_{\text{V0AND}} = \frac{N^{\text{rec.},|z|<10\ \text{cm}}_{\text{V0AND}}}{N^{\text{rec.vtx}}_{\text{V0AND}}} \cdot N^{\text{sel.}}_{\text{V0AND}} \,. \tag{5.6}$$

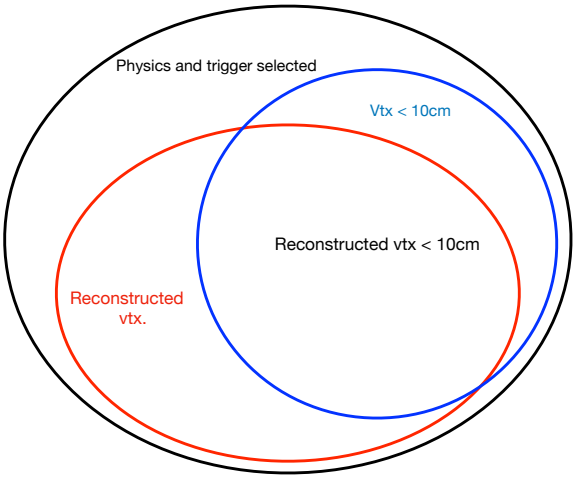

FIGURE 5.5: Representation of event number for physics and trigger selected events in black, events with a reconstructed vertex in red, and events with a z-vertex position less than 10 cm in blue. The blue circle is the number of MB triggered events used for determining the luminosity.

The fraction f_z is determined from a Gaussian fit to the z-vertex distribution. The z-vertex follows a Gaussian distribution for all periods, but the fraction within $|z| < 10$ cm varies. The event correction is therefore applied on a period-by-period basis. For all periods the Gaussian fit agrees well with the shape of the z-vertex distribution and the uncertainty of the fraction was found to be at the sub permille level. The left panel of figure 5.6 shows the z-vertex distribution for period LHC16j with a Gaussian fit describing the distribution well. The distributions for the remaining periods are shown in appendix B.3. The obtained fraction f_z is shown for each period in the right panel of figure 5.6.

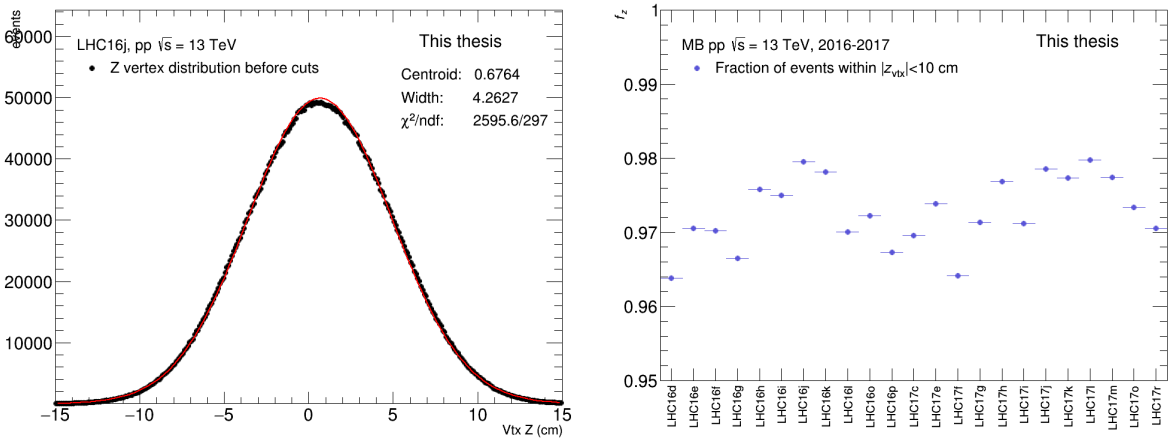

FIGURE 5.6: *Left*: Z-vertex distribtuion of period LHC16j. *Right*: The fraction f_z of events within a vertex cut of $|z| < 10$ cm for each period.

In addition to the assumed vertex distribution, the correction is based on the assumption that all events containing a J/ψ are triggered by the MB trigger, and that all events containing a J/ψ have a vertex with at least one contributing track. Based on these assumptions the number of physics and trigger selected events, represented by the black circle in figure 5.5, include all events containing a J/ψ. The selected and corrected number of events are shown in table 5.1.

The integrated luminosity determined from equation 5.5 amounts to

$$\mathscr{L} = 23.5 \text{ nb}^{-1} \pm 5\%(\text{syst.}) \,,$$

where the statistical error is found to be negligible.

5.4 Track selection

The J/ψ is reconstructed via the di-electron decay mode. Electron and positron tracks are reconstructed in the ITS and TPC in the central barrel. Various selection cuts are applied to select electron candidates and reduce the background. The following section describes the various tracking cuts. A summary of the chosen cut selection is shown in table 5.3.

Variable	cut value
$\lvert\mathrm{DCA}_{xy}\rvert$	< 0.5 cm
$\lvert\mathrm{DCA}_{z}\rvert$	< 2 cm
$\lvert\eta\rvert$	< 0.9
p_{T}	> 1 GeV/c
TPC $n\sigma_e$	$\in [-3.0, 3.0]$
TPC $n\sigma_p$	> 3
TPC $n\sigma_\pi$	> 3
require ITS refit	yes
require TPC refit	yes
reject kinks	yes
require SPD any	yes
TPC $\lvert\chi^2\rvert$	$\in [0.0, 4.0]$
ITS $\lvert\chi^2\rvert$	$\in [0.0, 30.0]$
TPC $N_{\mathrm{cls.}}$	$\in [70, 160]$
TPC N track segments	≥ 6
ITS $N_{\mathrm{cls.}}$ shared	≤ 1

TABLE 5.3: Electron and positron selection cuts. Here DCA_{xy} and DCA_{z} is the distance of closest approach to the primary vertex in the transverse direction and along the beam pipe, respectively. $n\sigma$ is the deviation from the expected energy loss and $N_{\mathrm{cls.}}$ is the number of clusters.

5.4.1 Kinematic cuts

Based on the acceptance of the central barrel, only tracks with a polar angle θ between 45° and 135° are selected. This is equivalent of a pseudorapidity cut $|\eta^{\mathrm{e}^{\pm}}| < 0.9$. In figure 5.7, the η - φ distribution of selected electron and positron tracks is shown for data on the left and MC on the right. The regions with the largest amount of hits, e.g. red regions in MC, are the different TPC segments. At the segment boundaries, the number of hits is reduced. Additionally, regions with incomplete TPC acceptance can be observed. These regions are well represented in the MC as can be seen in figure 5.7 and are therefore not problematic for this analysis. Overall, the distribution shows an even distribution of hits and there is good agreement between data and MC.

To reject background from gamma conversions, π^0 decays, and misidentified hadrons, a lower cut on the transverse momentum of the electron candidates is used. Such a cut is possible due to the fact that a J/ψ decaying into electrons requires a momentum transfer of about 1.5 GeV/c for each electron in the mother rest frame. For this analysis, the lower momentum cut is set to $p_{\mathrm{T}}^{\mathrm{e}^{\pm}} > 1.0$ GeV/c, which does not have a negative impact on the analysis. Figure 5.8 shows the p_{T} distribution of the selected electron tracks. To account for the flat p_{T} spectrum of the injected J/ψ, a re-weighting of the p_{T} distribution in MC as described in section 5.2.2 is applied.

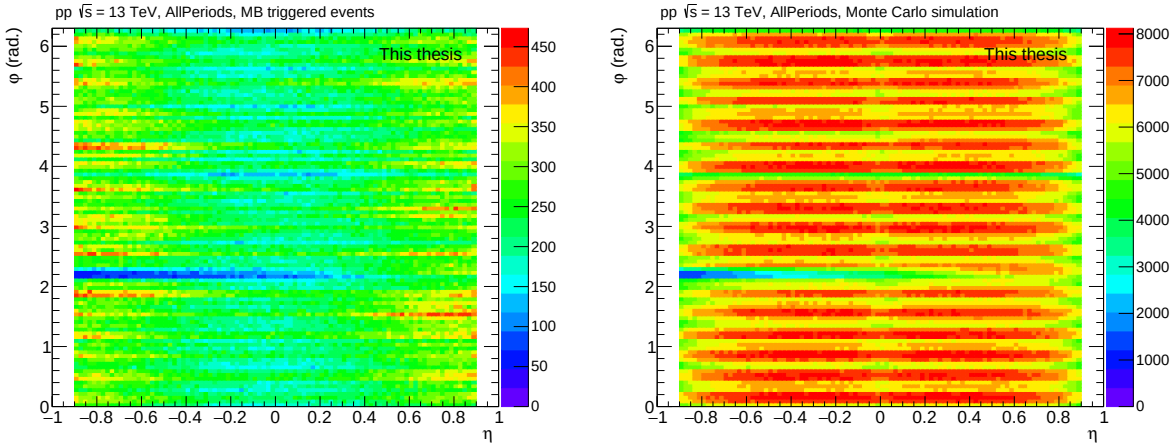

FIGURE 5.7: η vs φ for all MB events on the left and the corresponding MC simulation to the right.

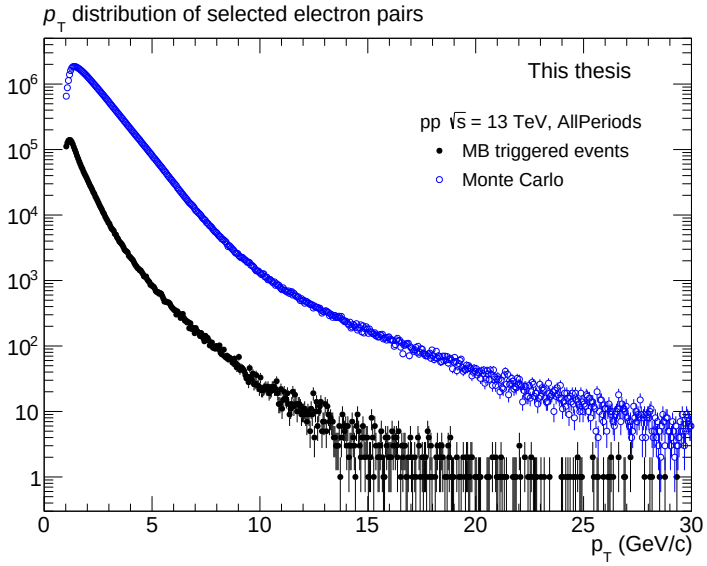

FIGURE 5.8: Transverse momentum distribution for selected electron tracks in MB events (black) and for the corresponding MC simulation (blue).

5.4.2 Tracking cuts

Tracking cuts are applied to ensure that the reconstructed tracks have a good quality and to reject tracks from secondary particles, background sources, and pileup. Primary particles going through the ITS may interact with the detector material creating secondary electrons. In order to minimize this electron contribution, tracks must be associated with a cluster in one of the SPD layers, referred to as SPD any. The track quality is further improved by requiring tracks to not share more than one ITS cluster with any other track. Requirements on the ITS information, such as SPD any and the refit of ITS tracks (section 4.3), are also used to discard most of the (out-of-bunch) pileup contamination, i.e. tracks from drifting charges still present in the TPC after the beam has passed

a full revolution in the LHC. Some (out-of-bunch) pileup might still be present, due to the readout time of the SPD and ITS. Applying a cut on the distance of closest approach (DCA) to the primary vertex helps to remove pileup tracks according to their displacement along the beam-pipe. The electromagnetic J/ψ decay into a di-electron pair is expected to show very little displacement relative to the primary vertex. Cutting on the DCA can remove the tracks from weak particle decays and tracks from material interactions with a larger displacement from the primary vertex. Figure 5.9 shows the DCA distributions for selected tracks in the x-y plane, i.e. transverse to the beam-pipe, on the left and in z, i.e. along the beam-pipe, on the right. The MC distribution is scaled to match the maximum value of the data using a scaling factor of 0.04. Some discrepancy is observed between data and MC, as there are more secondaries present in data than MC. The right panel of figure 5.9 shows a broader DCA distribution along the beam line $|\mathrm{DCA}_z|$ in data than for MC, indicating remaining out-of-bunch pileup tracks in data. The mismatch between track selection requirements on the distance of closest approach in data and MC is considered a possible source of systematic uncertainty, described in chapter 6.

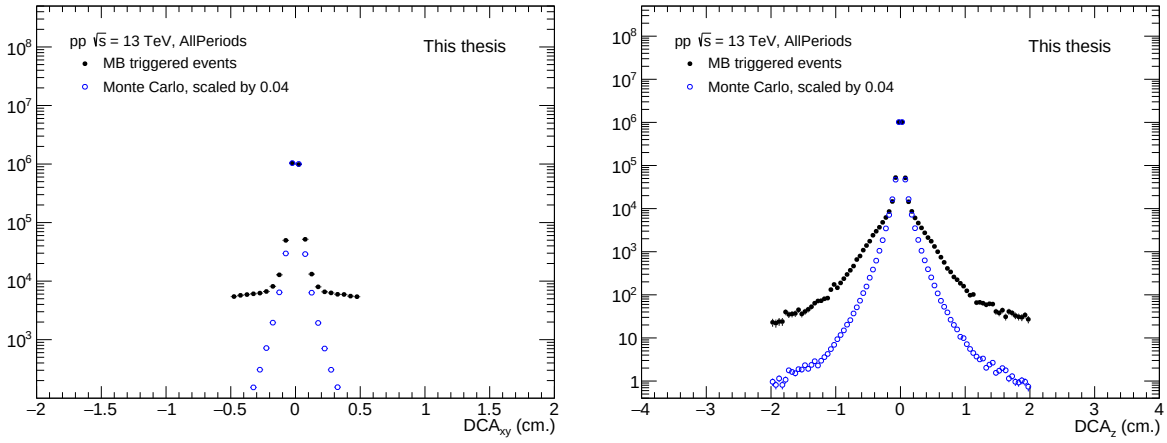

FIGURE 5.9: DCA distribution for selected tracks, to the left in the x-y plane and to the right in the z plane.

The combination of TPC channels used for a given track reconstruction is called clusters. The reconstruction quality is estimated by the number of fired TPC clusters divided by the number of possible TPC clusters. In the rapidity range $|\eta| < 0.9$, the total number of possible TPC clusters is 159, meaning that a minimum of $N_{\mathrm{cls.}} > 70$ assures good track quality. In addition, other TPC cuts, such as limiting the TPC $|\chi^2|$ and requiring a minimum of 6 TPC track segments, are applied to ensure good reconstruction quality. To remove tracks that are associated with particle decays, kinked tracks are rejected.

5.4.3 PID selection

The electron candidate tracks are identified via their specific energy loss in the TPC. Tracks are selected based on a deviation from the expected energy loss determined from a calibrated

parametrization of the Bethe-Bloch energy loss curve. The deviation of the parametrization is expressed in terms of the width of the distribution, according to:

$$n\sigma = \frac{(\mathrm{d}E/\mathrm{d}x)_{\mathrm{meas}} - (\mathrm{d}E/\mathrm{d}x)_{\mathrm{exp.}}}{\sigma_{\mathrm{exp.}}}, \tag{5.7}$$

where $(\mathrm{d}E/\mathrm{d}x)_{\mathrm{meas}}$ is the measured energy loss, $(\mathrm{d}E/\mathrm{d}x)_{\mathrm{exp.}}$ the expected energy loss, i.e. the parametrization, and $\sigma_{\mathrm{exp.}}$ corresponds to the resolution of the energy loss measurement.

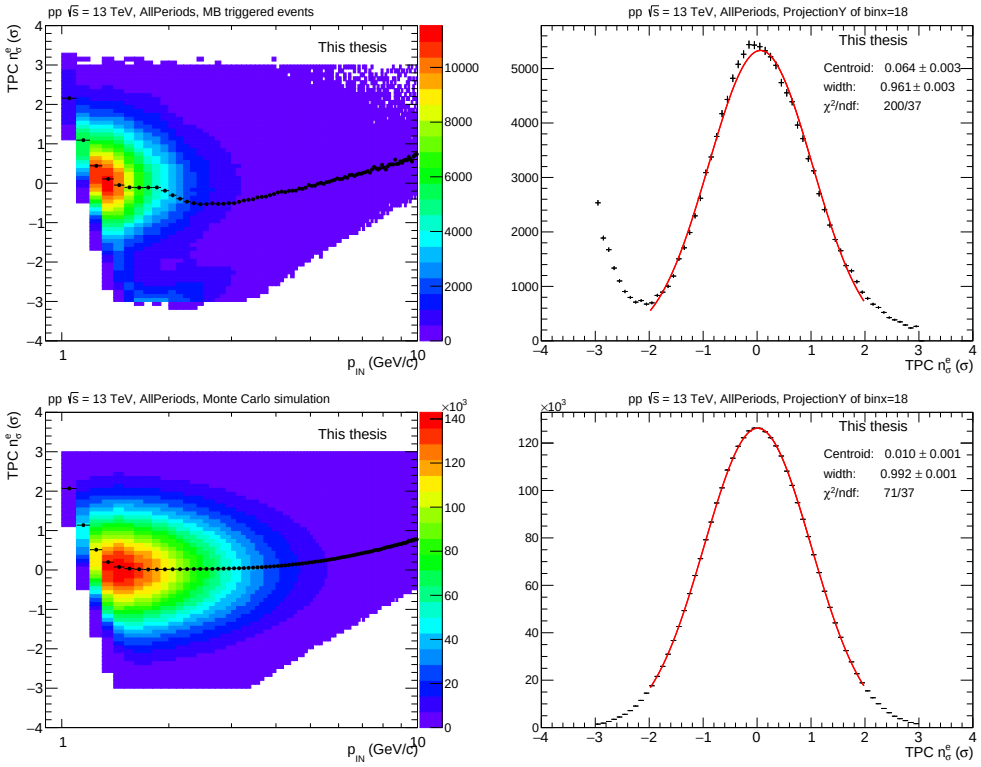

FIGURE 5.10: *Left*: TPC electron $n\sigma_e$ as a function of the momentum as reconstructed by the TPC for selected tracks, for data and MC in the top and bottom panel, respectively. The black points show the profile, i.e. the mean value, of the distributions. *Right*: Distribution of selected electron candidates as a function of $n\sigma_e$ in the momentum interval 1.7 - 1.8 GeV/c fitted with a Gaussian function, for data and MC in the top and bottom panel, respectively.

For this analysis, tracks within a $n\sigma_e \pm 3$ window around the expected electron energy loss line are included. In addition, proton and pion candidates are rejected by requiring $n\sigma_p$ and $n\sigma_\pi > 3$. The left panel of 5.10 shows the TPC $n\sigma_e$ selection versus the momentum as reconstructed by the TPC, for the data and MC, respectively. The black points show the profile, i.e. the mean value, of the distribution. The MC profile shows a smooth distribution, shifted in a slightly positive direction, due to the pion rejection cut. For the data, some pion contamination can be observed, shifting the mean distribution in a negative direction. In the right panel, the distribution of selected electron candidates is shown as a function of $n\sigma_e$ in the momentum interval 1.7 - 1.8 GeV/c fitted with a

Gaussian function. A pure electron distribution should be centered at 0, with a width of 1, which is the case for the MC sample. The data sample has a distribution with a slightly smaller width as there is a small pion contamination in the sample.

Figure 5.11 displays the TPC $n\sigma_e$ as a function of η for data and MC in the left and right panels, respectively. The profile displays a slight dip in the distribution of the data that is not apparent in the MC sample. This dip is clearly present for all the 2017 periods, while the distribution has a flat tendency in the 2016 data, as can be seen in appendix B.4.1.

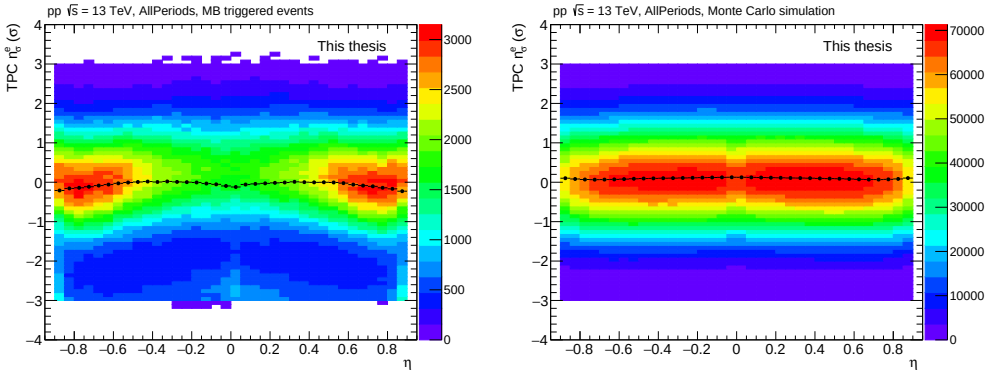

FIGURE 5.11: TPC $n\sigma_e$ as a function of the TPC η for selected tracks in minimum bias events(left) and corresponding MC events (right). The black points show the profile, i.e. the mean value, of the distributions.

5.4.4 Post calibration

As can be seen in figure 5.3, an offset between data and MC is observed in the average $n\sigma_e$ for the periods without dedicated TPC splines. A significant difference is observed in the $n\sigma_e$ distribution as a function of momentum as reconstructed by the TPC and η for period LHC16k, LHC16l, and LHC17k, while LHC17e shows a smaller discrepancy in both cases. This can be seen in the top panels of figure 5.12 showing the TPC electron $n\sigma_e$ ratio between data and MC as a function of η and TPC momenta for period LHC16k on the left and right, respectively. The data/MC ratio for all remaining periods can be found in appendix B.4.2 and B.4.3 for the $n\sigma_e$ distribution vs η and momentum as reconstructed by the TPC, respectively.

The figures in appendix B.4.4 show the TPC $n\sigma_e$ distribution as a function of the momentum as reconstructed by the TPC as well as the distribution of selected electron candidates as a function of $n\sigma_e$ in the momentum interval 1.7-1.8 GeV/c fitted with a Gaussian function for all data periods. The electron band should be centered around 0, with a width of 1. This is not the case for the periods without dedicated TPC splines. LHC16k and LHC16l have a significantly smaller width around 0.7. While LHC17k is shifted towards the left, with a width of about 0.8. LHC17e has a distribution similar to the whole 2017 data set, with only a slightly positive shift and a width of 1. The remaining data periods are nicely situated around 0 with a width of 1.

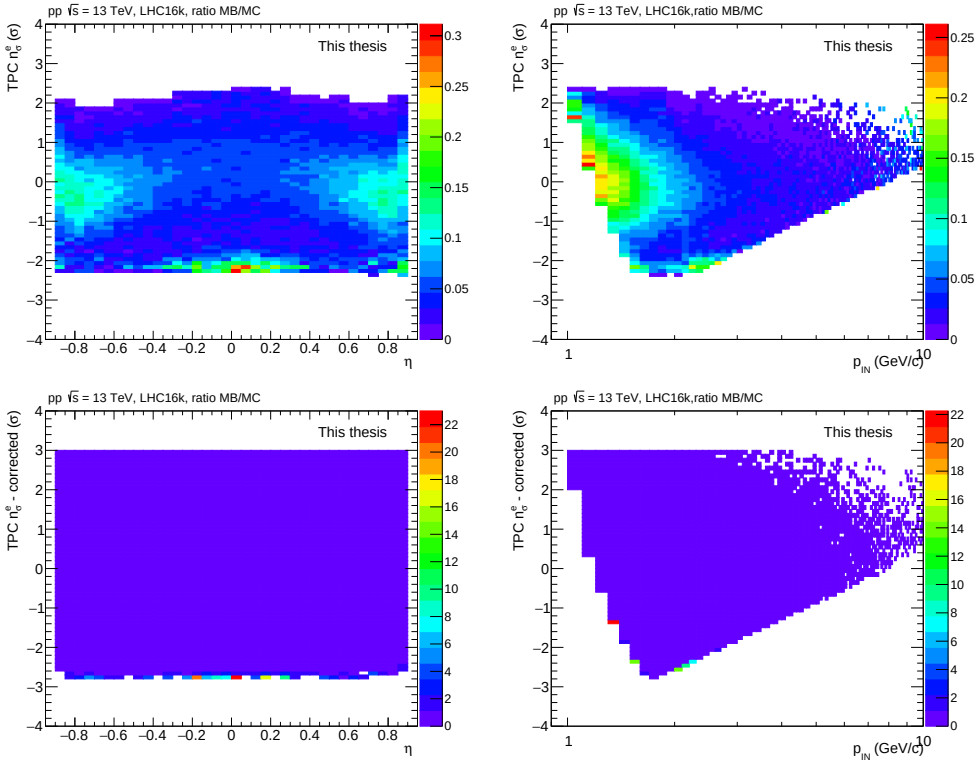

FIGURE 5.12: Ratio between data and MC for period LHC16k before (top) and after (bottom) post-calibration. The left panel shows the ratio of TPC $n\sigma_e$ as a function of η and to the right as a function of the momentum as reconstructed by the TPC.

A post-calibration is performed to improve the data to MC matching. The calibration is done individually for the four periods, LHC16k, LHC16l, LHC17e, and LHC17k. The lower panels of figure 5.12 show the ratio data/MC of the TPC electron $n\sigma_e$ versus η and TPC momenta after the post calibration of period LHC16k, respectively. After the post-calibration, very little discrepancy between data and MC is observed.

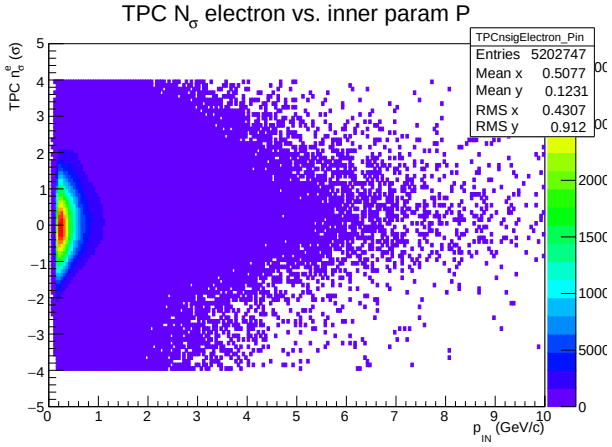

FIGURE 5.13: Tagged conversion electron sample used for TPC post calibration.

The post-calibration exploits a clean electron sample from electrons originating in photon conversions. The tagging is done only with tracking methods, so as not to impose any bias on the PID calibration. Figure 5.13 shows the $n\sigma_e$ distribution of tagged conversion electrons as a function of momentum as reconstructed by the TPC. The distribution shows the sufficiently good electron purity and can be used to extract the mean and widths of the electron band.

The conversion electron selection is made using cuts similar to the cuts used for J/ψ candidates (table 5.3), but as a lot of conversions happen in the ITS material, the requirement for SPD any is removed. The chosen cut values are displayed in table 5.4, where the DCA cut is the distance of closest approach between the electron and positron tracks. The pointing angle θ_{pionting} is the angle between the photon momentum and the vector pointing from the primary vertex to the conversion point. r_{decay} is the position of the conversion point in radial direction and Ψ is the angle between the plane defined by the di-electron pair and the xy-plane.

Variable	cut value
χ^2	< 10
$\cos(\theta_{\text{pointing}})$	$\in [0.0, 0.05]$
DCA	$\in [0.0, 1.0]$ cm
r_{decay}	$\in [3.0, 90.0]$ cm
Ψ	$\in [0.0, 0.2]$
m_{ee}	< 0.1 GeV/c^2
require ITS refit	yes
require SPD any	no

TABLE 5.4: Conversion electron cuts used for post calibration. The cuts are similar to J/ψ cuts, but without any SPD refit requirement.

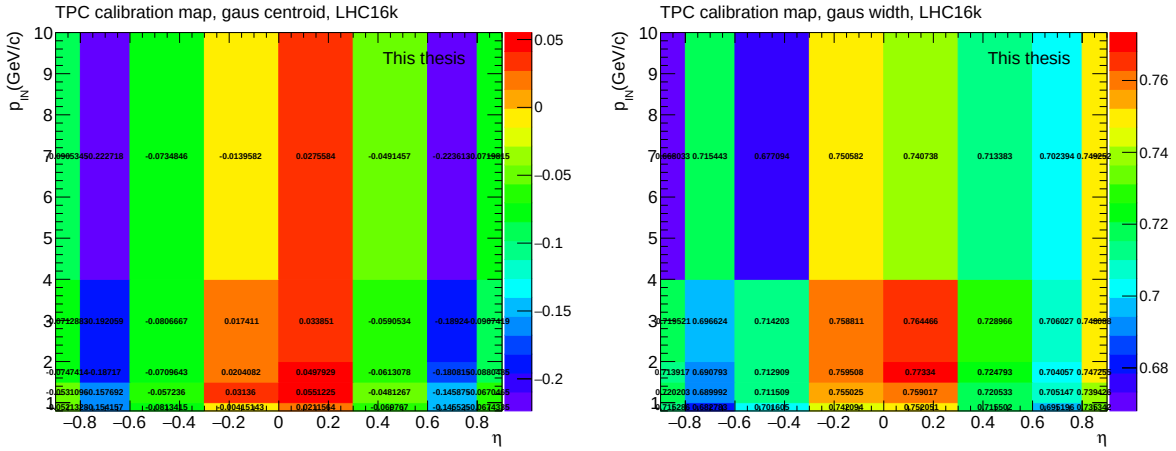

FIGURE 5.14: TPC calibration map obtained for period LHC16k. The left panel shows the mean and the right panel shows the width.

The calibration centers the electron band at 0, with a width of 1, by applying calibration maps. Due to low statistics, calibration maps are obtained only for a few dimensions. For this analysis,

maps are obtained in terms of η and the momentum as reconstructed by the TPC. The calibration maps are used to re-calculate the TPC $n\sigma_e$ value like

$$n\sigma^{\text{calib}}\left(p_{\text{IN}},\eta\right) = \frac{n\sigma\left(p_{\text{IN}},\eta\right) - n_0\left(p_{\text{IN}},\eta\right)}{w\left(p_{\text{IN}},\eta\right)}\,, \tag{5.8}$$

where n_0 is the mean of the uncalibrated electron band and w is the width of the uncalibrated electron band. Figure 5.14 shows the obtained calibration maps for period LHC16k. The remaining calibration maps can be found in appendix B.4.5.

Figure 5.15 shows the TPC $n\sigma_e$ distribution before and after post calibration for period LHC16k, together with a projection in the momentum interval 1.7-1.8 GeV/c, which has been fitted with a Gaussian, in the top and bottom panels, respectively. The distributions for the remaining calibrated periods can be found in appendix B.4.6. The distributions are centered around 0, with a width of 1 for all calibrated periods.

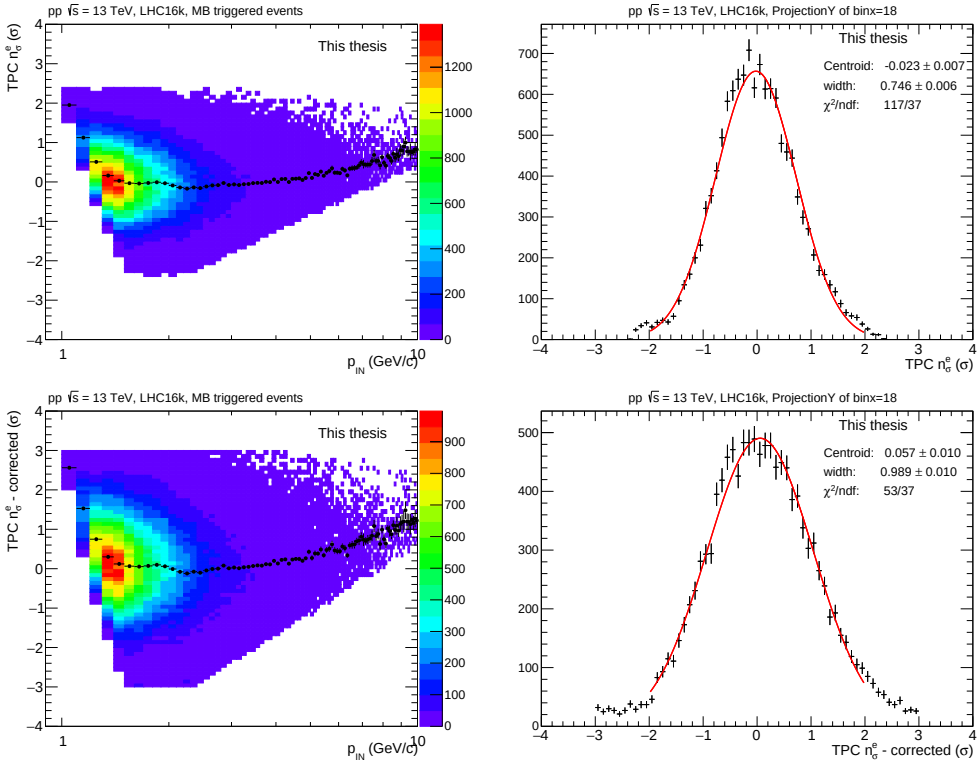

FIGURE 5.15: *Left*: TPC $n\sigma_e$ versus momentum as reconstructed by the TPC before (top) and after (bottom) post calibration for period LHC16k. *Right*: Distribution of selected electron candidates as a function of $n\sigma_e$ in the momentum interval 1.7-1.8 GeV/c fitted with a Gaussian function for the same period before and after post calibration.

5.4.5 Pre-filter selection

The electron candidates selected according to the criteria summarized in table 5.3 also contain electrons originating in photon conversions. A large fraction of these electrons is removed by requiring at least one hit in the SPD layer, as described in section 5.4.2. However, the selection may still include conversion pairs where one leg, i.e. electron candidate, passed the J/ψ candidate cut. A pre-filter selection, i.e. a looser electron cut, is applied to build an additional set of electron candidates. In order to remove conversion pairs, di-electron pairs are built by combining electrons surviving the tight electron cut with electrons surviving the loose selection. If the combined pairs are compatible with the photon conversion criteria, i.e $m_{ee} < 50$ MeV/c^2, the electron candidate passing the J/ψ cut is rejected. Table 5.5 shows the cut values for the pre-filter differing from the standard electron track selection in table 5.3.

Variable	cut value
$\lvert\mathrm{DCA}_{xy}\rvert$	< 3 cm
$\lvert\mathrm{DCA}_{z}\rvert$	< 10 cm
p_{T}	$\in [0.5, 100.0]$ GeV/c
TPC $n\sigma_e$	$\in [-4.0, 4.0]$
TPC $n\sigma_p$	> 2
TPC $n\sigma_\pi$	> 2
TPC $N_{\mathrm{cls.}}$	$\in [50, 160]$

TABLE 5.5: Pre-filter cut selections differing from the standard electron cut selections.

5.5 J/ψ measurement

The J/ψ signal is extracted by bin counting in the signal region of the invariant mass spectrum of the selected electron-positron pairs after a subtraction of the estimated background. The signal extraction is performed for various p_{T} intervals in order to obtain the differential yield. The following section describes the signal extraction procedure in detail. The pair selection, background estimation, and signal extraction will be described, as well as the extracted raw yield. Further corrections to the raw yield are discussed in section 5.6.

5.5.1 Pair selection

After the track and PID selections discussed in section 5.4, the remaining electron-positron candidates are combined into $\mathrm{e}^+\mathrm{e}^-$ pairs to obtain the invariant mass spectrum. These pairs consist of all possible $\mathrm{e}^+\mathrm{e}^-$ combinations in the same event, with an invariant mass above 0.05 GeV/c^2. Figure 5.16 shows the obtained mass invariant spectrum. A clear signal peak around 3 GeV/c^2 indicates the J/ψ resonance, above a background continuum. As most of the di-electron pairs come

from background sources, the signal-to-background ratio is small in the J/ψ signal region. The background consists of a combinatorial background, meaning e^+e^- pairs not having a common physical source and a residual background, i.e. electron pairs originating from a common physical source. The residual background can be decay products from $c\bar{c}$ and $b\bar{b}$ decays or originate from jet fragmentations.

To obtain a clear J/ψ signal, the background must be determined and subtracted from the invariant mass distribution. The background can be estimated through various methods, and in this analysis, a so-called hybrid signal extraction method is used.

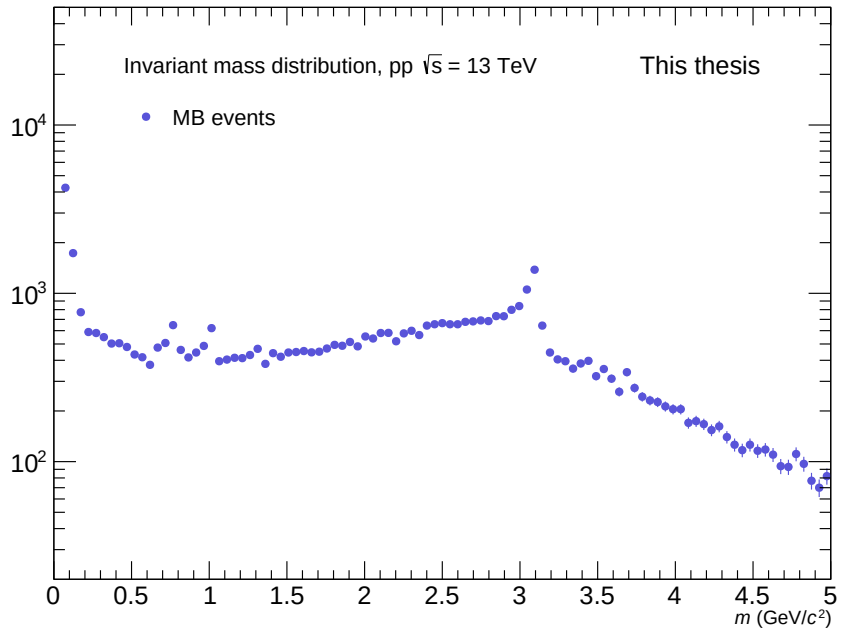

FIGURE 5.16: Invariant mass distribution.

5.5.2 Hybrid background estimation

The hybrid approach for estimating the background determines the combinatorial and residual background separately. The combinatorial background is estimated using pairs with legs from different events in order to remove possible correlations, while the residual background is estimated using a fit.

The combinatorial background is obtained from opposite-sign (OS), i.e. electron-positron, pairs built from mixed events (ME). Events are mixed using a pool depth of 100. To ensure that the mixed events consist of comparable events, events are only mixed within certain event classes, listed in table 5.6. Requiring a similar z-vertex position ensures event mixing with similar geometric acceptance, while the requirement on the number of SPD tracklets provides similar event

multiplicities. Further, the obtained ME-OS distribution is scaled using a so-called R-factor correction. The R-factor is obtained by scaling a like-sign (LS) pair distribution from event mixing to a like-sign distribution from the same event (SE). The LS pair distribution is formed from pairs consisting of e^-e^- and e^+e^+, where an average of the two signs is used. The LS distribution does not have a signal peak within the J/ψ mass window, thus scaling can be applied for the whole invariant mass range.

Variable	N_{bins}	values				
z vertex position	20	$[-10,-9)$ cm	$[-9,-8)$ cm	$[-8,-7)$ cm	$[-7,-6)$ cm	$[-6,-5)$ cm
		$[-5,-4)$ cm	$[-4,-3)$ cm	$[-3,-2)$ cm	$[-2,-1)$ cm	$[-1,0)$ cm
		$[0,1)$ cm	$[1,2)$ cm	$[2,3)$ cm	$[3,4)$ cm	$[4,5)$ cm
		$[5,6)$ cm	$[6,7)$ cm	$[7,8)$ cm	$[8,9)$ cm	$[9,10]$ cm
$N_{\text{SPD tracklets}}$	10	$[1,15)$	$[15,25)$	$[25,35)$	$[35,45)$	$[45,55)$
		$[55,65)$	$[65,80)$	$[80,110)$	$[110,150)$	$[150,200]$

TABLE 5.6: Event categories used in the event mixing approach.

The upper left panel of figure 5.17 shows the invariant mass spectrum in black and the combinatorial background in blue for the p_{T} integrated case. The combinatorial background describes the total background fairly well, but as can be seen in the lower left panel showing the invariant mass distribution after subtracting the combinatorial background, a small residual background contribution remains. The background shape is highly p_{T} dependant, and the combinatorial background is more dominant at lower p_{T}, while higher p_{T} leads to a stronger residual background contribution as can be seen in figure 5.19 and 5.20.

After subtracting the combinatorial background from the invariant mass distribution, the remaining background is estimated by an empirical fit. Due to the energy loss of daughter electrons and positrons, the signal shape shows a strong tail towards lower invariant masses. To allow for a best possible fit, the tail shape is determined from the J/ψ signal shape in MC. The MC signal shape is added to the fitting function to constrain the fit in the region of the low mass tail. As previously mentioned, the combinatorial background is greatly suppressed at higher p_{T}. It was determined that a polynomial fit function would be the best description for $p_{\text{T}} < 2$ GeV/c. At higher p_{T}, the combinatorial background contribution decreases, and an exponential fit function was found to give a better description. The fit functions were chosen based on a good background description, while also allowing for a stable and robust fit. The complete fit function is given as,

$$f_{\text{fit}}\left(m_{\text{inv., e}^+\text{e}^-}\right) = p_0\, S_{\text{MC}}\left(m_{\text{inv., e}^+\text{e}^-}\right) + f_{\text{res. bkg.}}\left(m_{\text{inv., e}^+\text{e}^-}\right) , \tag{5.9}$$

where $S_{\text{MC}}\left(m_{\text{inv., e}^+\text{e}^-}\right)$ is the MC signal count obtained by bin counting of the mass invariant distribution after all cuts are applied. $f_{\text{res. bkg.}}\left(m_{\text{inv., e}^+\text{e}^-}\right)$ is the empirical function describing the (residual) background,

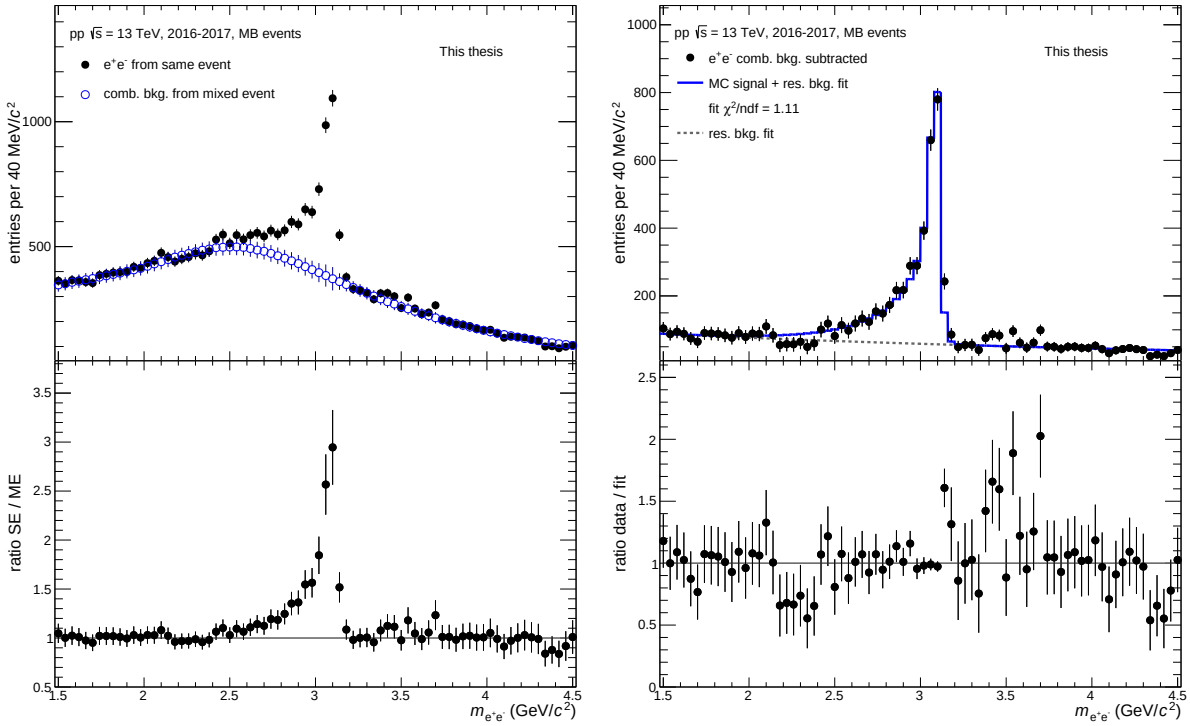

FIGURE 5.17: Invariant mass distribution for p_{T} integrated $\mathrm{e^+e^-}$ pairs from the same event with combinatorial background from mixed events on the left and after combinatorial background subtraction and the corresponding fits on the right.

$$f_{\text{res. bkg.}}\left(m_{\text{inv., e}^+\text{e}^-}\right) = \begin{cases} \left(p_1 + p_2\, m_{\text{inv., e}^+\text{e}^-}\right) & p_{\mathrm{T}} < 2 \text{ GeV}/c \\ \exp\left(p_1 + p_2\, m_{\text{inv., e}^+\text{e}^-}\right) & p_{\mathrm{T}} \geq 2 \text{ GeV}/c \end{cases} . \tag{5.10}$$

The right upper panel of figure 5.17 shows the invariant mass distribution after the combinatorial background subtraction together with the empirical fit. In the lower panel, the ratio between data and fit is displayed. The fit agrees within ±20% and has a reasonable χ^2 of 1.11.

After the combinatorial background subtraction and the fitting of the residual background, the signal count is found by bin counting in the mass signal window $2.92 \leq m_{\text{inv., e}^+\text{e}^-} \leq 3.16$ GeV/c^2. Figure 5.18 shows the invariant mass distribution of the J/ψ signal together with the signal shape obtained from MC. A clear signal peak is observed with a strong tail towards lower invariant mass due to the electron energy loss. The extracted raw yield for the p_{T} integrated case amounts to

$$N_{\text{raw}} = 2304 \pm 69 \,. \tag{5.11}$$

Table 5.7 and 5.8 show the fit parameters and the signal extraction values, respectively.

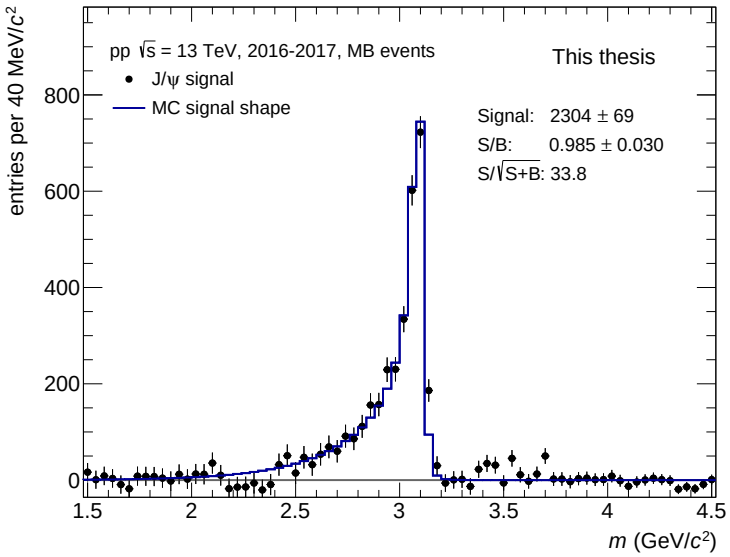

FIGURE 5.18: Signal invariant mass distribution and MC signal shape for p_{T} integrated J/ψ mesons in minimum bias events after combinatorial and residual background subtraction.

5.5.3 Signal extraction in p_{T} intervals

In order to determine the differential yield as a function of p_{T}, the J/ψ signal was extracted in 10 p_{T} intervals in addition to the p_{T} integrated range. Hereby, the signal was extracted using the hybrid method as described in section 5.5.2. Figures 5.19 and 5.20 show the invariant mass distribution for all selected p_{T} intervals in black, and the combinatorial background in red in the respective top panels, while lower panels show the invariant mass spectrum after the background subtraction together with the fit function in magenta. The background shape varies greatly with p_{T}, mostly due to the combinatorial background. As mentioned in section 5.5.2, different fitting functions are used depending on the p_{T} interval. The last panel in figure 5.20 shows only fluctuations for p_{T} > 13 GeV/c and is thus excluded for the yield extraction.

The fit parameters used for fitting each p_{T} bin according to equation (5.10) are listed in table 5.7. For p_{T} bins lower than 2 GeV/c, a polynomial function was used, while the fit to higher p_{T} intervals was done using an exponential function. Apart from the last p_{T} bin containing only fluctuations, the χ^2/ndf is close to 1. p_{T} bin 6 and 7 show a slightly larger offset from 1 then the other bins, due to fluctuations in the lower mass region. The fit parameters for the exponential fits are stable with relatively small uncertainties apart from p_{T} bin 10, while the polynomial fitting parameters have somewhat larger uncertainties. The covariance matrix, i.e. the uncertainty combinations of the fit parameters is incorporated into the statistical uncertainty of the signal count.

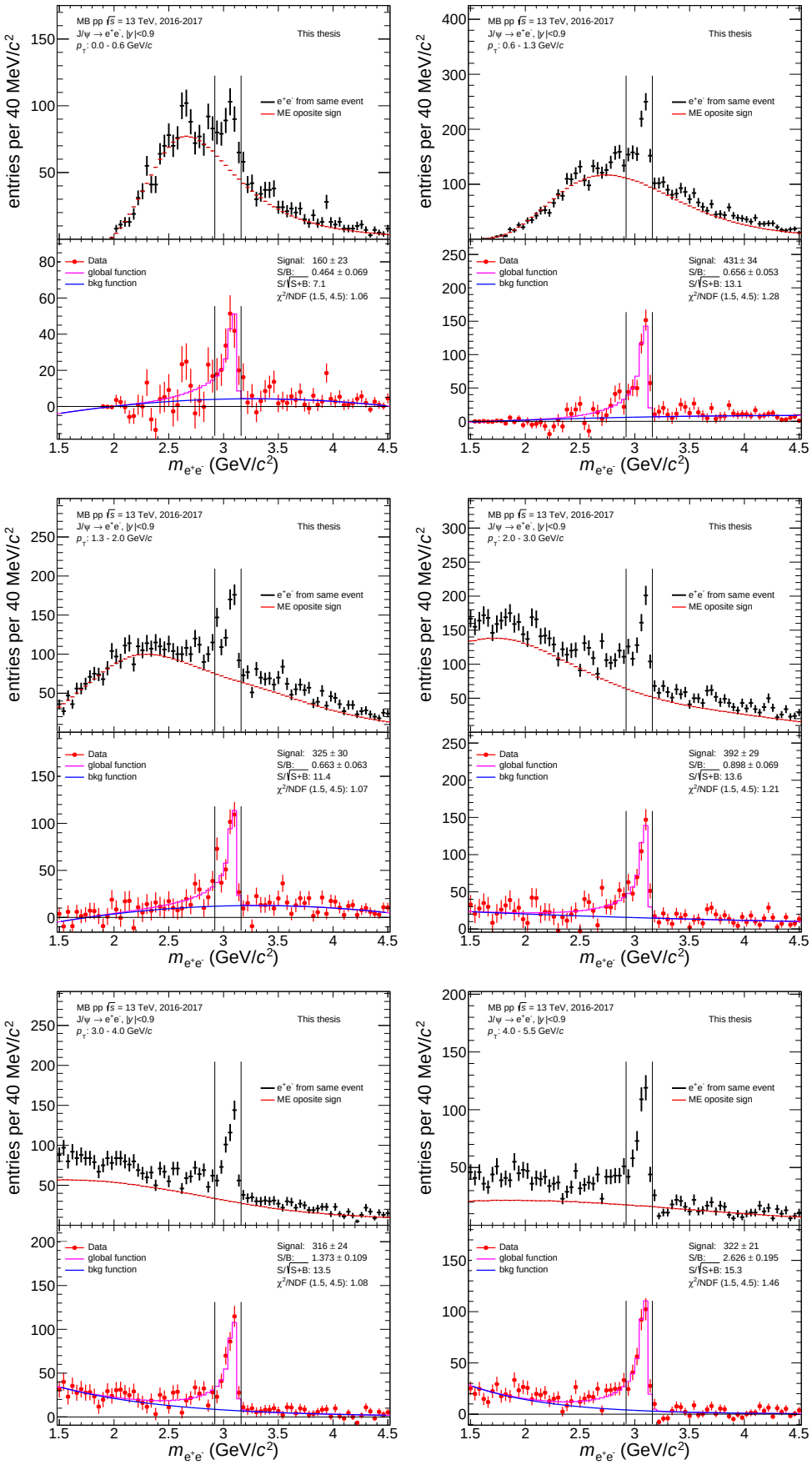

FIGURE 5.19: Signal extraction for p_{T} bins 0.0-0.6 GeV/c (top left), 0.6-1.3 GeV/c (top right), 1.3-2.0 GeV/c (middle left), 2.0-3.0 GeV/c (middle right), 3.0-4.0 GeV/c (bottom left) and 4.0-5.5 GeV/c (bottom right).

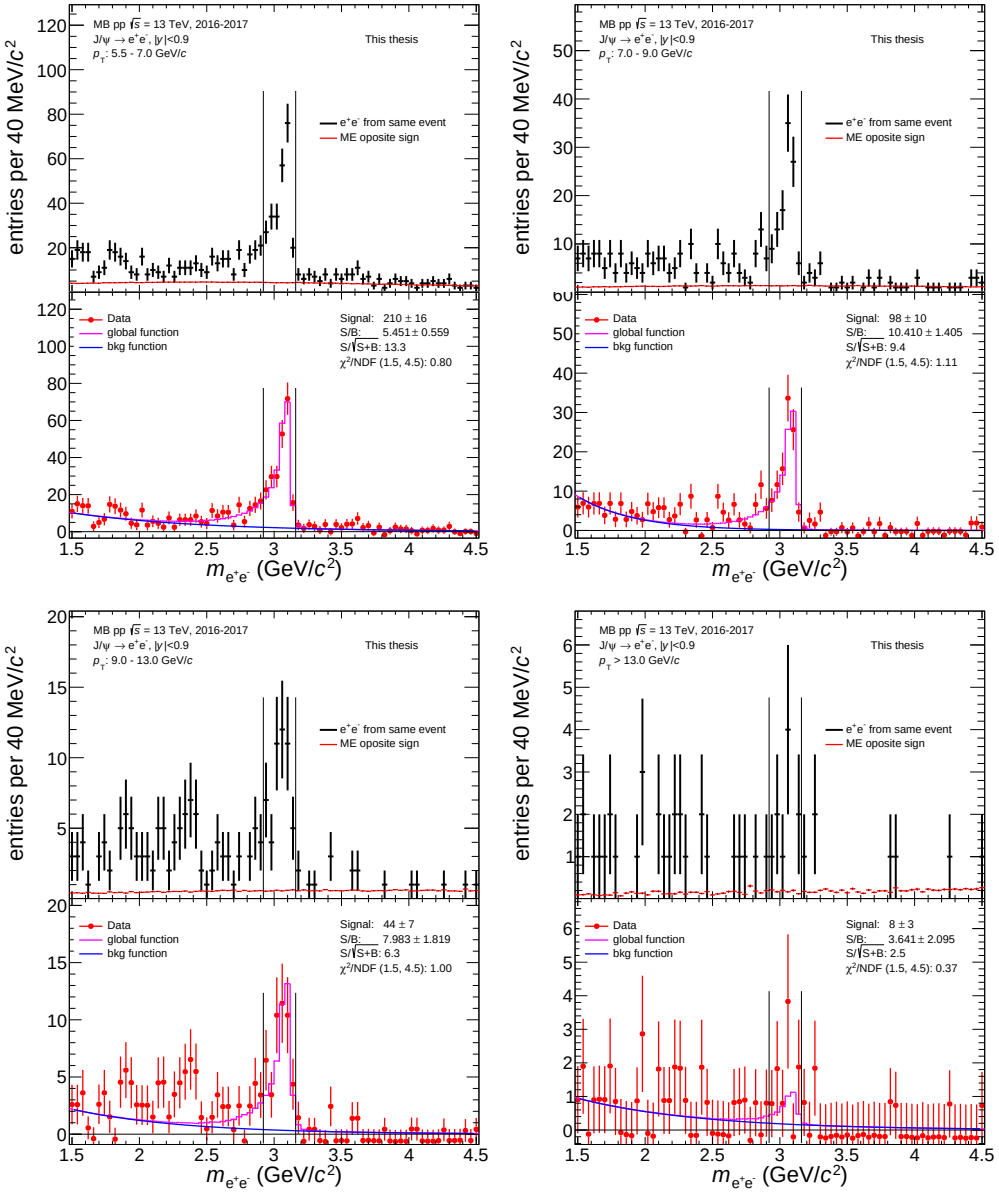

FIGURE 5.20: Signal extraction for p_{T} bins 5.5-7.0 GeV/c (top left), 7.0-9.0 GeV/c (top right), 9.0-13.0 GeV/c (bottom left) and >13.0 GeV/c (bottom right).

p_{T} bin	p_{T}[GeV/c]	χ^2/ndf	$p_0[10^{-4}]$	p_1	p_2	p_3
1	[0.0 , 0.6]	1.06	3.04 ± 0.43	-23.59 ± 7.66	17.05 ± 5.60	-2.61 ± 0.91
2	[0.6 , 1.3]	1.28	3.69 ± 0.28	-13.43 ± 6.67	9.83 ± 5.62	-1.09 ± 0.98
3	[1.3 , 2.0]	1.07	3.01 ± 0.28	-45.45 ± 11.30	35.20 ± 8.13	-5.33 ± 1.33
4	[2.0 , 3.0]	1.21	3.10 ± 0.22	3.56 ± 0.25	-0.28 ± 0.08	
5	[3.0 , 4.0]	1.08	3.30 ± 0.24	4.98 ± 0.24	-0.97 ± 0.11	
6	[4.0 , 5.5]	1.46	3.67 ± 0.23	5.34 ± 0.31	-1.34 ± 0.15	
7	[5.5 , 7.0]	0.80	5.11 ± 0.37	3.85 ± 0.39	-1.03 ± 0.19	
8	[7.0 , 9.0]	1.11	5.62 ± 0.57	5.75 ± 0.82	-2.39 ± 0.46	
9	[9.0, 13.0]	1.00	8.45 ± 1.36	2.56 ± 0.65	-1.19 ± 0.32	
10	[13.0 , 50]	0.37	8.91 ± 7.41	1.57 ± 1.34	-1.09 ± 0.66	
	[0.0 , 50]	1.11	3.61 ± 0.10	4.87 ± 0.11	-0.27 ± 0.03	

TABLE 5.7: Fit parameters from fits of equation (5.10) to corresponding invariant mass distributions (after subtraction of combinatorial background) in minimum bias events.

The lower panels in figures 5.19 and 5.20 also show the signal count, signal to background ratio, and the significance of the signal extraction. These numbers are summarized in table 5.8. Due to rounding for each p_{T} bin, there might be some minor mismatch between the p_{T} integrated counts and the total number of counts in the table. The signal count S refers to the raw J/ψ signal count in the mass window $2.92 \leq m_{\mathrm{inv.,\ e^+e^-}} \leq 3.16$ GeV/c^2. The total background count (combinatorial + residual) B in the same window is also given. S/B denotes the signal to background ratio and $S/\sqrt{S+B}$ is the significance of the signal extraction. The signal to background ratio greatly improves for higher p_{T}, while the significance is above 10 for all but the first and three last p_{T} intervals. When determining the size of the p_{T} intervals, a significance above 6 was preferred. Also, a p_{T} interval with a boundary at 1.3 GeV/c was chosen in order to compare with ongoing measurements of the prompt/non-prompt J/ψ fraction which can not go lower than p_{T} =1.3 GeV/c due to the resolution of the secondary vertex.

p_{T} bin	p_{T}[GeV/c]	S	B	S/B	$S/\sqrt{S+B}$
1	[0.0 , 0.6]	160 ± 23	346 ± 7	0.46 ± 0.07	7.1
2	[0.6 , 1.3]	431 ± 34	657 ± 9	0.66 ± 0.05	13.1
3	[1.3 , 2.0]	325 ± 30	490 ± 10	0.66 ± 0.06	11.4
4	[2.0 , 3.0]	392 ± 29	436 ± 6	0.90 ± 0.07	13.6
5	[3.0 , 4.0]	316 ± 24	230 ± 5	1.37 ± 0.11	13.5
6	[4.0 , 5.5]	322 ± 21	123 ± 4	2.63 ± 0.20	15.3
7	[5.5 , 7.0]	210 ± 16	38 ± 3	5.45 ± 0.56	13.3
8	[7.0 , 9.0]	98 ± 10	9 ± 1	10.41 ± 1.40	9.4
9	[9.0, 13.0]	44 ± 7	6 ± 1	7.98 ± 1.82	6.3
10	[13.0 , 50]	8 ± 3	2 ± 1	3.64 ± 2.09	2.5
	[0.0 , 50]	2304 ± 69	2339 ± 13	0.99 ± 0.03	33.8

TABLE 5.8: Signal extraction values in $2.92 \leq m_{\mathrm{inv.,\ e^+e^-}} \leq 3.16$ GeV/c^2 for minimum bias events. S/B denotes the signal over total background counts.

The raw signal count as a function of p_{T} is plotted in the left panel of figure 5.21. To obtain the differential yield, the raw signal count is divided by the rapidity interval, the p_{T} bin width and the fraction of J/ψ decaying into electrons, i.e the branching ratio. The branching ratio through the di-electron channel is [29]:

$$\mathrm{BR}_{\mathrm{J}/\psi\to\mathrm{ee}} = (5.971 \pm 0.032)\% \,. \tag{5.12}$$

The differential raw yield is shown in the right panel of figure 5.21.

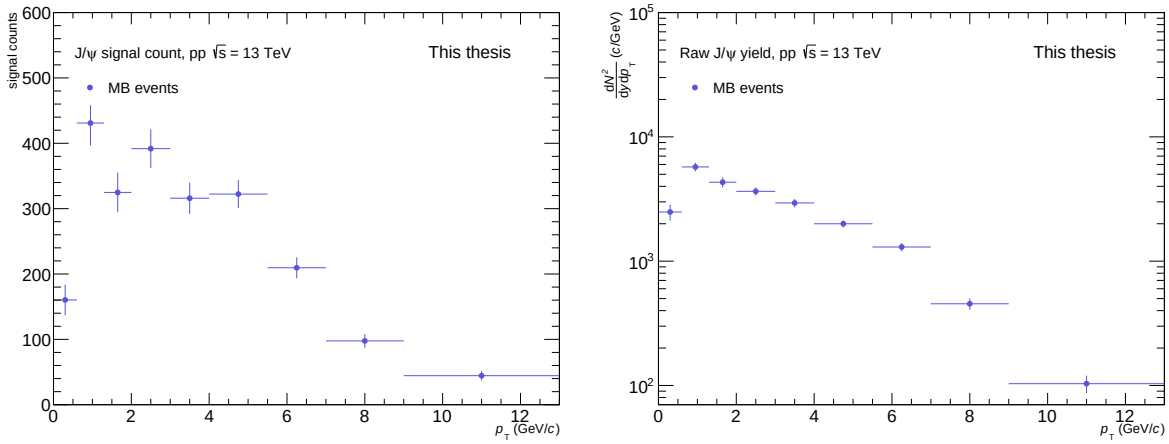

FIGURE 5.21: The raw J/ψ signal count to the left, and to the right the raw yield including corrections for Δy, $\Delta\ p_{\mathrm{T}}$, and branching ratio.

5.6 Acceptance and efficiency

Not all particles passing through the detector are reconstructed, due to the detector geometry, dead zones, noisy channels, imperfect efficiency, etc. To obtain the J/ψ yield produced in the collision one must correct for this signal loss, due to the detector acceptance and efficiency. The geometrical acceptance refers to a purely geometric fiducial volume of the detector, indicating the fraction of signal events visible to a detector due to its geometry. The reconstruction efficiency refers to the effectiveness of the detector in finding objects which have passed through the detector acceptance.

A J/ψ enhanced Monte Carlo sample, as introduced in section 5.2.2, is used to evaluate the acceptance and efficiency. The MC simulation reproduces all running conditions of the corresponding data set, but with additional J/ψ mesons added on top of the MB event. The same event (section 5.3) and track selection (section 5.4) cuts are performed on both data and MC samples. This makes it possible to calculate the acceptance and efficiency from the MC sample, as both the number of generated and reconstructed J/ψ candidates are available. As the same selection cuts are performed on data and MC, it is important that the reconstruction performance of the MC sample corresponds well with the data. Comparison between data and MC after applied cuts was

described in section 5.2.3, as well as a data-driven calibration on $n\sigma_e$ for problematic periods (section 5.4.4). Additionally, a re-weighting of the injected J/ψ p_{T} spectrum in MC was performed, section 5.2.2. Thus, a good description of data by MC is ensured.

The total acceptance and efficiency is retrieved from the simulation by determining the fraction of reconstructed, validated J/ψ mesons, i.e. electron pairs passing all selection criteria, to the number of generated J/ψ candidates. The correction is determined for each period individually, and applied as a weighted average, using the corrected number of events in data (table A.1 - A.2) as weights. The weighted average is calculated as

$$(\mathscr{A} \times \mathscr{E})_{\text{average}} = \sum_i W_i \cdot (\mathscr{A} \times \mathscr{E})_i \,, \tag{5.13}$$

where $(\mathscr{A} \times \mathscr{E})_i$ is the calculated acceptance times efficiency according to equation 5.17 for period i. Here, W_i is the weight factor,

$$W_i = \frac{(N^{\text{corr.}}_{\text{V0AND}})_i}{\sum\limits_j \left(N^{\text{corr.}}_{\text{V0AND}}\right)_j} \,, \tag{5.14}$$

where $(N^{\text{corr.}}_{\text{V0AND}})_i$ is the corrected number of events for period i. Figure 5.22 shows the calculated acceptance and efficiency for the p_{T} integrated case for each period.

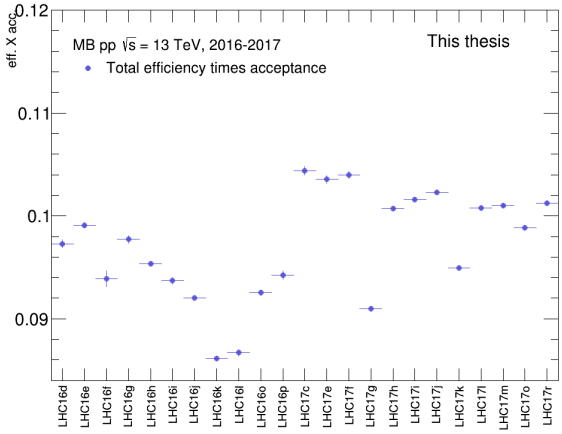

FIGURE 5.22: Efficiency and acceptance as a function of the period number.

The total acceptance and efficiency after the calculation of the weighted average according to equation 5.13 is

$$(\mathscr{A} \times \mathscr{E}) = (9.6 \pm 0.004)\% \,.$$

To get a better understanding of the different contributions to the total efficiency, the following factorization is introduced,

$$(\mathscr{A} \times \mathscr{E}) = \frac{\mathrm{N}_{\mathrm{J}/\psi(\mathrm{rec.sim})}}{\mathrm{N}_{\mathrm{J}/\psi(\mathrm{gen.sim})}} \tag{5.15}$$

$$= \frac{\mathrm{N}_{\mathrm{J}/\psi,\text{gen, kinematic cuts}}}{\mathrm{N}_{\mathrm{J}/\psi,\text{gen}}} \cdot \frac{\mathrm{N}_{\mathrm{J}/\psi,\text{rec, tracking cuts}}}{\mathrm{N}_{\mathrm{J}/\psi,\text{gen, kinematic cuts}}}$$

$$\cdot \frac{\mathrm{N}_{\mathrm{J}/\psi,\text{rec, tracking + PID cuts}}}{\mathrm{N}_{\mathrm{J}/\psi,\text{rec, tracking cuts}}} \cdot \frac{\mathrm{N}_{\mathrm{J}/\psi,\text{rec, tracking + PID + mass window cuts}}}{\mathrm{N}_{\mathrm{J}/\psi,\text{rec, tracking + PID cuts}}} \tag{5.16}$$

$$= \mathscr{A} \cdot \varepsilon_{\text{track}} \cdot \varepsilon_{\text{PID}} \cdot \varepsilon_{\text{mass}} \,. \tag{5.17}$$

Geometric acceptance, $\mathscr{A}$: The geometric acceptance is defined by the kinematic selection cuts described in section 5.4.1.
Track efficiency, $\varepsilon_{\text{track}}$: The efficiency of the track reconstruction determines the probability that both decay daughter tracks (in the acceptance) are reconstructed and pass the tracking cuts in 5.4.2. (Due to the technical setup of this analysis, a loose PID cut of $n\sigma_e \pm 5$ is applied in addition to the tracking cuts.)
PID efficiency, ε_{PID}: The efficiency of particle identification is the probability that both reconstructed tracks pass as electron track candidates, based on the PID selection of 5.4.3.
Signal mass window efficiency, $\varepsilon_{\text{mass}}$: The mass window efficiency is the probability that reconstructed J/ψ mass is within the mass signal region.

Figure 5.23 shows the total acceptance and efficiency of the J/ψ as a function of p_{T}, as well as the different contributions.

The geometric acceptance shown in red points shows a strong pair p_{T} dependence. This is due to the p_{T} selection of the daughter tracks. Due to the J/ψ mass, no daughter tracks with p_{T} below 1 GeV/c are possible. For higher p_{T} the decay particles are boosted in the direction of the J/ψ momentum, and a significant fraction of the electron-pairs have a large opening angle. This leads to daughter tracks with one track within the acceptance and one track with p_{T} below the kinematic acceptance cut value, thereby reducing the acceptance. For pairs with p_{T} larger then 2 GeV/c the fraction of pairs with large opening angle decreases, thus increasing the acceptance.

The track selection is not 100% efficient, due to the fact that tracks may be lost during seeding, or rejected due to bad readout quality. A weakly decreasing p_{T} dependence is observed for the tracking efficiency, shown in yellow.

The largest reduction in the total efficiency comes from the PID selection, depicted in green. The shape of the PID efficiency is caused by the interplay of the pion and proton exclusion cuts. At low p_{T} there is no influence of the pion band. Around 1 GeV/c there is a dip in the efficiency caused by the proton rejection, as there is a crossing of the proton and electron line in the $\mathrm{d}E/\mathrm{d}x$. For higher p_{T} the efficiency decreases due to the relativistic rise of the pion energy loss closing in on the electron band.

The efficiency of the signal mass window is shown in magenta. There is a slight p_{T} dependence due to the fact that the applied tracking cuts differ in how well they remove conversion electrons in different pair -p_{T} regions.

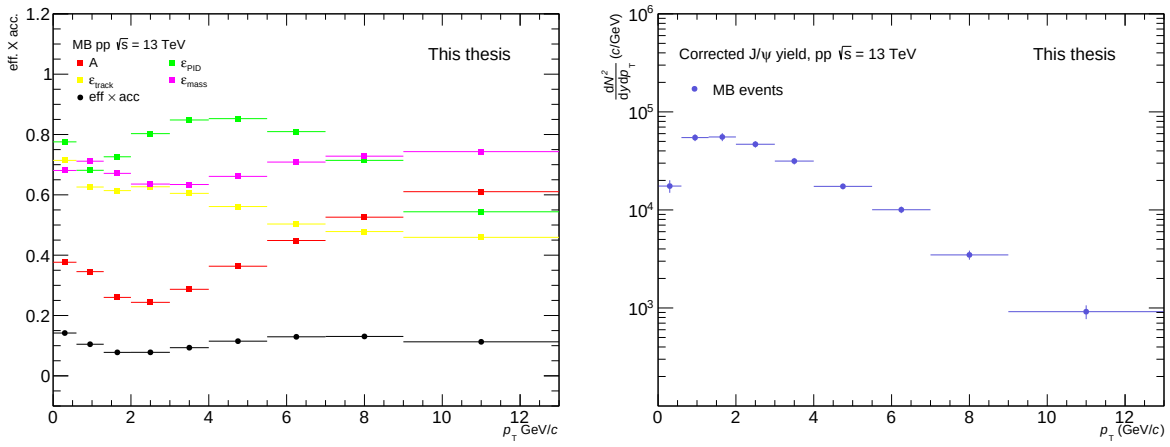

FIGURE 5.23: *Left*: Efficiency and acceptance as a function of transverse momentum. The total acceptance times efficiency is displayed in black and the different efficiency components in color. In red, the geometric acceptance, in yellow the tracking efficiency, in green the PID efficiency and in magenta the efficiency of the signal mass window. *Right*: The corrected J/ψ yield as a function of p_{T}.

5.7 Inclusive J/ψ cross section

The p_{T}- differential cross section of inclusive J/ψ is determined by:

$$\frac{\mathrm{d}\sigma^2}{\mathrm{dyd}p_{\mathrm{T}}} = \frac{\mathrm{N}_{\mathrm{raw}}^{\mathrm{J}/\psi}}{(\mathscr{A} \times \mathscr{E})\mathrm{BR}_{\mathrm{J}/\psi\to\mathrm{ee}} \cdot \Delta\mathrm{y} \cdot \Delta p_{\mathrm{T}}} \cdot \frac{\sigma_{\mathrm{V0AND}}}{\mathrm{N}_{\mathrm{V0AND}}^{\mathrm{corr.}}}, \tag{5.18}$$

where

- $\mathrm{N}_{\mathrm{raw}}^{\mathrm{J}/\psi}$ is the number of J/ψ obtained from the signal extraction (section 5.5)
- $\mathscr{A} \times \mathscr{E}$ is the acceptance and efficiency correction factor (section 5.6)
- $\mathrm{BR}_{\mathrm{J}/\psi\to\mathrm{ee}}$ is the branching fraction of decay J/$\psi \to ee$ (section 5.5.3)
- Δy is the rapidity window, being 1.8 as $|y| < 0.9$

- Δp_{T} is the width of the respective p_{T} bin
- $\mathrm{N}^{\mathrm{corr.}}_{\mathrm{V0AND}}$ the number of triggered events (table: 5.3.2)
- σ_{V0AND} is the cross section taken from Van der Meer scan (section 5.3.2)

Figure 5.24 shows the differential cross section obtained using the total cross section, σ_{V0AND} from the 2015 van der Meer scan. The total p_{T} integrated cross section is

$$\frac{\mathrm{d}\sigma}{\mathrm{d}y} = 9.46 \pm 0.28\,(\mathrm{stat})\ \mu\mathrm{b}\,. \tag{5.19}$$

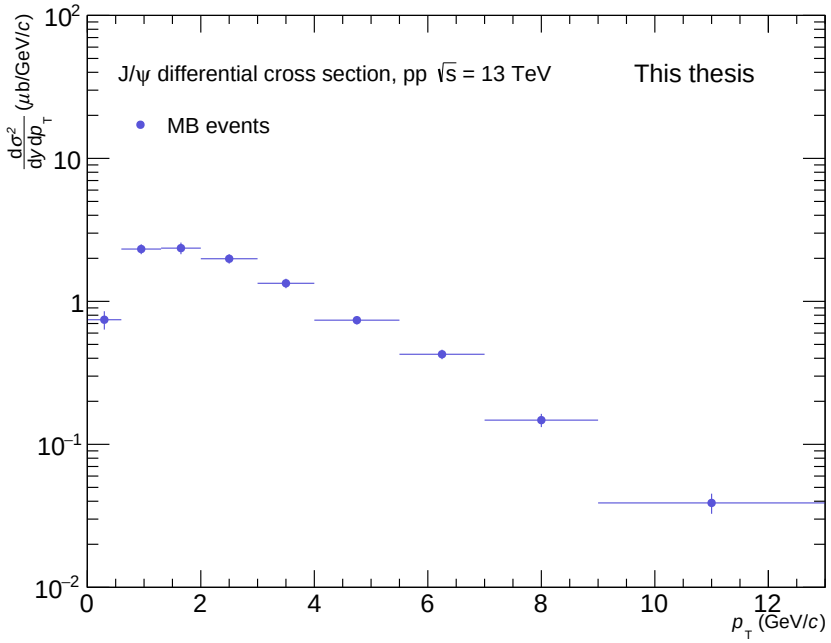

FIGURE 5.24: Inclusive J/ψ cross section as a function of p_{T}.

Chapter 6

Systematic uncertainties

In this chapter, the systematic uncertainty of the cross section measurement is presented. The different contributions to the systematic uncertainty are discussed, as well as the methods used to estimate these uncertainties. The estimation of the systematic uncertainty is carried out using the same procedure for both the p_{T} differential and the p_{T} integrated cases. Thus, the procedure will only be presented for the p_{T} integrated case and a summary of the results including the p_{T} differential uncertainty can be found in section 6.5. The systematic uncertainty plots for all p_{T} bins can be found in appendix C.

The systematic uncertainty of the inclusive J/ψ cross section measurement has different sources. For this analysis, the uncertainties associated with the track reconstruction, PID, and signal extraction are investigated. In addition, a global systematic uncertainty is assigned to the measurement due to the uncertainty of the luminosity and the branching ratio. Due to limited statistics in the lowest p_{T} bin, $0.0 \leq p_{\mathrm{T}} < 0.6$ GeV/c^2, the two lowest bins are merged when determining the different systematic uncertainty contributions in bins of p_{T}. The relative uncertainty obtained is then assigned to both bins. In this manner, statistical fluctuations are minimized in order to not artificially increase the systematic uncertainty.

For this analysis, several of the contributions to the systematic uncertainty are determined by a cut variation method. Hereby, the cross section measurement is repeated for different cut selections, e.g. variations of the PID cuts. The measured results are then compared to the results obtained for the standard cut setting. For each variation, a deviation from the standard case is computed according to

$$\Delta Y = \frac{Y - Y_{\mathrm{standard}}}{Y_{\mathrm{standard}}}, \tag{6.1}$$

where Y and Y_{standard} are the measured values for a certain cut variation and the standard cut, respectively. The statistical uncertainty of the deviation is computed as proposed by Barlow [73]:

$$\delta_{\Delta Y} = \sqrt{|\delta_Y^2 - \delta_{Y_{\mathrm{standard}}}^2|}\,. \tag{6.2}$$

According to this criterium, a deviation is considered statistically significant if it does not agree with the standard case within the uncertainty. In principle, only statistically significant deviations

should be included when determining the systematic uncertainty. However, for this analysis, a conservative approach is used, where all considered cut variations are included in the calculation of the systematic uncertainty.

6.1 Tracking

Imperfect knowledge of the track reconstruction performance can lead to a systematic uncertainty of the measured cross section. The estimation of this uncertainty is split into two contributions, namely the contribution due to track quality selections and the efficiency of the track matching between the TPC and the ITS. The uncertainty connected with the quality selection is determined by cut variations, while the uncertainty estimation due to track matching makes use of a simplified MC simulation.

6.1.1 Tracking quality selection

The MC sample is used to determine the detector acceptance and efficiency. Thus, a mismatch between the tracking performance in data and MC will add a systematic uncertainty to the measured cross section. The systematic uncertainty associated with the tracking quality selection is estimated by a variation of the main track quality requirements described in section 5.4.2. Most of these cuts are chosen to be open enough to not introduce any systematic effect. Stricter cut requirements are used on hits in the SPD layers, the distance of closest approach to the primary vertex, and the maximum number of shared clusters in the ITS. In order to determine the systematic uncertainty of the track selection, the strict cuts are varied in both data and MC. All possible combinations of the cut variations listed under "tracking" in table 6.1 are considered. For each considered cut variation, the whole analysis is repeated. Hence, the efficiency and acceptance is re-calculated and used to obtain the cross section. The p_{T} integrated cross sections obtained for different cut variations are shown in figure 6.1. The tracking cut selections are labeled in a manner similar to *SPDfirst_ITSShared1_DCAxy50DCAz200* corresponding to a cut using the requirements SPDfirst, i.e. tracks associated with one or more clusters in the first SPD layer, at most 1 shared cluster for the ITS tracks and DCA cuts of 0.5 and 2 cm for xy and z, respectively. Figure 6.2 shows the relative deviation according to equation 6.1 of the obtained cross sections with respect to the standard tracking cut selection for the p_{T} integrated case. Deviations from the standard cut case of up to 4% are observed, some of which deviate significantly from the standard case as depicted by the dashed line at zero deviation. As previously mentioned, a conservative approach is used for the uncertainty estimation where all considered cut variations are included. In figure 6.3 the p_{T} integrated cross section distribution is shown, where each tracking cut variation adds one entry to the distribution. The RMS of this distribution, i.e. the standard deviation, is calculated according to

$$\mathrm{RMS} = \sqrt{\frac{1}{N}\left(\sum_{i=1}^{N}(x_i - \bar{x})^2\right)}, \tag{6.3}$$

where N is the total number of entries, i.e. tracking cut variations, x_i is the cross section value of entry i, and $\bar{x}$ is the mean value of the distribution. The measured RMS is used as the systematic uncertainty of the tracking quality. The RMS for the p_{T} integrated case amounts to 147.8 nb corresponding to a relative uncertainty of about 1.6%. The p_{T} differential RMS values range from 1.0 to 109.0 nb, corresponding to relative uncertainties ranging from 1.2-6.8%. The relative uncertainties can be found in table 6.3. The p_{T} differential cross sections are found in figures C.1 and C.2. Figure C.3 shows the cross section distributions for the respective p_{T} bins.

	Standard	Variations
Tracking		
SPD	$\mathrm{SPD}_{\mathrm{any}}$	$\mathrm{SPD}_{\mathrm{first}}$
ITS $N_{\mathrm{cls.}}$ shared	≤ 1	$\leq 0, 2, 3$
$\lvert\mathrm{DCA}_{xy}\rvert$	< 0.5 cm	$< 1, 0.3$ cm
$\lvert\mathrm{DCA}_{z}\rvert$	< 2 cm	$< 3, 1$ cm
PID		
TPC $n\sigma_e$	$\in [-3.0, 3.0]$	$\in [-2.0, 3.0], [-3.5, 3.0], [-3.0, 2.0], [-3.0, 3.5]$
TPC $n\sigma_p$	> 3	$> 2.5, 3.5$
TPC $n\sigma_\pi$	> 3	$> 2.5, 3.5$
Signal extraction	[GeV/c^2]	[GeV/c^2]
Signal window	$[2.92, 3.16]$	$[2.88, 3.16], [2.84, 3.16], [2.80, 3.16], [2.76, 3.16],$ $[2.92, 3.12], [2.88, 3.12], [2.84, 3.12], [2.80, 3.12], [2.76, 3.12]$ $[2.92, 3.08], [2.88, 3.08], [2.84, 3.08], [2.80, 3.08], [2.76, 3.16]$
Bkg fit range	[GeV/c^2]	[GeV/c^2]
pol 2	$[1.48, 4.52]$	$[1.48, 4.40], [1.48, 4.76], [1.48, 5.00], [1.72, 5.00]$ $[1.72, 4.52], [1.84, 4.52], [1.96, 4.52], [1.96, 4.40]$
exponential	$[1.48, 4.52]$	$[1.48, 4.40], [1.48, 4.76], [1.48, 5.00], [1.00, 5.00]$ $[1.00, 4.52], [1.24, 4.52], [1.60, 4.52], [1.60, 4.40]$

TABLE 6.1: Applied cut variations for tracking and PID cuts, signal window variations and the variations applied for the background fit range. The fit range variations are shown separately for the second order polynomial and the exponential fit functions. The second column shows the standard choice, while the third column shows the considered variations.

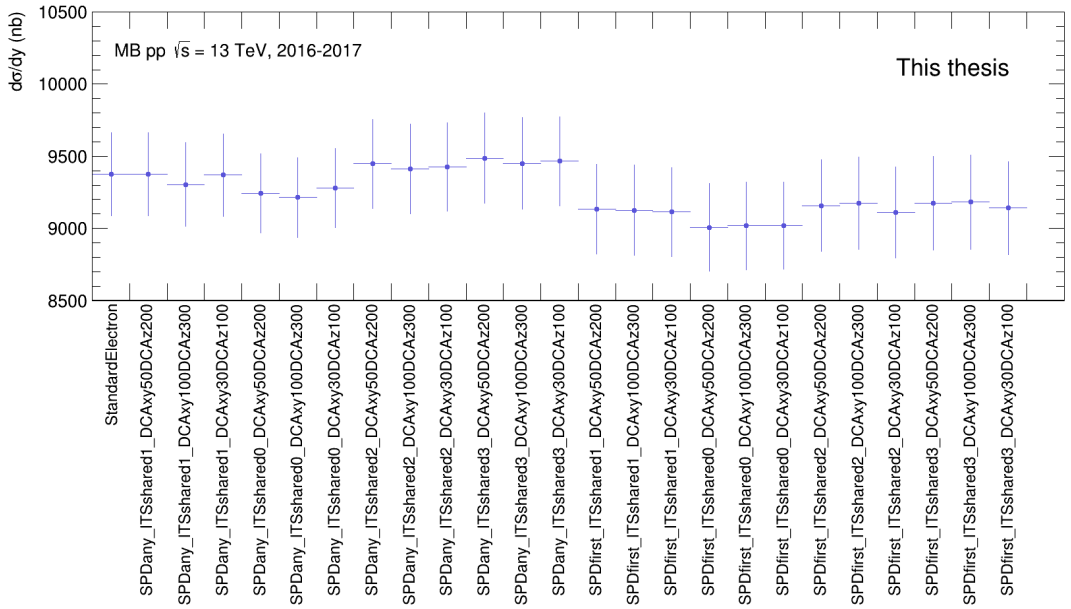

FIGURE 6.1: The p_{T} integrated inclusive J/ψ cross section obtained for each tracking cut configuration.

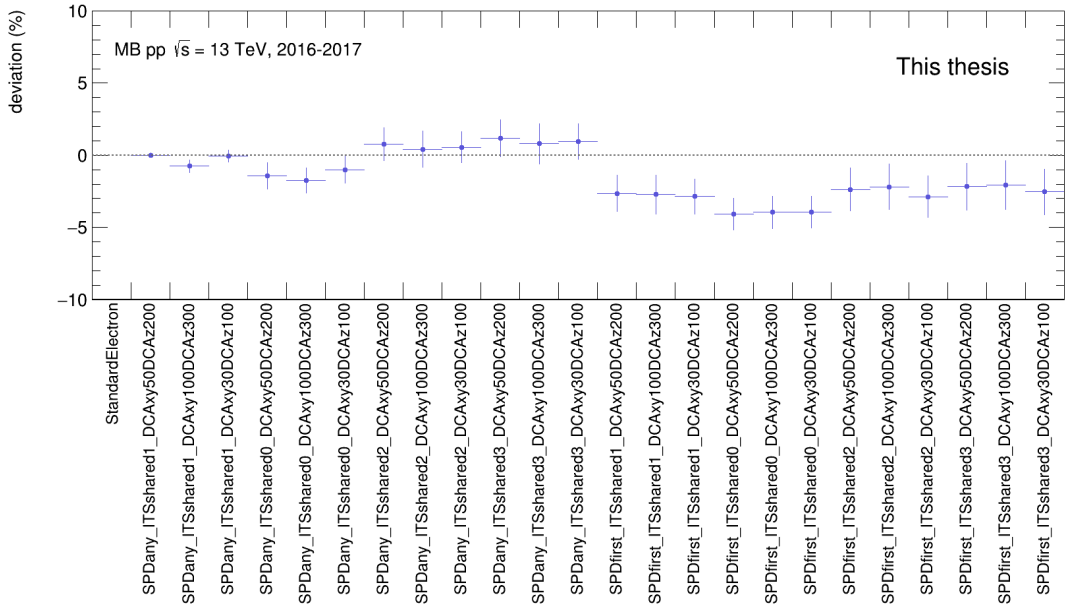

FIGURE 6.2: The relative deviation from the cross section obtained with the standard cut for each track cut variation.

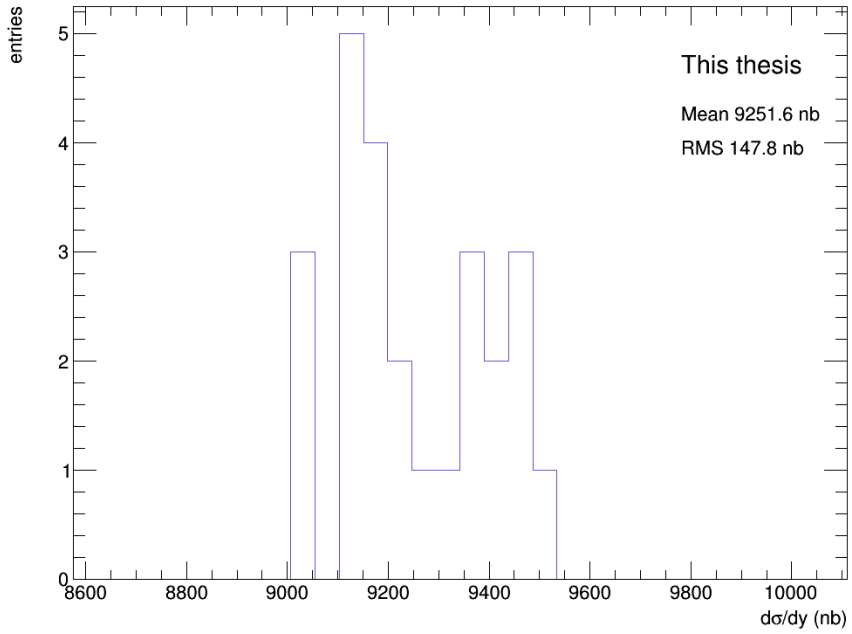

FIGURE 6.3: Distribution of p_{T} integrated cross sections for all considered track cut variations.

6.1.2 ITS-TPC matching

The systematic uncertainty related to the matching efficiency between ITS tracks and TPC tracks is determined following the method presented in [74]. Here a simplified MC simulation, referred to here as a toy MC, is used to determine the impact of the uncertainty due to the track matching efficiency on the acceptance of the J/ψ. In the toy MC, J/ψ mesons are generated according to a natural p_{T} spectrum built using an input shape obtained from a power law fit of the p_{T} differential cross section, presented in section 5.7,

$$f\left(p_{\mathrm{T}}\right) = A \cdot \frac{p_{\mathrm{T}}}{\left(1 + \left(\frac{p_{\mathrm{T}}}{p_0}\right)^2\right)^n}\,, \tag{6.4}$$

where A, p_0, and n are fit parameters. The fit to the cross section is shown in the top left panel of figure 6.4 together with the obtained fit parameters. The fit describes the data sufficiently with a $\chi^2/\mathrm{ndf} = 1.62$. The fit agrees with data within $\pm 20\%$ as can be seen in the lower panel of figure 6.4 showing the ratio between data and fit.

The J/ψ mesons are generated within a rapidity range of $|y| < 0.9$ according to a Gaussian rapidity distribution centered around 0 with a σ of 2. The J/ψ decay into electrons and positrons is simulated such that the particles are selected to be within the geometric acceptance of the ALICE central barrel.

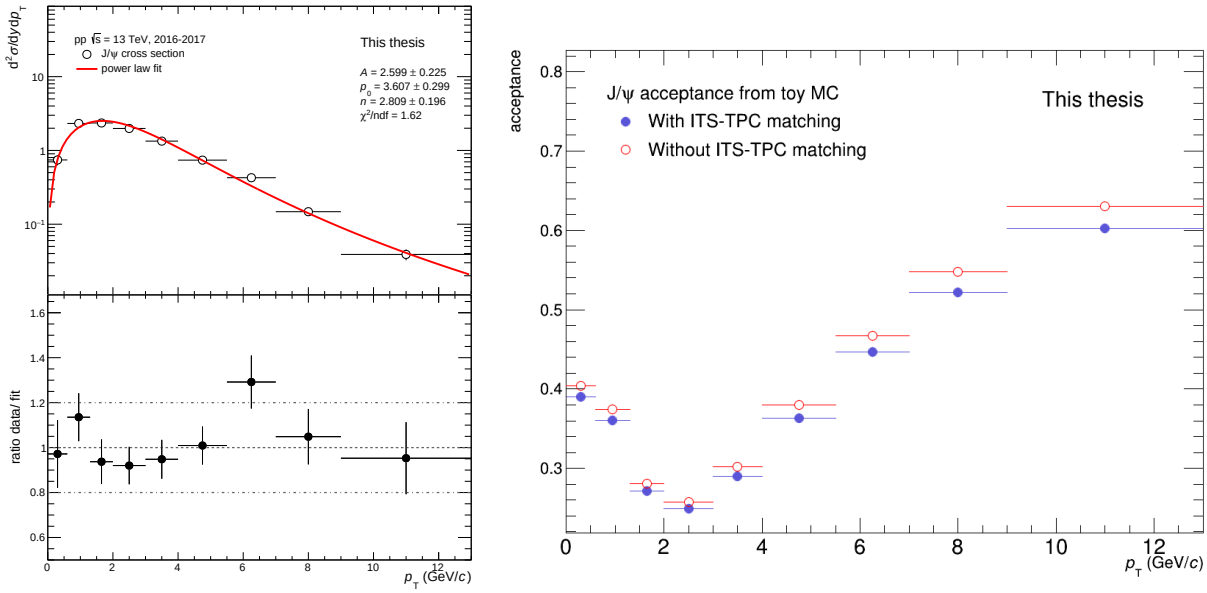

FIGURE 6.4: *Left:* Inclusive J/ψ cross section and a power law fit in the top panel and the ratio data to fit in the bottom panel. *Right:* Generated J/ψ acceptance with and without the matching efficiency in blue and red, respectively.

The right panel of figure 6.4 shows the J/ψ acceptance obtained from the toy MC in red. In order to determine the systematic uncertainty of the track matching on the J/ψ cross section another toy MC is performed using the systematic uncertainty of ITS-TPC matching efficiency for single tracks as input. In this manner, the impact of the matching efficiency uncertainties on the calculated acceptance can be studied.

The systematic uncertainties of the single track efficiencies are obtained from [75] for periods LHC16d-p and LHC17c,e,f,g, and j. Efficiencies for the remaining 2017 periods are not available. The efficiency uncertainties for the available periods are reasonably stable and the weighted average of the available periods can thus be used to describe all data periods. The weighted average is calculated in the same manner as described for the efficiency and acceptance in section 5.6. For the first and last p_{T} bins, no single track matching efficiency is available. Therefore the value from neighboring bins is used. The relative uncertainty of single track efficiencies as a weighted average for each p_{T} bin is shown in table 6.2.

p_{T} bin [GeV/c]	0-0.8	0.8-1.	1.-2.	2.-3.	3.-4.	4.-6.	6.-8.	8.-15.	$> 15.$
Matching eff. (%)	0.82	0.82	1.45	2.22	2.27	2.10	2.05	2.26	2.26

TABLE 6.2: The relative uncertainty of track matching efficiency between ITS and TPC for single tracks obtained as a weighted average of periods LHC16d-p and LHC17c,e,f,g, and j. The systematic uncertainties of the single track efficiencies for each period are taken from [75].

In order to quantify the impact of the matching efficiency on the measured J/ψ cross section, the

systematic uncertainty of single track efficiencies is used as input for the toy MC. The effect of the matching efficiency uncertainties is emulated in the toy MC by randomly rejecting decay particles with an efficiency of (1-X), where X is the single track matching uncertainties listed in table 6.2. Thus, the simulated acceptance is slightly reduced due to the uncertainty of the matching efficiency for single tracks. The obtained acceptance including the impact of the matching efficiency is shown in blue in figure 6.4. The difference between the acceptance with and without the ITS-TPC matching efficiency is calculated according to

$$\Delta\mathscr{A} = 2 \cdot \frac{\left(\frac{1}{\mathscr{A}_{\text{Without}}} - \frac{1}{\mathscr{A}_{\text{With}}}\right)}{\left(\frac{1}{\mathscr{A}_{\text{Without}}} + \frac{1}{\mathscr{A}_{\text{With}}}\right)}, \tag{6.5}$$

and is used as the systematic uncertainty for each p_{T} bin. For the p_{T} integrated case, the systematic uncertainty is about 3.9%. The p_{T} differential relative systematic uncertainties associated with the matching efficiency range from 3.3 to 4.8% and can be found in table 6.3. For most of the p_{T} bins, the value is approximately twice the systematic uncertainty obtained for single tracks, which is what one would naively expect for two electrons reconstructed independently.

The total systematic uncertainty assigned due to tracking is calculated as the quadratic sum of the contributions from track selections and the matching efficiency yielding about 4.2% for the p_{T} integrated cross section and approximately 4.3% to 7.7% for the p_{T} differential case.

6.2 TPC PID

The systematic uncertainty related to the PID is estimated following the procedure of cut variations, similar to what was described for the tracking quality selection. The electron inclusion cut is varied as well as the proton and pion rejection cuts. The considered cut variations can be found in table 6.1 under "PID". Figure 6.5 shows the p_{T} integrated cross section obtained for the different PID selections. The selections are labeled in a manner similar to *electron0_proton0_pion1* corresponding to a cut using the standard electron and proton value and the strict pion rejection cut of 2.5, while *electron0_proton0_pion2* corresponds to the loose pion cut of 3.5.

Most of the integrated cross sections shown in figure 6.5 are compatible within statistical fluctuations with the standard case. The relative deviations according to equation 6.1 are shown in figure 6.6, where a maximum deviation of about 4% is observed. As in the tracking case, some of the cut variations deviate significantly from the standard case which is depicted by the dashed line at zero. Again a conservative approach is used, including all PID variations when determining the systematic uncertainty. The distribution of p_{T} integrated cross sections for all PID variations is shown in figure 6.7. The RMS of this distribution is assigned as the systematic uncertainty for the PID. In the p_{T} integrated case, the RMS is 108.1 nb, corresponding to a relative uncertainty of about 1.2%. The systematic uncertainty associated with the PID is not bin-to-bin correlated,

i.e. the uncertainty is p_{T} dependent as the energy loss in the TPC depends on the momentum. At low p_{T}, the systematic uncertainty contribution is 3.78%, while the contribution in the p_{T} region 1.3-3 GeV/c is around 3.5% due to the proton rejection cut. At high p_{T}, the PID selection is highly influenced by the pion rejection cut and the systematic uncertainty ranges from about 3-5%. The p_{T} differential RMS values range from 1.8 to 81.1 nb and the cross section and associated distributions can be found in appendix C.10 and C.11.

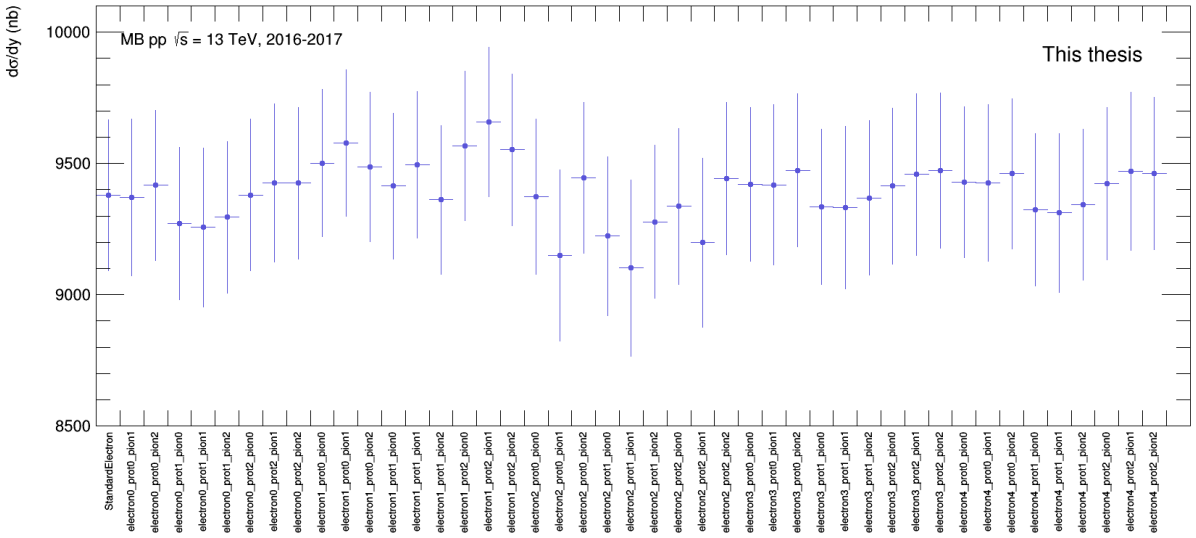

FIGURE 6.5: The p_{T} integrated inclusive J/ψ cross section obtained for each PID cut configuration.

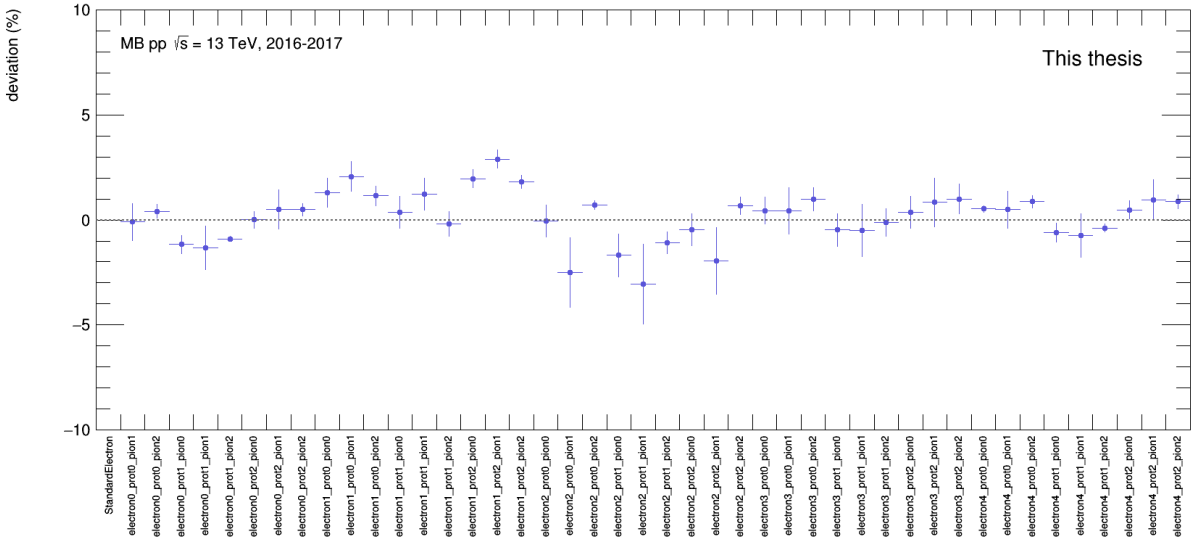

FIGURE 6.6: The relative deviation from the cross section obtained with the standard cut for each PID cut variation.

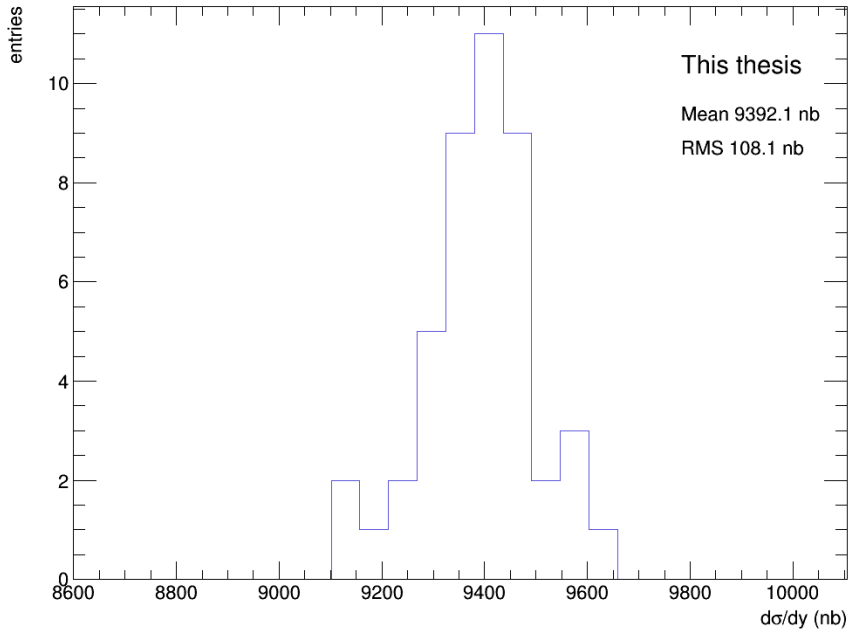

FIGURE 6.7: Distribution of p_{T} integrated cross sections for all considered PID cut variations.

6.3 Signal extraction

The J/ψ signal extraction, as described in 5.5, is based on bin counting in the signal window $2.92 \leq m_{\mathrm{inv.,\ e^+e^-}} \leq 3.16$ GeV/c^2, to determine the number of J/ψ mesons. The background is estimated using a hybrid method relying on the J/ψ signal shape obtained from MC. The MC signal shape is hereby used to describe the low mass tail of the J/ψ signal, originating from electron and positron energy loss. A possible mismatch between the signal shape in data and MC is thus considered as a possible source of systematic uncertainty. In addition, the background estimation may contribute to the systematic uncertainty of the signal extraction.

6.3.1 Signal shape

To determine the systematic uncertainty corresponding to the signal shape, the mass signal window is varied. The considered variations can be found in table 6.1 under "signal extraction". A total of 15 different signal windows are chosen, where the upper and lower limits are varied in steps of 0.04 GeV/c^2, with 3 and 5 variations, respectively. This is a conservative choice inspired by the cross section analysis performed in [74].

Additionally, there might be a bias of the signal shape by the track selection criteria. The signal window variations are therefore repeated for all tracking cut variations mentioned in section 6.1.1. Figure 6.8 shows the relative deviations of the p_{T} integrated cross sections for each tracking cut variation along the x-axis and the different signal extraction windows and fit variations (further described in section 6.3.2) along the y-axis. The signal window variations show a deviation of at most 4.5% for the p_{T} integrated case. The relative deviation for the p_{T} differential cross sections can be found in appendix C.4.

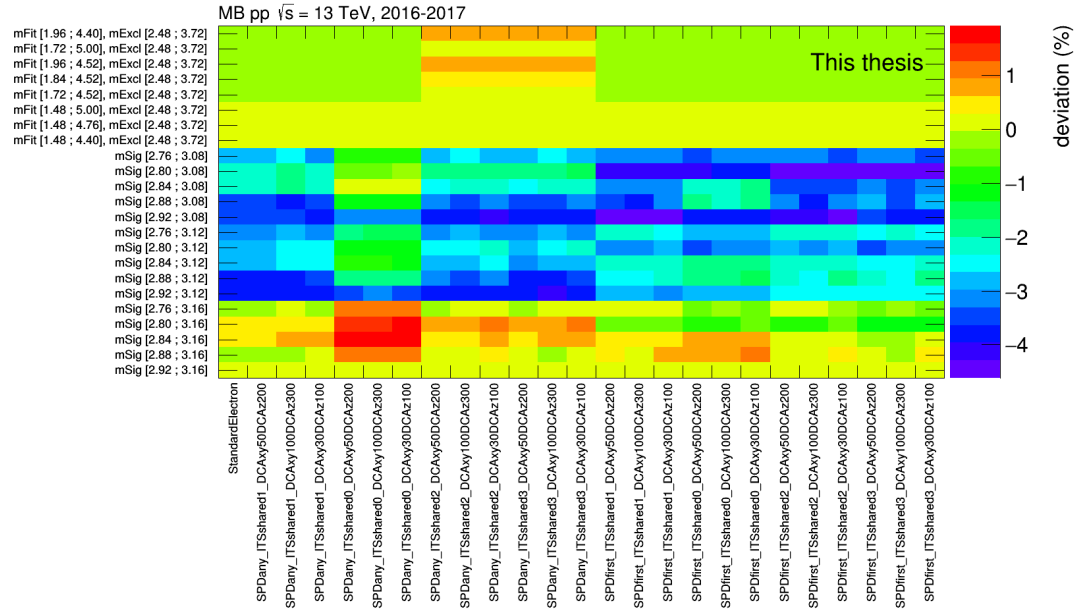

FIGURE 6.8: The relative deviation of the p_{T} integrated cross sections in percent for each tracking cut variation along the x-axis and every signal extraction variation along the y-axis.

Figure 6.9 shows the cross section distribution due to signal window variations for each tracking cut for the p_{T} integrated case. Each of the 15 signal variations gives one entry for each of the tracking cut variations along the x-axis. The black points are the mean of the distribution along the y-axis and the error bars are the corresponding RMS values. The distribution of RMS values is shown in the left panel of figure 6.10, where the mean is taken to be the systematic uncertainty of the signal counting window. Thus, the systematic uncertainty assigned for the p_{T} integrated case is 144.9 nb corresponding to a relative uncertainty of approximately 1.5%. The signal shape is assumed to be bin-to-bin correlated, i.e. the signal shape should not depend strongly on p_{T}. In order to minimize the effect of statistical fluctuations when determining the uncertainties in p_{T} bins, the signal window is varied for three larger p_{T} bins, namely 0-2.0 GeV/c, 2.0-5.5 GeV/c and 5.5-13 GeV/c. The relative systematic uncertainties obtained from these bins are assigned to the smaller bins. In order to follow the same procedure for signal extraction as for the cross section measurement, the signal is extracted using a second-order polynomial residual background fit for the p_{T} bin 0-2.0 GeV/c, while the signal for the remaining bins is extracted using an exponential function to describe the residual background. Figure C.5 shows the cross section distribution due to

signal variations for each track cut variation, respectively. The RMS distributions can be found in appendix C.6, with mean values ranging from 3.9 - 40.5 nb corresponding to relative uncertainties ranging from 2.2 - 2.8%. The relative uncertainties can be found in table 6.3.

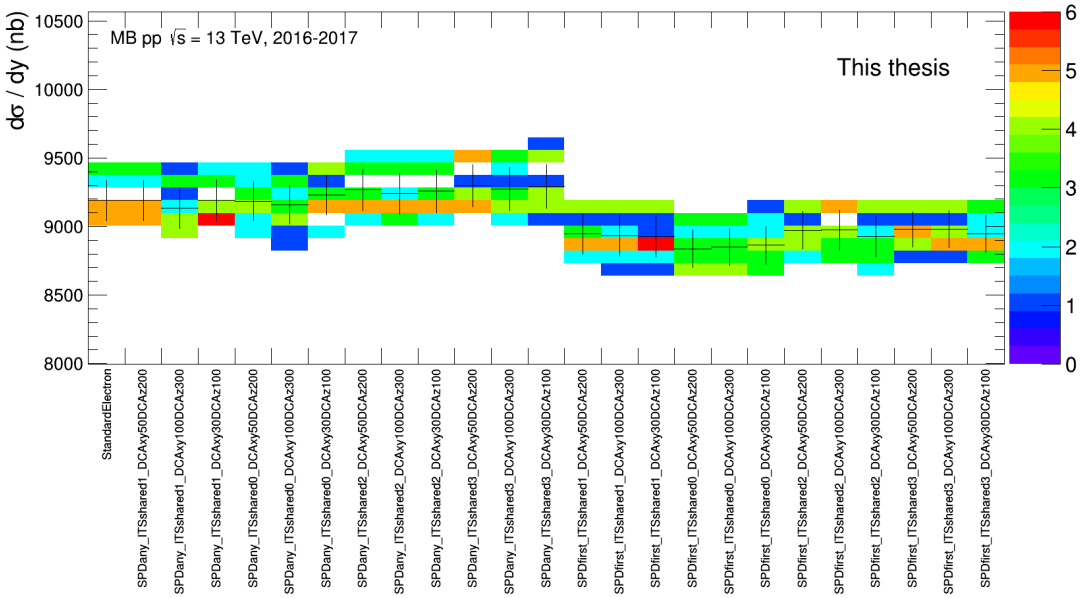

FIGURE 6.9: The distribution of the p_{T} integrated inclusive J/ψ cross section obtained from variations of the signal window for each tracking variation. The mean of the distribution is shown in black points where the uncertainty represents the RMS of the distribution.

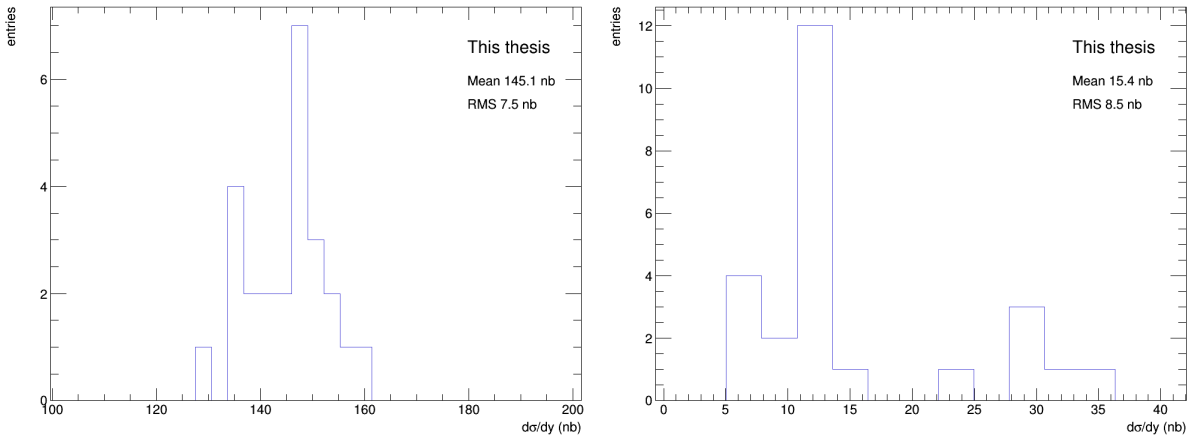

FIGURE 6.10: The RMS distribution obtained from the signal window and fit range variations for the p_{T} integrated case in the left and right panel, respectively. Each of the considered tracking cut settings has one entry in the histograms.

6.3.2 Background determination

The hybrid signal extraction method, as described in section 5.5.2, is used in order to describe both the combinatorial and residual background. The description of the residual background relies on an empirical fit. Possible contributions to the systematic uncertainty associated with the background estimation method as well as the chosen fit range are thus investigated.

Background estimation method

In order to explore a possible systematic uncertainty related to the background estimation method, a full fit method is investigated. The full fit background estimation describes the total background using an empirical fit function in combination with the MC signal shape. Unlike the hybrid method, there is no distinction between combinatorial and residual background using this method. The full fit method is performed using a third order polynomial fit for $p_{\mathrm{T}} < 2$ GeV/c and an exponential in the remaining bins. The left panel of figure 6.11 shows the full fit signal extraction for the p_{T} integrated case with a signal count similar to what is obtained using the hybrid method. The signal extraction for each p_{T} bin using the full fit method can be found in appendix C.5.

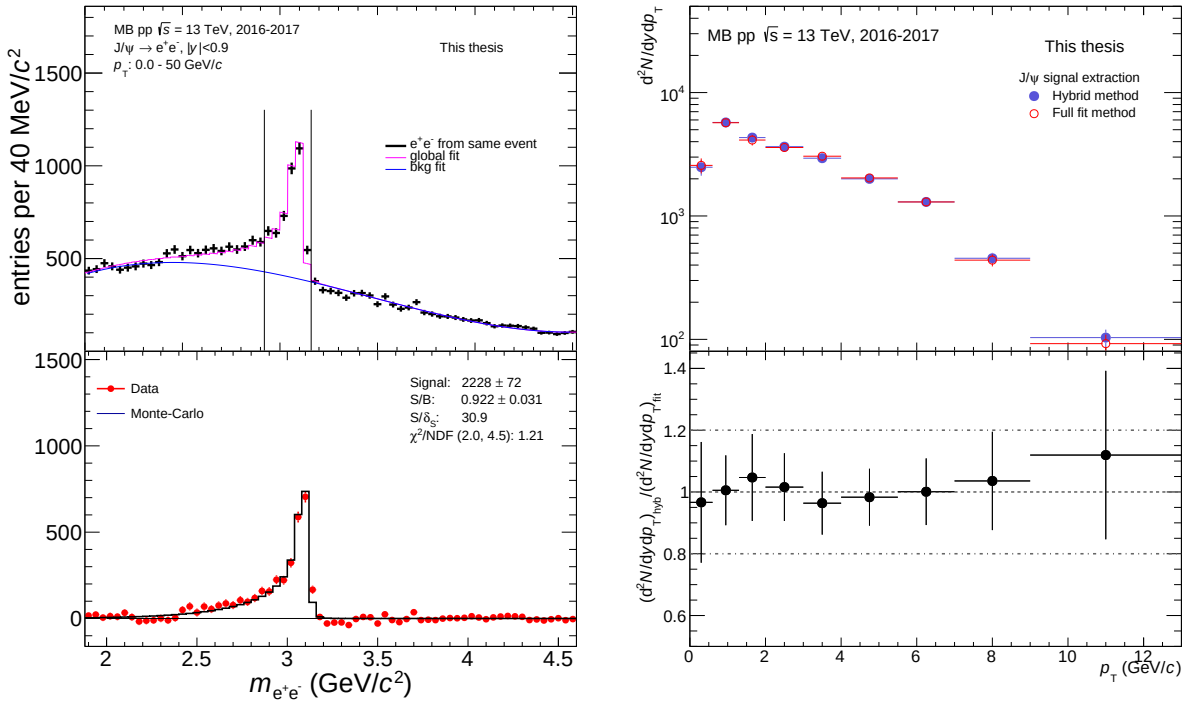

FIGURE 6.11: The left panel shows the signal extraction using the full fit method for the p_{T} integrated case. The right panel shows the extracted raw yield using the hybrid and full fit method in blue and red, respectively. The yield ratio is shown in the lower panel showing good agreement between the methods.

The right panel of 6.11 shows the extracted raw yield obtained using the hybrid and the full fit method. The lower panel shows the ratio between the two yields. Both methods agree well within statistical uncertainties, thus no systematic uncertainty is assigned due to the chosen background method.

Background fit range

The systematic uncertainty associated with the fit range is determined in the same manner as the uncertainty associated with the signal shape, namely by varying the fit range. The signal extraction is performed for a total of 8 different fit ranges in addition to the standard fit range. Due to very different background shapes at low and high p_{T}, second-order polynomial and exponential fit functions are used to describe the different p_{T} ranges. These fit functions behave very differently, and therefore two different sets of fit range variations are considered in order to provide stable fits for all considered variations. The considered ranges can be found in table 6.1. As is done for the signal window variations, the cross section is determined for all fit ranges using all considered track cut variations described in section 6.1.1.

In figure 6.8 the relative deviation of the obtained cross section is shown for each tracking cut variation along the x-axis and the considered fit ranges in the upper 8 bins along the y-axis. The fit variations show relative cross section deviations below 2% for the p_{T} integrated case. The cross section distribution for the p_{T} integrated case determined from variations on the fit range is shown in figure 6.12, with black points showing the mean and the error bars the RMS. The distribution of RMS values for the fit range variations is shown in the right panel of figure 6.10, where the mean is taken to be the systematic uncertainty of the fit range. The uncertainty assigned due to the background fit range is 17.7 nb giving a relative uncertainty of about 0.2% for the p_{T} integrated case. The background shape depends on the considered p_{T} range, thus the fit range is not bin-to-bin correlated, and the systematic uncertainty is determined individually for all p_{T} bins apart from the two lowest p_{T} bins which are merged due to limited statistics in the smallest bin. The RMS distributions of the cross section due to fit range variations can be found in appendix C.7, where the mean corresponds to the systematic uncertainty. The uncertainty ranges from 0.2 - 22.4 nb for the p_{T} bins, corresponding to relative uncertainties of 0.2 - 1.4%, which can be found in table 6.3.

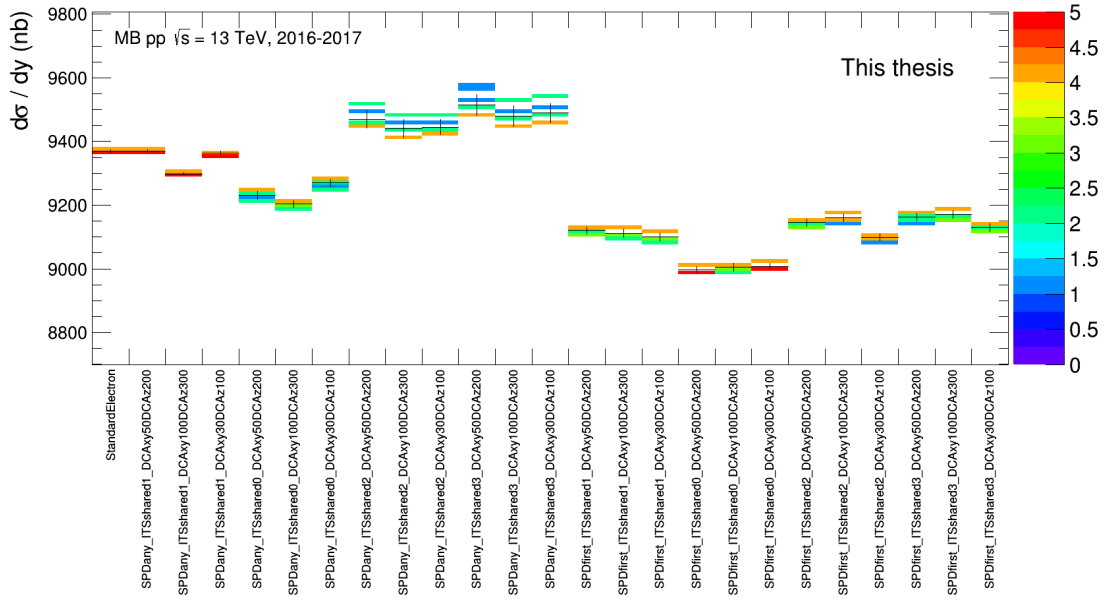

FIGURE 6.12: The distribution of the p_{T} integrated inclusive J/ψ cross section obtained from variations of the fit ranges for each tracking cut variation. The mean of the distribution is shown in black points where the uncertainty represents the RMS.

6.4 Global uncertainties

Luminosity: The luminosity, as described in section 5.3.2, is determined from the cross section obtained from the van der Meer scan and the estimated number of minimum bias events. As the van der Meer cross section values for the 2016 and 2017 data sets are not available, the value for the 2015 data set at $\sqrt{s} = 13$ TeV is used. A conservative uncertainty of 5% is recommended when applying this value to 2016 data [72]. No uncertainty is specified for 2017 data, so the conservative choice of 5% is used as well. In principle, the uncertainty of the estimated number of events within the z vertex requirement of -10 to 10 cm contributes to the uncertainty of the luminosity. For all considered periods the shape of the event distributions is compatible with a Gaussian distribution, and the uncertainty of the event correction is negligible in comparison to the 5% uncertainty of the van der Meer cross section.

Branching ratio: The branching ratio for J/ψ mesons decaying through the di-electron channel is $(5.971 \pm 0.032\%)$ [29]. This corresponds to a global uncertainty for the cross section of 0.53%.

The quadratic sum of the luminosity and branching ratio is assigned as a global uncertainty for the measured J/ψ cross section, amounting to approximately 5%.

6.5 Total systematic uncertainty

The total systematic uncertainty assigned to the J/ψ cross section is obtained by adding the different contributions as a quadratic sum. In total this amounts to an approximately 4.6% uncertainty for the p_{T} integrated case, omitting the global systematic uncertainty. At low p_{T}, the uncertainty is about 8.8% due to a quite high uncertainty associated with the tracking quality selection. The contribution from the fit range variation also increases the total uncertainty in the lowest p_{T} bins. For the intermediate p_{T} range, the total systematic uncertainty is about 6% and at high p_{T} the uncertainty is approximately 7.6%. A summary of the systematic uncertainty and the different contributions can be found in table 6.3.

Source	p_{T} [GeV/c]									
	$p_{\mathrm{T}} > 0$	0-0.6	0.6-1.3	1.3-2	2-3	3-4	4-5.5	5.5-7	7-9	9-13
Tracking										
Cut variations	1.58	6.75	6.75	3.07	2.86	1.18	2.12	2.95	3.76	2.70
ITS-TPC matching	3.86	3.37	3.62	3.38	3.28	4.18	4.46	4.39	4.83	4.51
Total	4.17	7.54	7.66	4.57	4.35	4.34	4.94	5.29	6.12	5.26
PID										
Cut variations	1.15	3.78	3.78	3.45	3.39	2.55	1.42	3.57	2.98	4.78
Signal shape										
Window variations	1.53	2.19	2.19	2.19	2.37	2.37	2.37	2.78	2.78	2.78
Bkg. fit										
Fit range variations	0.16	1.40	1.40	0.80	0.21	0.90	0.48	0.26	0.66	0.43
Total	4.59	8.83	8.93	6.18	6.00	5.64	5.68	6.96	7.38	7.64
Luminosity	5.00									
Branching ratio	0.53									

TABLE 6.3: A summary of systematic uncertainty contributions for the p_{T} integrated and differential inclusive J/ψ cross section. The values are listed in percent.

Chapter 7

Results

In this chapter the results of the inclusive J/ψ cross section measurement at $\sqrt{s} = 13$ TeV at mid-rapidity will be presented. The p_{T} integrated result, as well as the p_{T} differential cross sections will be shown. A model comparison to the energy dependence of the integrated cross section measurement is presented together with p_{T} integrated measurements at different energies. The p_{T} differential cross sections are further compared to previously published ALICE measurements at mid- and forward- rapidity. In addition, comparisons will be done to the preliminary results for the cross section measurement at $\sqrt{s} = 5$ TeV.

7.1 Integrated cross section

The p_{T} integrated inclusive J/ψ cross section at mid-rapidity for pp collisions at $\sqrt{s} = 13$ TeV is found to be

$$\frac{\mathrm{d}\sigma}{\mathrm{d}y} = 9.46 \pm 0.28\,(\mathrm{stat.}) \pm 0.43\,(\mathrm{syst.}) \pm 0.48\,(\mathrm{global})\ \mu\mathrm{b}\,.$$

The systematic uncertainty is stated with two components, namely the total systematic uncertainty without the contribution from global systematic uncertainties and the global uncertainty consisting of the luminosity and branching ratio uncertainty.

Figure 7.1 shows the energy dependence of p_{T} integrated cross section measurements at mid-rapidity together with a model comparison. The model taken from [76] is calculated by employing a small x Color Glass Condensate (CGC) + NRQCD formalism. The calculation is done for prompt J/ψ, while the data points are for inclusive J/ψ measurements. Thus, a direct comparison is not possible. Still, the general tendency is comparable, though the inclusive measurement includes both prompt and non-prompt J/ψ mesons. The data points include measurements from PHENIX [77], Collider Detector at Fermilab (CDF) [78] and ALICE [74,79,80]. The error bars show the quadratic sum of the statistical and systematic uncertainties including the uncertainty of the luminosity. At high center of mass energies all measurements are well within the predicted uncertainty band of the model calculation. At very low $\sqrt{s}$ the inclusive J/ψ measurement is slightly lower than the

model calculation. Overall the energy dependence of the inclusive J/ψ cross section measurements is comparable with the calculated energy dependence.

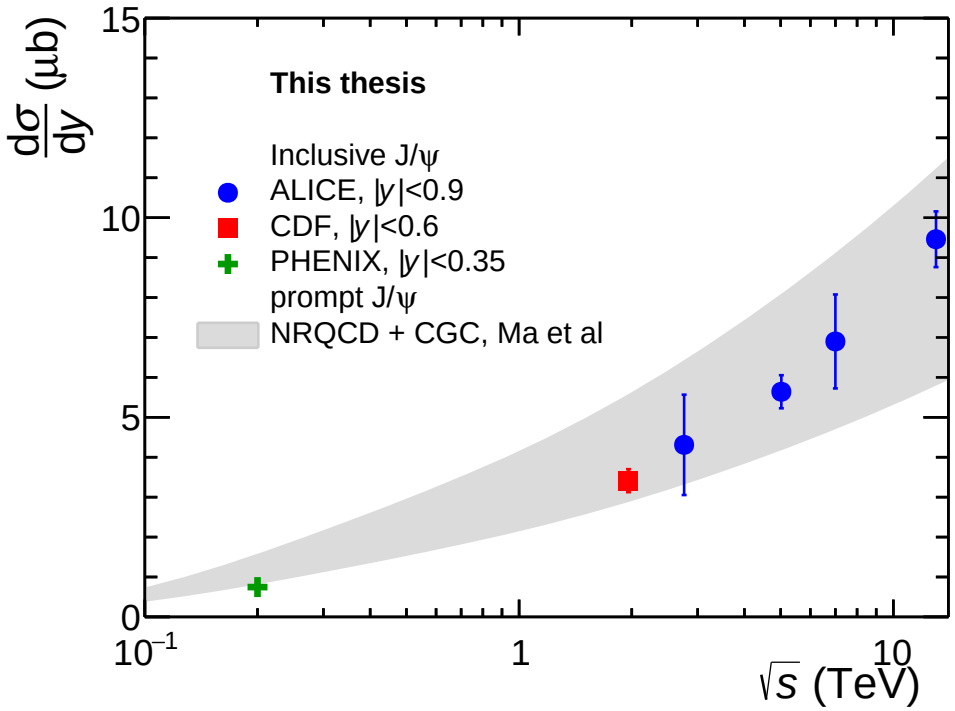

FIGURE 7.1: Energy dependence of the inclusive J/ψ cross section with CGC+NRQCD model calculations from [76]. The result from this analysis is shown together with measurements from PHENIX [77], CDF [78] and ALICE [74, 79, 80].

7.2 p_{T} differential cross section

The p_{T} differential cross section, as described in section 5.7, is determined by equation 5.18. Figure 7.2 shows the differential cross section where the statistical uncertainties are shown as error bars and the systematic uncertainty as boxes. The systematic uncertainty does not include the global uncertainty.

The result is compared to previous ALICE measurements for the inclusive J/ψ cross section at mid-rapidity in figure 7.3. The figure shows the preliminary cross section at $\sqrt{s} = 5$ TeV [74], the published cross section at $\sqrt{s} = 7$ TeV [80] as well as the results from this thesis at $\sqrt{s} = 13$ TeV with scaling factors of 1, 10 and 100, respectively. The statistical uncertainties are shown as error bars and the quadratic sum of the p_{T} correlated and uncorrelated systematic uncertainties excluding global uncertainties are shown as boxes. It is observed that the p_{T} reach for the measured cross section at $\sqrt{s} = 5$ TeV is larger than for the $\sqrt{s} = 7$ TeV measurement. This is due to the large amount of statistics for the $\sqrt{s} = 5$ TeV data set, as can be seen when comparing the luminosities of the two measurements. The systematic uncertainties of the $\sqrt{s} = 5$ TeV and $\sqrt{s} = 13$ TeV

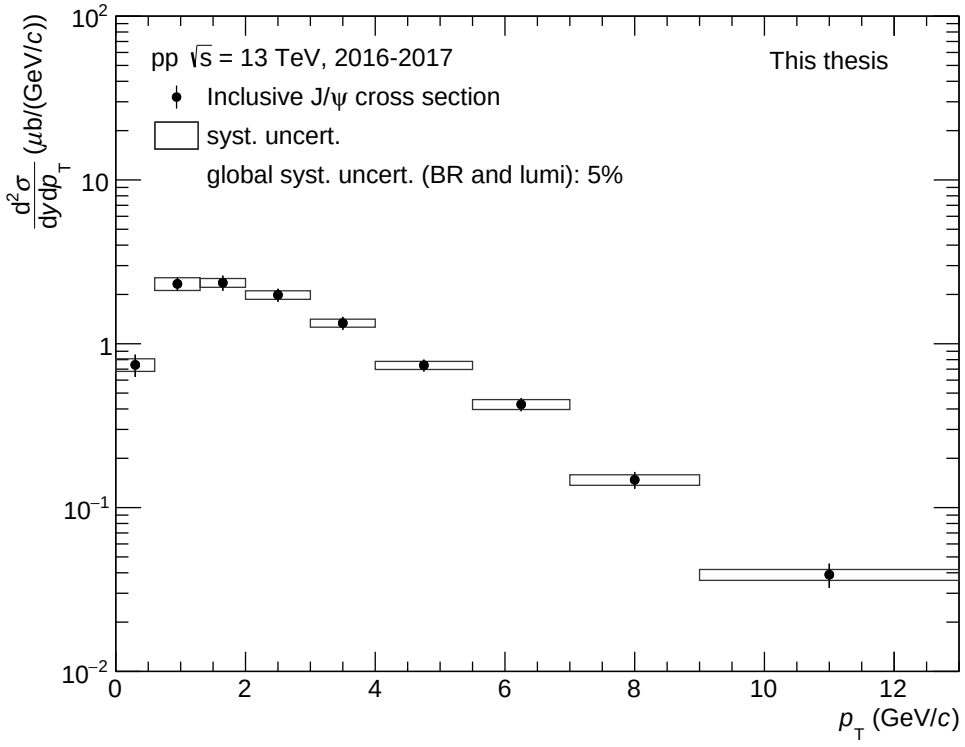

FIGURE 7.2: Inclusive J/ψ cross section at $\sqrt{s} = 13$ TeV with statistical uncertainty shown as vertical lines and the total systematic uncertainty apart from the global contribution shown as boxes.

measurements are comparable, while the systematic uncertainty of the $\sqrt{s} = 7$ TeV measurement is larger.

In figure 7.4 the result is compared to the inclusive J/ψ cross section measured by ALICE through the di-muon channel at forward-rapidity [41]. The mid-rapidity result is shown in blue and the forward-rapidity in black. The statistical uncertainties are shown as error bars and the systematic uncertainties apart from the global uncertainty are shown as boxes. The forward-rapidity measurement has higher statistics and therefore extends to higher p_{T}. The mid-rapidity measurement has slightly higher values for the p_{T} differential measurement than the measurement at forward-rapidity. This is expected, as the cross section measurement has a slight rapidity dependence with a maximum at mid-rapidity.

For this analysis, no p_{T} differential model calculations at mid-rapidity are available. Thus, no model comparisons can be performed for the p_{T} differential results.

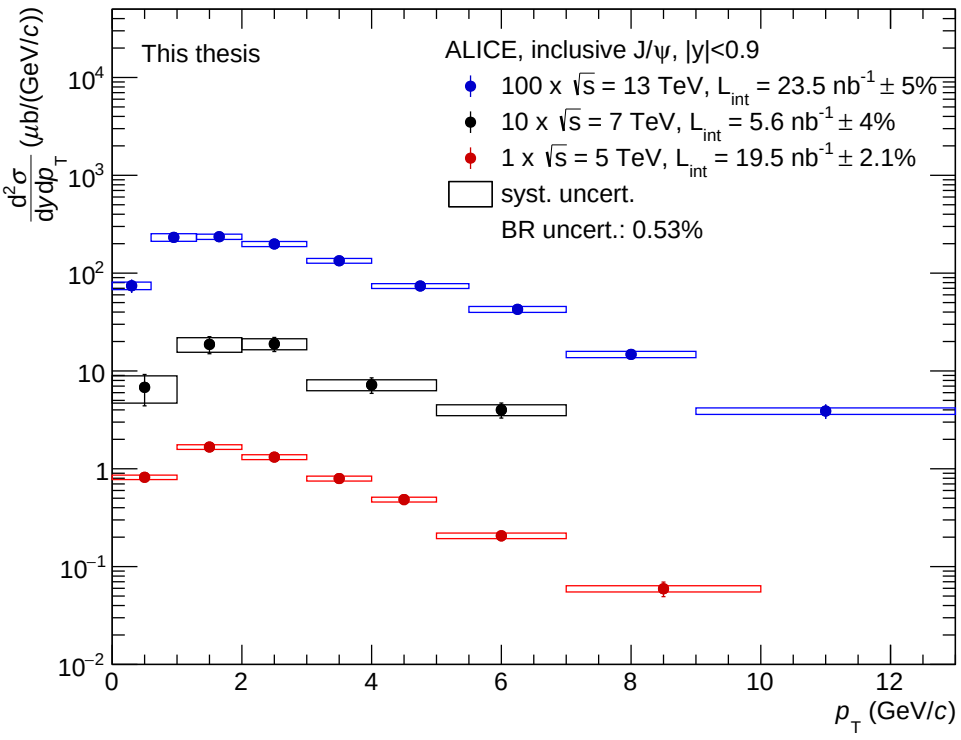

FIGURE 7.3: Inclusive J/ψ cross section measurements at mid-rapidity for $\sqrt{s}$ = 5 TeV [74] in red, $\sqrt{s}$ = 7 TeV [80] in black and $\sqrt{s}$ = 13 TeV in blue, scaled by 1, 10 and 100, respectively. The statistical uncertainties are represented by error bars and the total systematic uncertainties apart from the luminosity are shown as boxes.

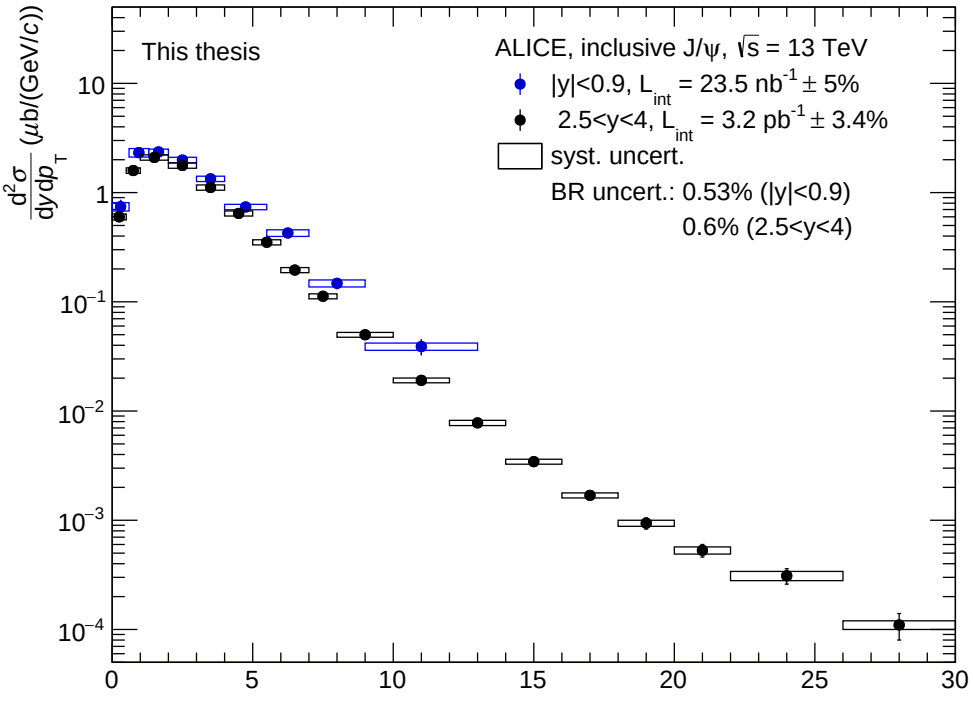

FIGURE 7.4: ALICE measurements of the inclusive J/ψ cross section at $\sqrt{s} = 13$ TeV at forward rapidity and mid-rapidity in black and blue, respectively. The statistical uncertainties are represented by error bars and the total systematic uncertainties apart from the luminosity are shown as boxes.

Chapter 8

Outlook

This analysis was performed on parts of the, as of now, largest data set recorded by ALICE. The pp data set at $\sqrt{s} = 13$ TeV consists of data taken during run 2 from 2015 to 2018. The 2015 data set was looked at briefly for this analysis, but due to the lack of MC productions anchored to half of the data period, as well as quite a large fraction of problematic runs, the data set was not included. The 2018 data set was not finished in time for its inclusion in this thesis. This data set amounts to about the same size as the 2017 data set, and would thus increase the achieved statistics significantly. A natural step when further analyzing the $\sqrt{s} = 13$ TeV data set would be to include pp runs from 2018. However, increasing the amount of statistics for the MB data set will not dramatically increase the p_{T} reach of the measurement. In order to go to higher p_{T}, one would have to use triggered data, e.g. the high multiplicity trigger provided by the V0.

Nevertheless, the data set used in this analysis is very large and was acquired over a long period of time. Analysis of smaller data chunks should therefore be performed in order to investigate possible biases introduced by changes in the data taking conditions.

For this analysis, a post calibration of the TPC energy loss distributions in data was performed only for periods which were missing dedicated TPC splines. A slight dip in the TPC $n\sigma_e$ vs η observed as a general tendency in the 2017 data set. A further investigation of this would be in order, and a possible post calibration of these periods could be considered.

Further, a more thorough check should be performed for the systematic uncertainties. The kinematics of the injected J/ψ mesons in the MC production have been seen to give small uncertainty in previous analyses [74]. Even though such contributions are expected to be small, this should be taken into account in the future. Also, the cut variation method used to determine the systematic uncertainty associated with the PID may be biased by large statistical fluctuations and overestimate the associated systematic uncertainty. Alternatively, the systematic uncertainty can be determined by the use of a single electron method. The method relies on using a clean sample of electrons from photon conversions in data and identified electrons in MC. A single electron cut efficiency can be determined as the ratio between the pure electrons surviving a certain cut variation to the number of electrons passing a reference cut. The obtained efficiencies can then be

propagated through a toy MC in order to determine the impact on the J/ψ cross section. The difference between the obtained acceptance times PID efficiency for data and MC can then be used as a measure for the systematic uncertainty related to the PID. Such a method was performed in the cross section analysis at $\sqrt{s} = 5$ TeV [74] and was found to yield smaller systematic uncertainties than the cut variation method.

For this analysis, no model comparison for the p_{T} differential cross section is available. With available model calculations, the *ad hoc* method combining NRQCD models with FONLL would make comparisons to the cross section possible. This is done for the forward rapidity measurement at $\sqrt{s} = 13$ TeV, indicating a good agreement between the data and model predictions [41]. Accurate comparisons to model predictions require measurements of the prompt/non-prompt J/ψ fraction. An analysis determining this fraction for the data set analyzed in this thesis is ongoing and will be important for further model comparisons. The polarization of the J/ψ at mid-rapidity is not yet determined. Hence, further polarization measurements are important for further model constraints.

Appendix A

Number of runs and events

$\mathrm{TPC}_{\mathrm{acceptance}}$		N_{runs}	$N^{\mathrm{sel}}_{\mathrm{V0AND}}$	f_{z}	$N^{\mathrm{corr}}_{\mathrm{V0AND}}$		$N_{\mathrm{evts.,\ MC}}$
	2016 data					*2016 data anchored MC, J/ψ injected*	
Complete	LHC16d	10	1.60×10^7			LHC17h2a	5.18×10^5
Incomplete		7	2.08×10^7				5.56×10^5
Total		17	3.69×10^7	0.964	3.56×10^7		1.07×10^6
Complete	LHC16e	11	5.22×10^7			LHC17h2b	1.69×10^6
Incomplete		2	1.20×10^7				2.90×10^5
Total		13	6.42×10^7	0.971	6.23×10^7		1.98×10^6
Complete	LHC16f	0	–			LHC17h2c	–
Incomplete		6	6.63×10^6				2.32×10^5
Total		6	6.63×10^6	0.970	6.43×10^6		2.32×10^5
Complete	LHC16g	18	2.88×10^7			LHC17h2d	1.03×10^6
Incomplete		0	–				–
Total		18	2.88×10^7	0.966	2.79×10^7		1.03×10^6
Complete	LHC16h	68	7.94×10^7			LHC17h2e	2.89×10^6
Incomplete		1	3.05×10^6				1.09×10^5
Total		69	8.25×10^7	0.976	8.05×10^7		3.00×10^6
Complete	LHC16i	14	3.18×10^7			LHC17h2f	1.18×10^6
Incomplete		1	9.67×10^5				3.49×10^4
Total		15	3.28×10^7	0.975	3.19×10^7		1.22×10^6
Complete	LHC16j	44	5.84×10^7			LHC17h2g	2.02×10^6
Incomplete		1	3.44×10^6				9.87×10^4
Total		45	6.18×10^7	0.980	6.06×10^7		2.12×10^6
Complete	LHC16k	171	1.34×10^8			LHC17h2h2	4.89×10^6
Incomplete		7	1.06×10^7				3.90×10^5
Total		178	1.44×10^8	0.978	1.41×10^8		5.28×10^6
Complete	LHC16l	58	3.10×10^7			LHC17h2i2	1.12×10^6
Incomplete		2	1.24×10^6				4.54×10^4
Total		60	3.22×10^7	0.970	3.13×10^7		1.16×10^6
Complete	LHC16o	74	3.50×10^7			LHC17h2j	1.22×10^6
Incomplete		28	1.85×10^7				6.09×10^5
Total		102	5.35×10^7	0.972	5.20×10^7		1.83×10^6
Complete	LHC16p	42	2.16×10^7			LHC17h2k	7.57×10^5
Incomplete		0	–				–
Total		42	2.16×10^7	0.967	2.09×10^7		7.57×10^5
Complete	LHC16[d-p]	510	4.88×10^8			LHC17h2[a-k]	1.73×10^7
Incomplete		55	7.73×10^7				2.37×10^6
Total		565	5.65×10^8		5.51×10^8		1.97×10^7

TABLE A.1: Number of runs and selected events for the selection of good runs with complete, reduced, and including reduced TPC acceptance for data and MC periods used in this analysis.

$\mathrm{TPC}_{\mathrm{acceptance}}$		N_{runs}	$N^{\mathrm{sel}}_{\mathrm{V0AND}}$	f_{z}	$N^{\mathrm{corr}}_{\mathrm{V0AND}}$		$N_{\mathrm{evts.,\ MC}}$
	2017 data					*2017 data anchored MC, J/ψ injected*	
Complete	LHC17c	5	9.50×10^6			LHC18b1a [c]	9.05×10^5
Incomplete		0	–				–
Total		5	9.50×10^6	0.970	9.21×10^6		9.05×10^5
Complete	LHC17e	5	1.03×10^7			LHC18b1a [e]	1.07×10^6
Incomplete		0	–				–
Total		5	1.03×10^7	0.974	1.00×10^7		1.07×10^6
Complete	LHC17f	5	9.91×10^6			LHC18b1a [f]	1.07×10^6
Incomplete		0	–				–
Total		5	9.91×10^6	0.964	9.56×10^6		1.07×10^6
Complete	LHC17g	31	1.10×10^8			LHC18b1a [g]	1.06×10^7
Incomplete		0	–				–
Total		31	1.10×10^8	0.971	1.07×10^8		1.06×10^7
Complete	LHC17h	93	1.34×10^8			LHC18b1a [h]	1.28×10^7
Incomplete		6	3.29×10^6				3.64×10^5
Total		99	1.38×10^8	0.977	1.34×10^8		1.32×10^7
Complete	LHC17i	61	5.93×10^7			LHC18b1a [i]	5.16×10^6
Incomplete		3	1.03×10^6				9.63×10^4
Total		64	6.03×10^7	0.971	5.86×10^7		5.26×10^6
Complete	LHC17j	10	4.09×10^7			LHC18b1a [j]	3.65×10^6
Incomplete		0	–				–
Total		10	4.09×10^7	0.979	4.00×10^7		3.65×10^6
Complete	LHC17k	124	1.20×10^8			LHC18b1a [k]	9.87×10^6
Incomplete		7	2.75×10^6				2.27×10^5
Total		131	1.23×10^8	0.977	1.20×10^8		1.01×10^7
Complete	LHC17l	129	7.50×10^7			LHC18b1a [l]	7.34×10^6
Incomplete		4	1.66×10^6				1.61×10^5
Total		133	7.66×10^7	0.980	7.51×10^7		7.50×10^6
Complete	LHC17m	109	1.04×10^8			LHC18b1a [m]	9.69×10^6
Incomplete		0	–				–
Total		109	1.04×10^8	0.977	1.02×10^8		9.69×10^6
Complete	LHC17o	155	1.12×10^8			LHC18b1a [o]	1.06×10^7
Incomplete		19	8.53×10^6				7.79×10^5
Total		174	1.21×10^8	0.973	1.18×10^8		1.14×10^7
Complete	LHC17r	30	2.78×10^7			LHC18b1a [r]	2.59×10^6
Incomplete		0	–				–
Total		30	2.78×10^7	0.971	2.70×10^7		2.59×10^6
Complete	LHC17[c-r]	757	8.14×10^8			LHC18b1a[c-r]	7.54×10^7
Incomplete		39	1.73×10^7				1.63×10^6
Total		796	8.31×10^8		8.10×10^8		7.70×10^7

TABLE A.2: Number of runs and physics and trigger selected events for the selection of good runs with complete, reduced, and including reduced TPC acceptance for data and MC periods used in this analysis.

Appendix B

Additional Plots

B.1 Runwise QA of event selection

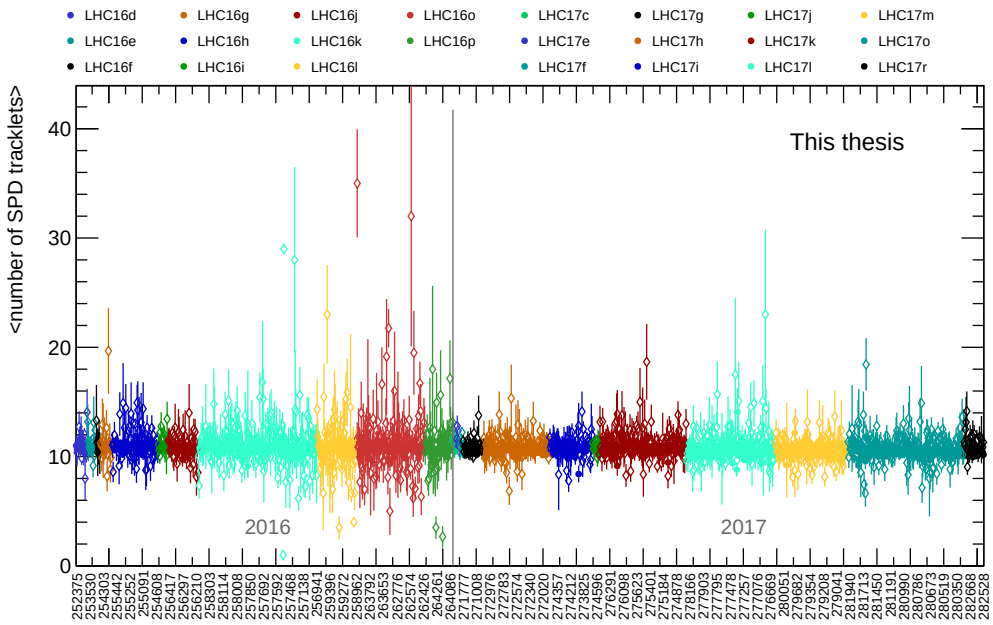

FIGURE B.1: Average number of SPD tracklets for accepted events per run for MB and corresponding MC events. The labels along the x-axis show the run number of every 20th run.

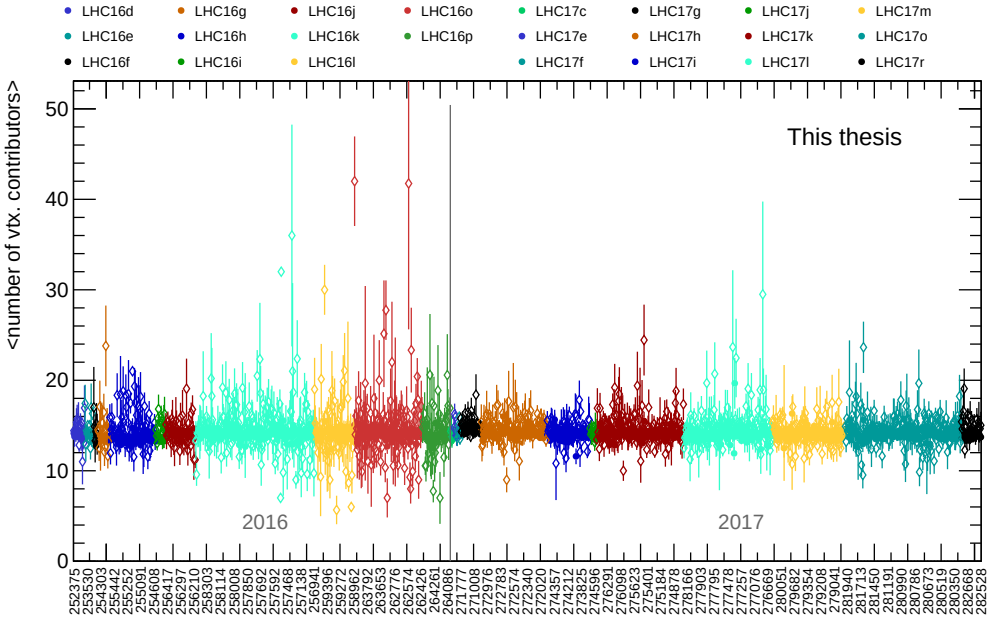

FIGURE B.2: Average number of vertex contributors for accepted events per run for MB and corresponding MC events. The labels along the x-axis show the run number of every 20th run.

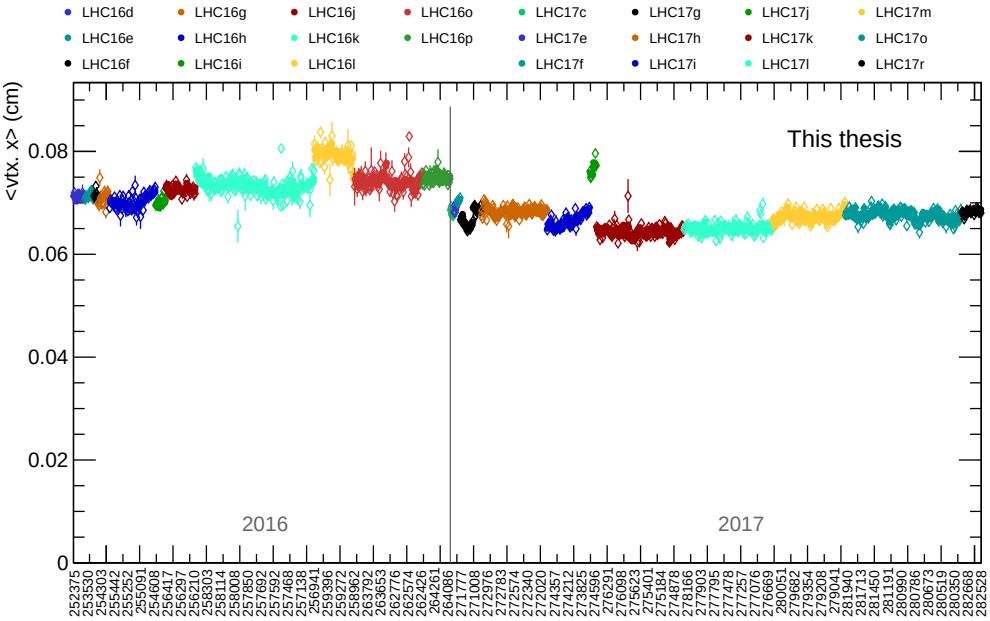

FIGURE B.3: Average vertex x position for accepted events per run for MB and corresponding MC events. The labels along the x-axis show the run number of every 20th run.

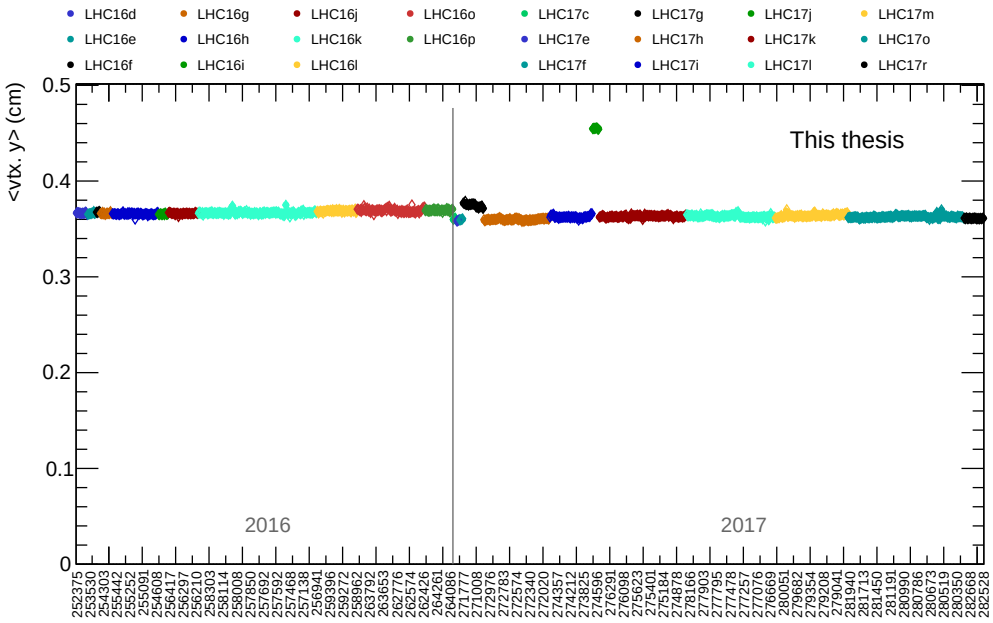

FIGURE B.4: Average vertex y position for accepted events per run for MB and corresponding MC events. The labels along the x-axis show the run number of every 20th run.

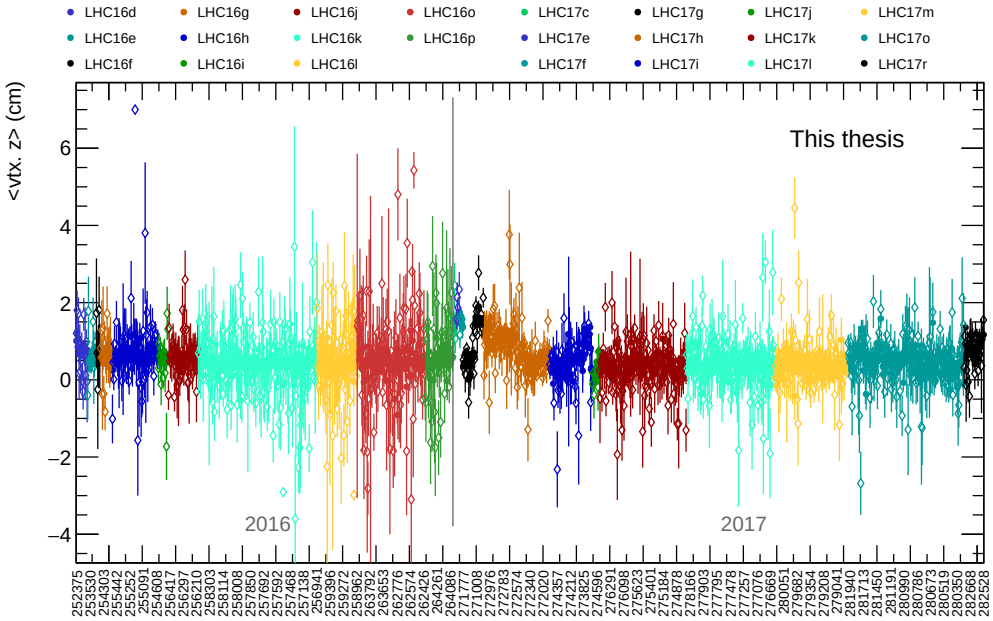

FIGURE B.5: Average vertex z position for accepted events per run for MB and corresponding MC events. The labels along the x-axis show the run number of every 20th run.

B.2 Runwise QA of track selection

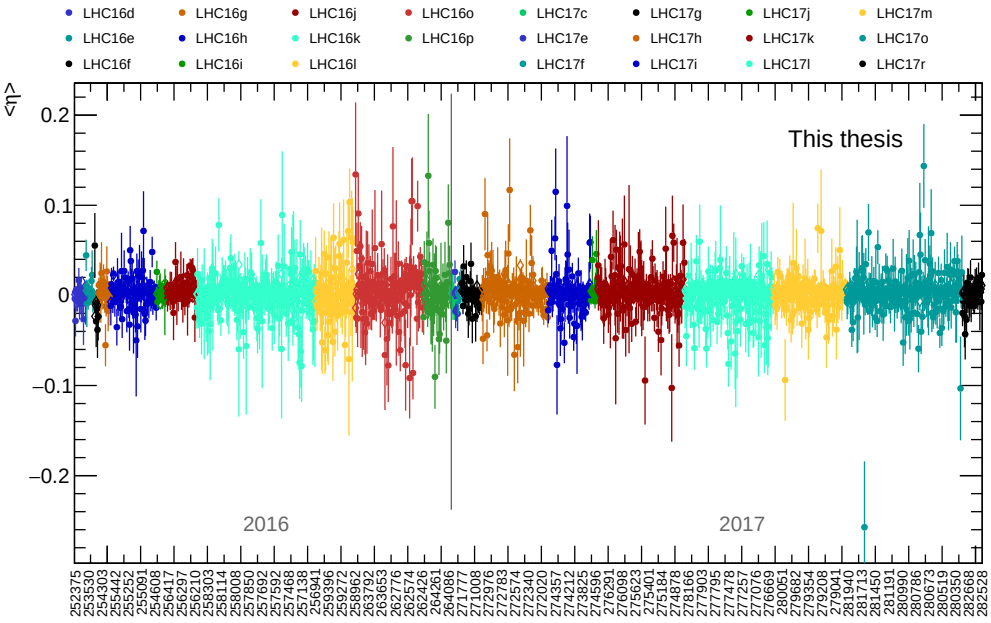

FIGURE B.6: Average η for selected electron tracks per run for MB and corresponding MC events. The labels along the x-axis show the run number of every 20th run.

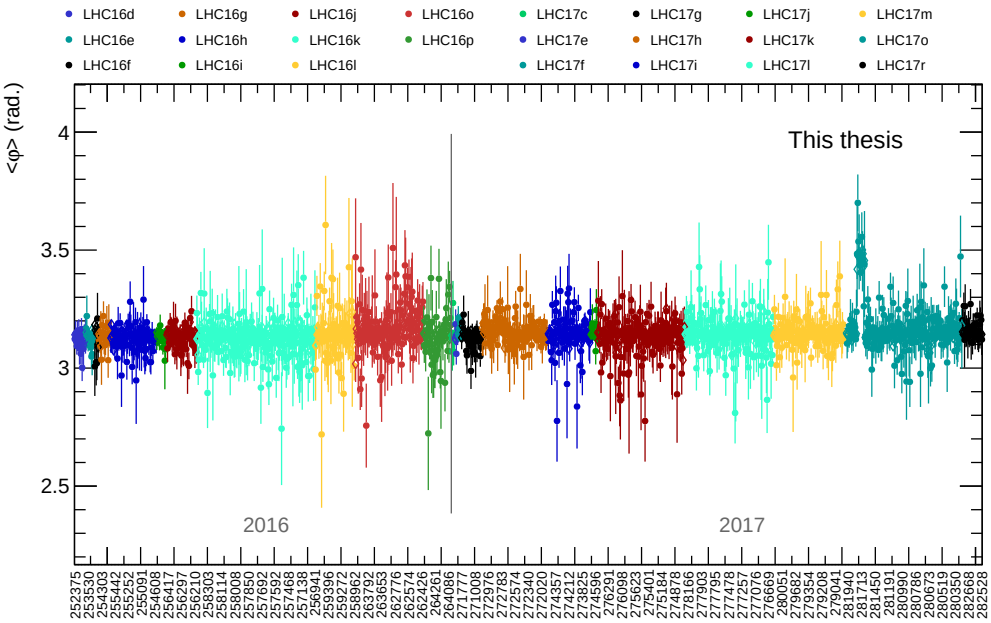

FIGURE B.7: Average φ for selected electron tracks per run for MB and corresponding MC events. The labels along the x-axis show the run number of every 20th run.

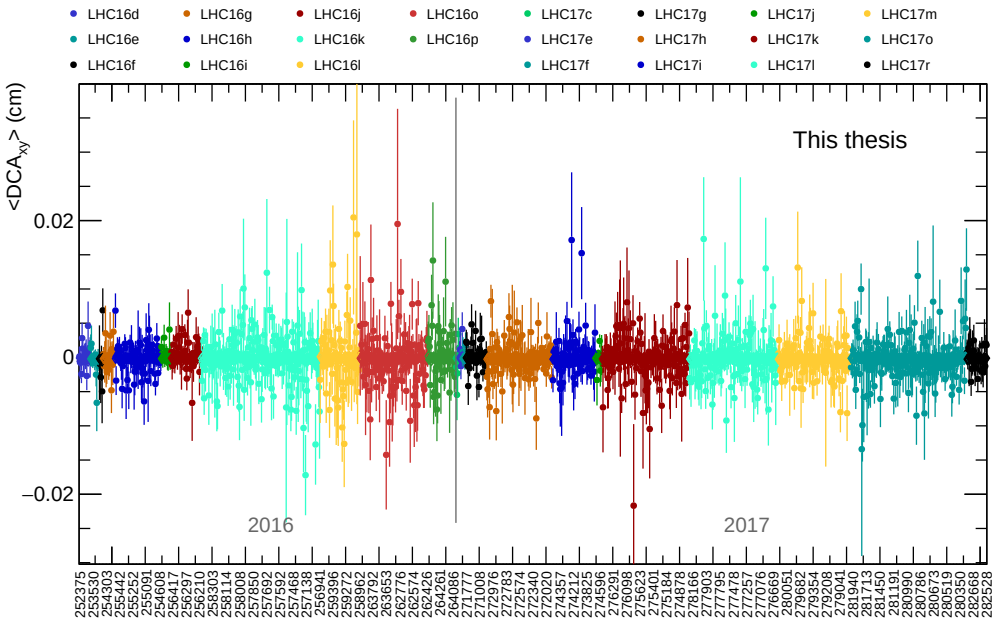

FIGURE B.8: Average DCA in x-y plane for selected electron tracks per run for MB and corresponding MC events. The labels along the x-axis show the run number of every 20th run.

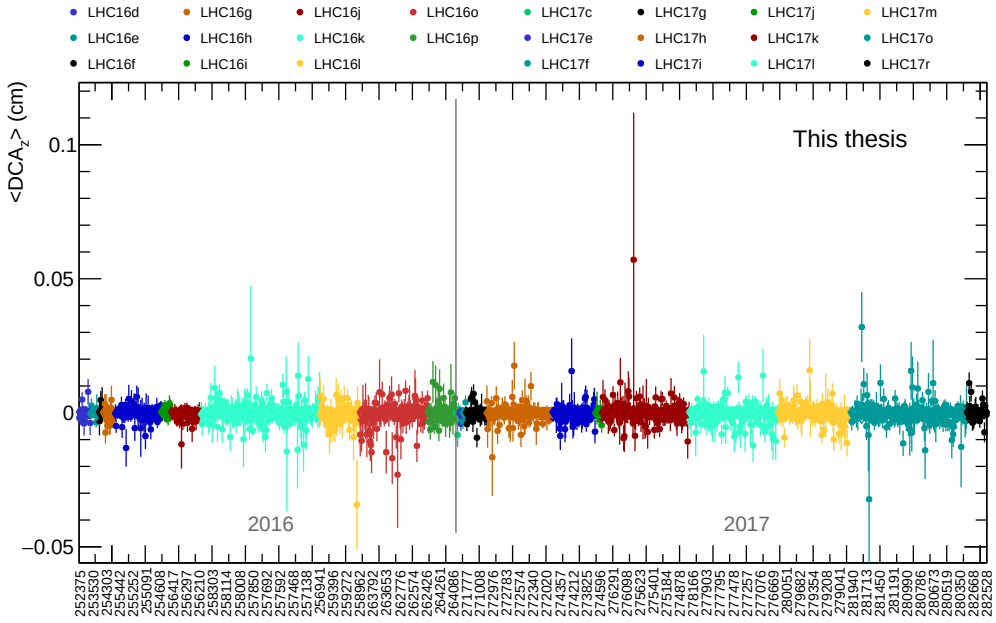

FIGURE B.9: Average DCA in z for selected electron tracks per run for MB and corresponding MC events. The labels along the x-axis show the run number of every 20th run.

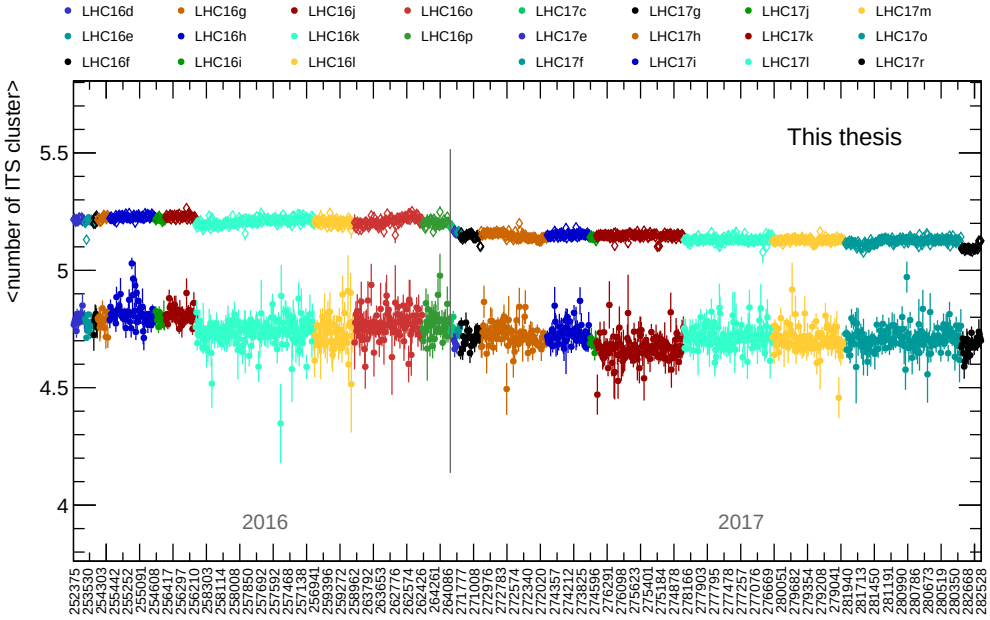

FIGURE B.10: Average number of ITS clusters for selected electron tracks per run for MB and corresponding MC events. Due to the injected J/ψ in the MC sample hard primary electrons dominate the electron sample creating more ITS clusters, thus the average cluster number is higher for the MC sample than the data sample. The labels along the x-axis show the run number of every 20th run.

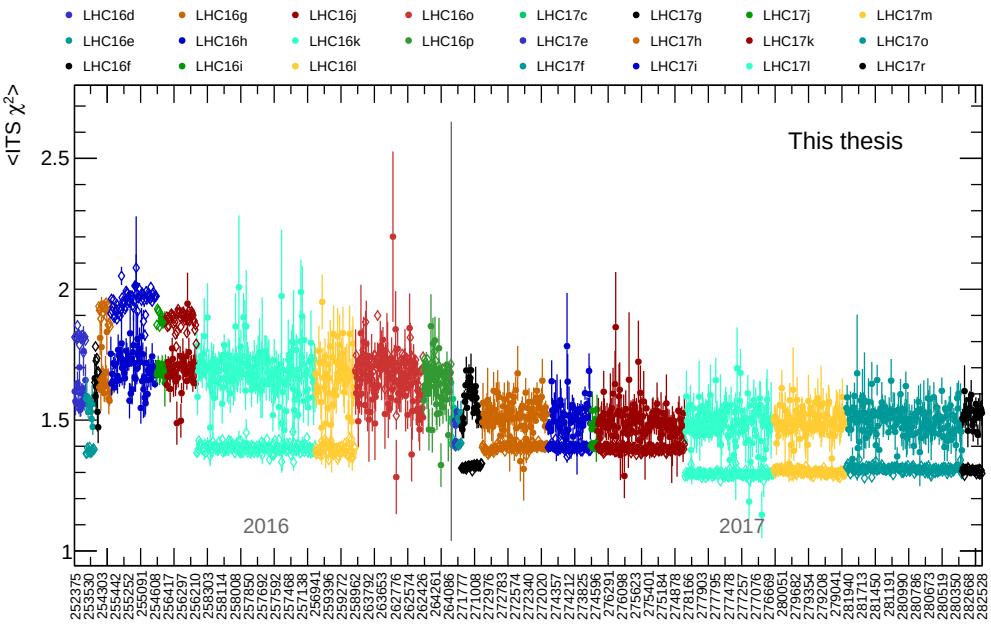

FIGURE B.11: Average ITS χ^2 for selected electron tracks per run for MB and corresponding MC events. The labels along the x-axis show the run number of every 20th run.

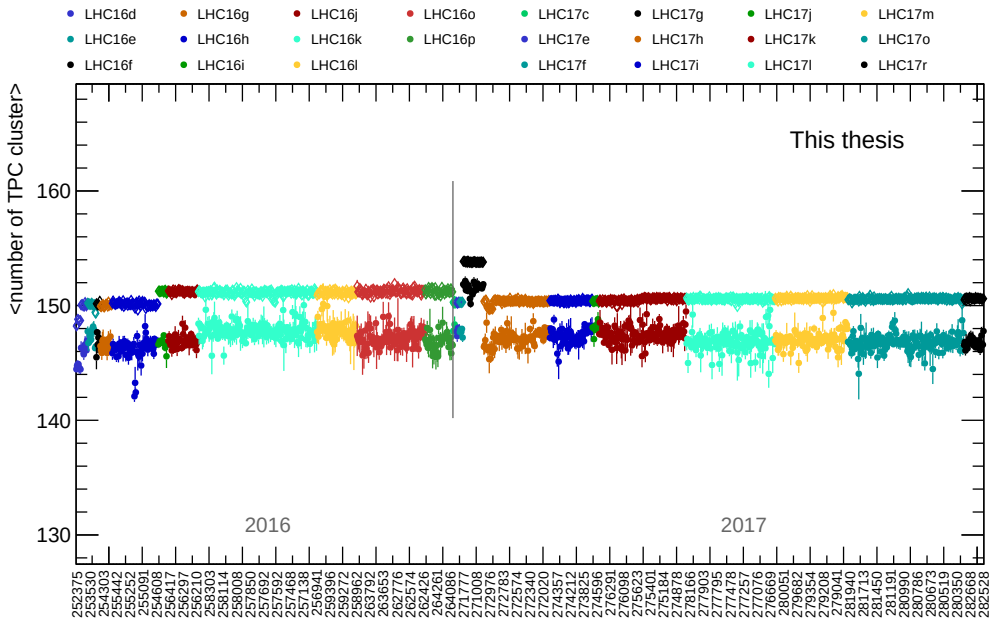

FIGURE B.12: Average number of TPC clusters for selected electron tracks per run for MB and corresponding MC events. Out of bunch pileup tracks in the TPC slightly reduce the cluster charges such that some clusters are below the measured threshold, thus the average number of clusters in the data sample is lower than that of the MC sample. The labels along the x-axis show the run number of every 20th run.

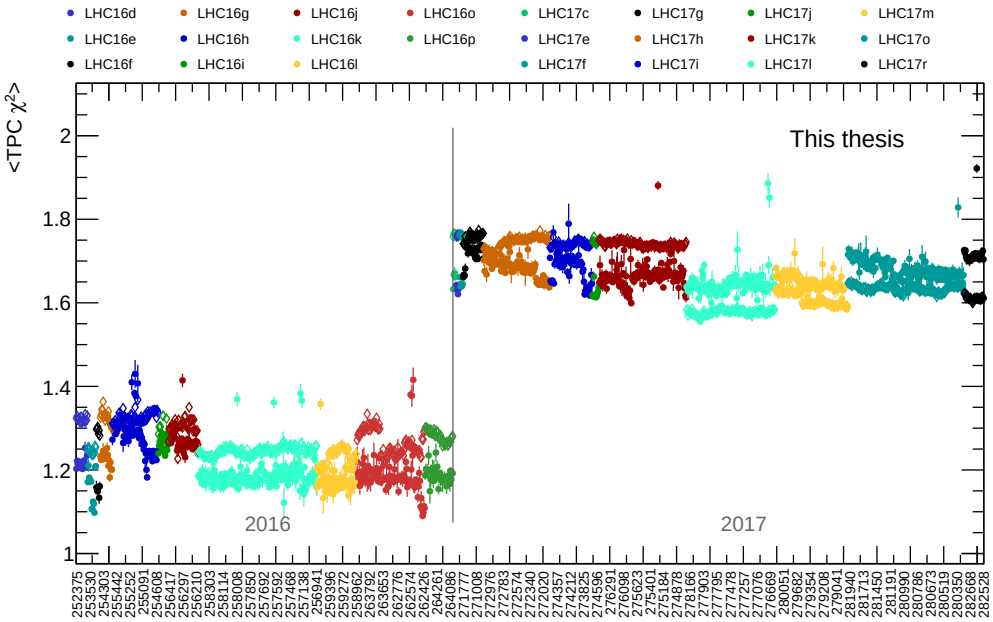

FIGURE B.13: Average TPC χ^2 for selected electron tracks per run for MB and corresponding MC events. The labels along the x-axis show the run number of every 20th run.

B.3 Z-vertex distribution

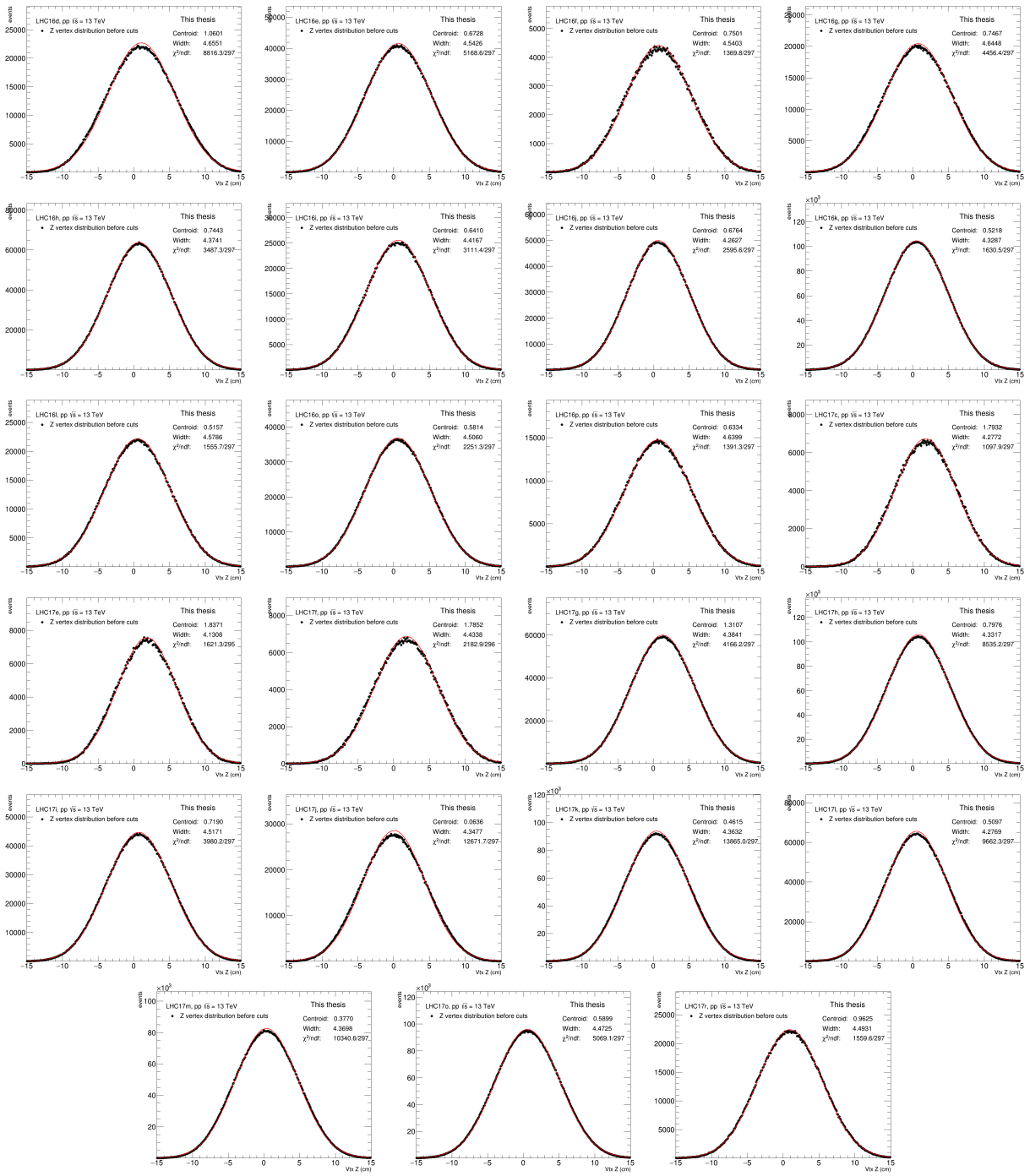

FIGURE B.14: Z-vertex distribution for periods LHC16d-LHC17r, with Gaussian fit in red.

B.4 Electron selection plots

B.4.1 TPC $n\sigma_e$ vs η

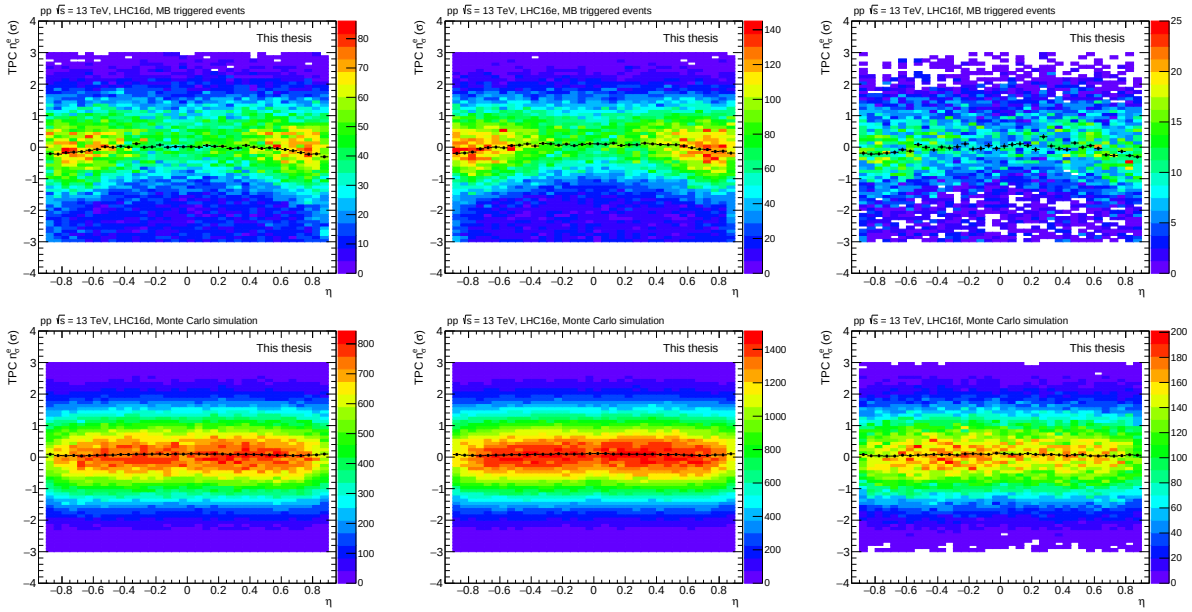

FIGURE B.15: TPC $n\sigma_e$ vs η for period LHC16d (left), LHC16e (middle) and LHC16f (right) with data and MC in the top and bottom row, respectively.

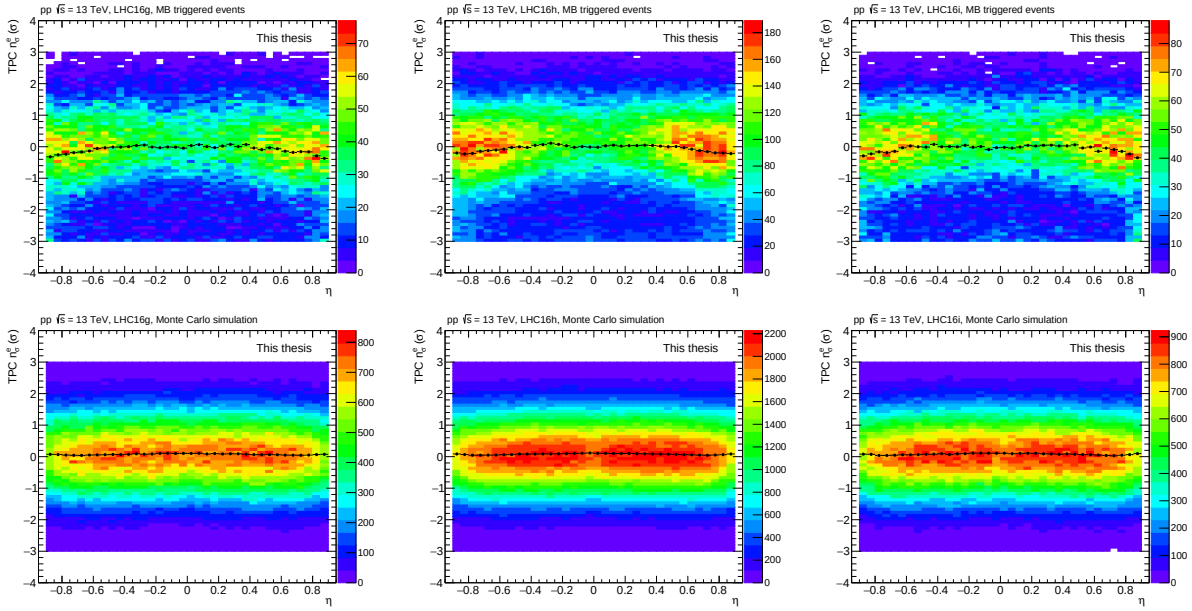

FIGURE B.16: TPC $n\sigma_e$ vs η for period LHC16g (left), LHC16h (middle) and LHC16i (right) with data and MC in the top and bottom row, respectively.

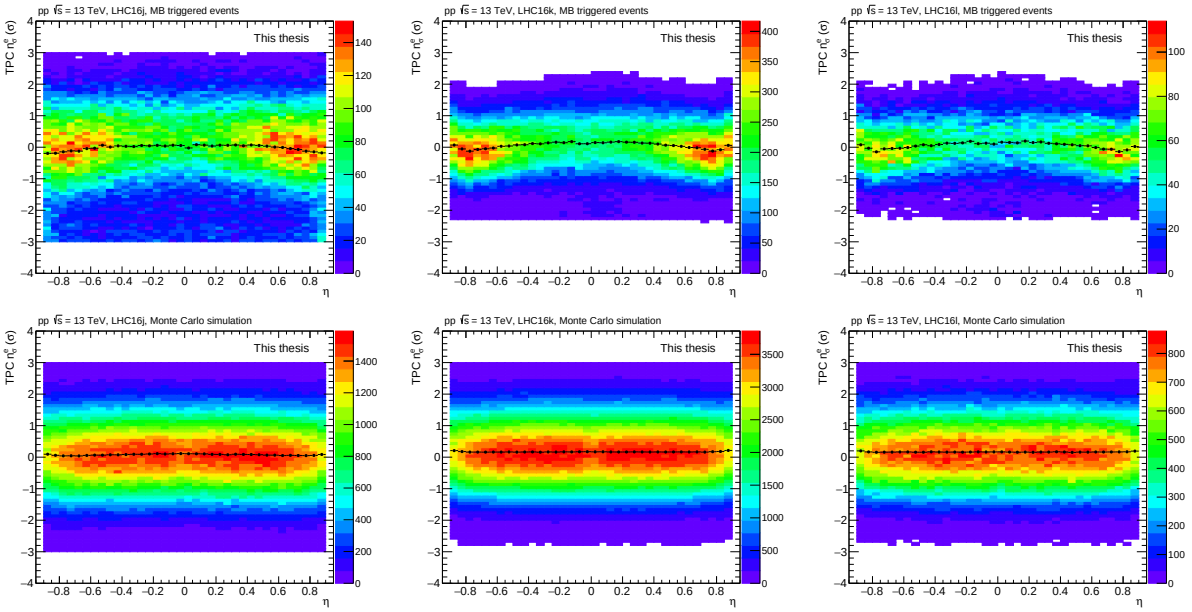

FIGURE B.17: TPC $n\sigma_e$ vs η for period LHC16j (left), LHC16k (middle) and LHC16l (right) with data and MC in the top and bottom row, respectively.

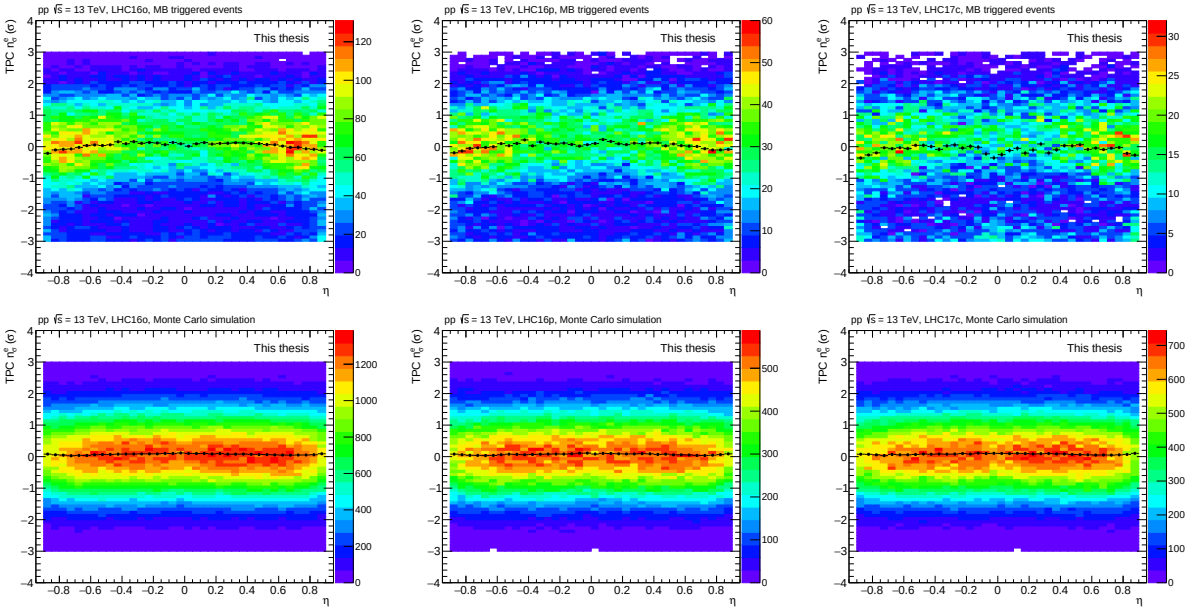

FIGURE B.18: TPC $n\sigma_e$ vs η for period LHC16o (left), LHC16p (middle) and LHC17c (right) with data and MC in the top and bottom row, respectively.

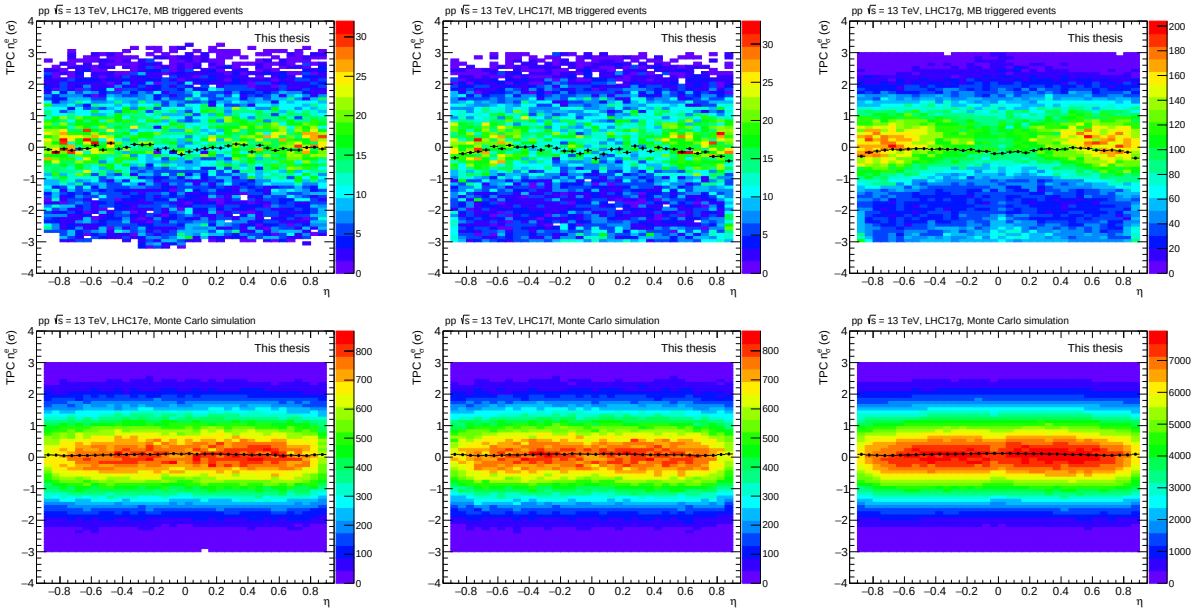

FIGURE B.19: TPC $n\sigma_e$ vs η for period LHC17e (left), LHC17f (middle) and LHC17g (right) with data and MC in the top and bottom row, respectively.

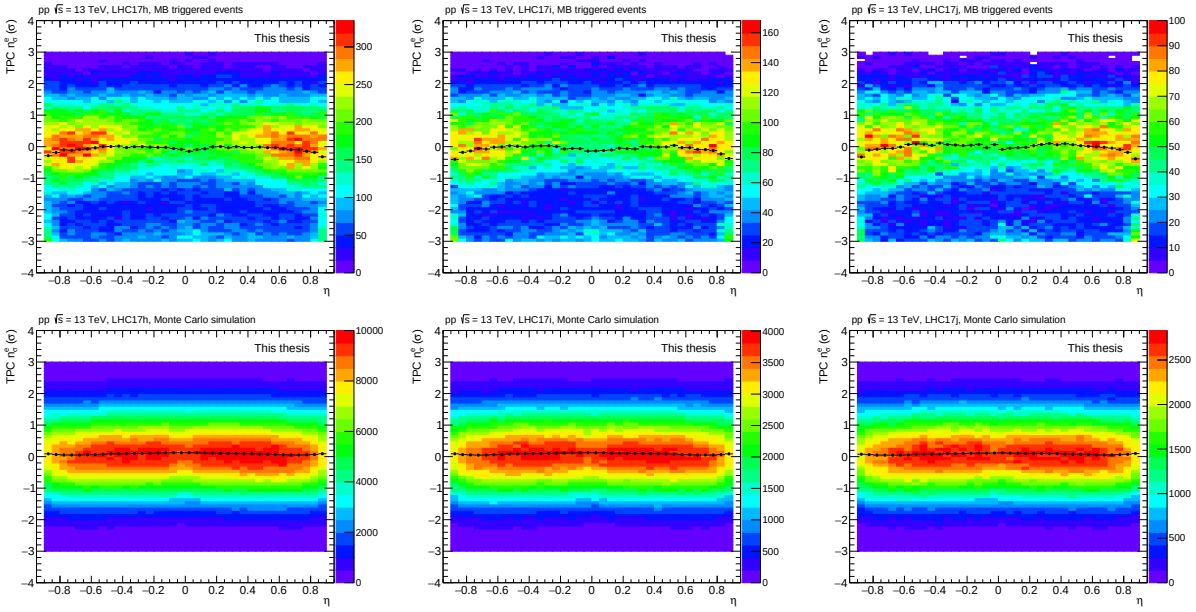

FIGURE B.20: TPC $n\sigma_e$ vs η for period LHC17h (left), LHC17i (middle) and LHC17j (right) with data and MC in the top and bottom row, respectively.

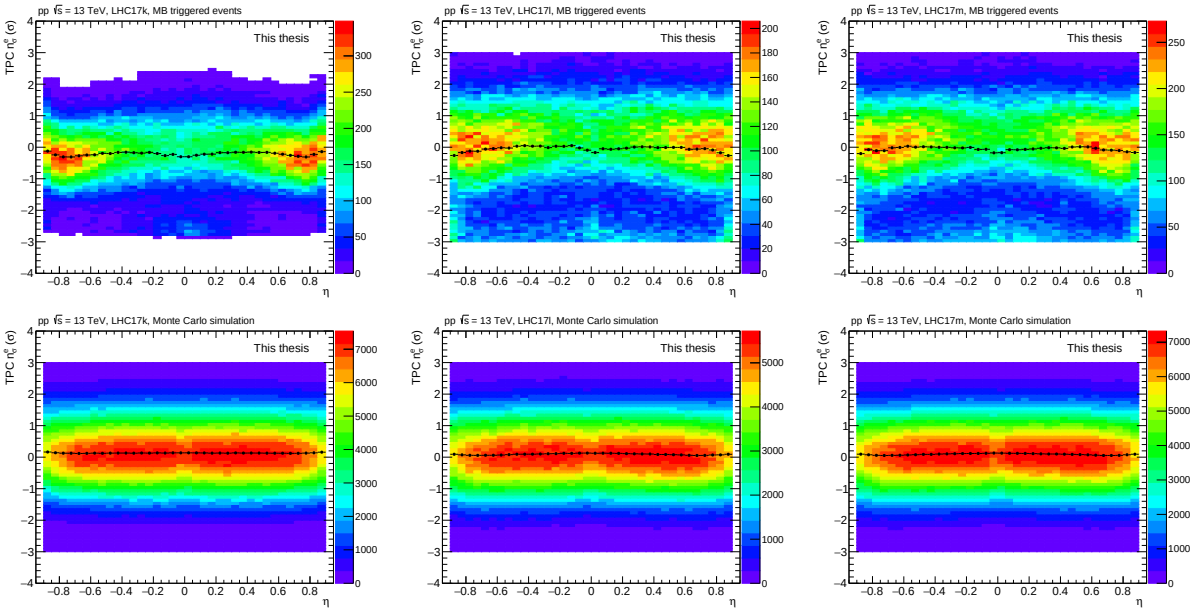

FIGURE B.21: TPC $n\sigma_e$ vs η for period LHC17k (left), LHC17l (middle) and LHC17m (right) with data and MC in the top and bottom row, respectively.

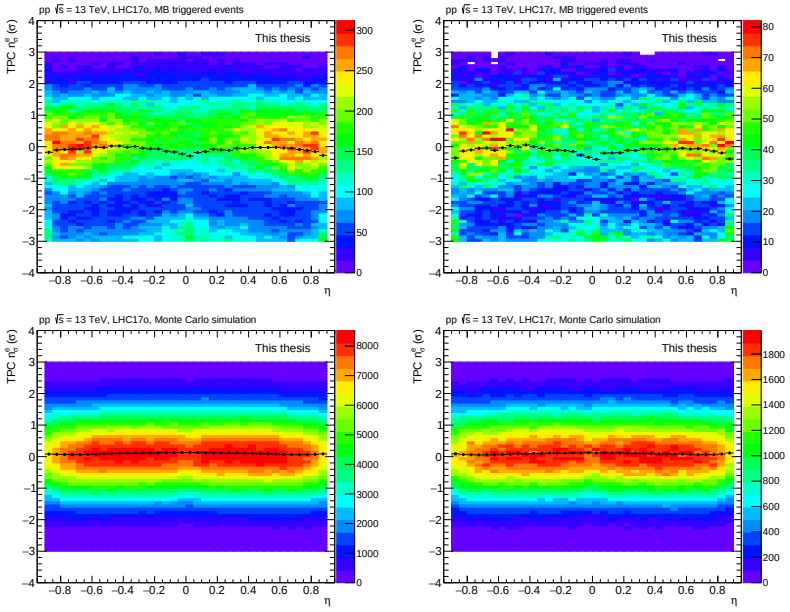

FIGURE B.22: TPC $n\sigma_e$ vs η for period LHC17o (left) and LHC17r (right) with data and MC in the top and bottom row, respectively.

B.4.2 TPC $n\sigma_e$ vs η ratio between MC and data

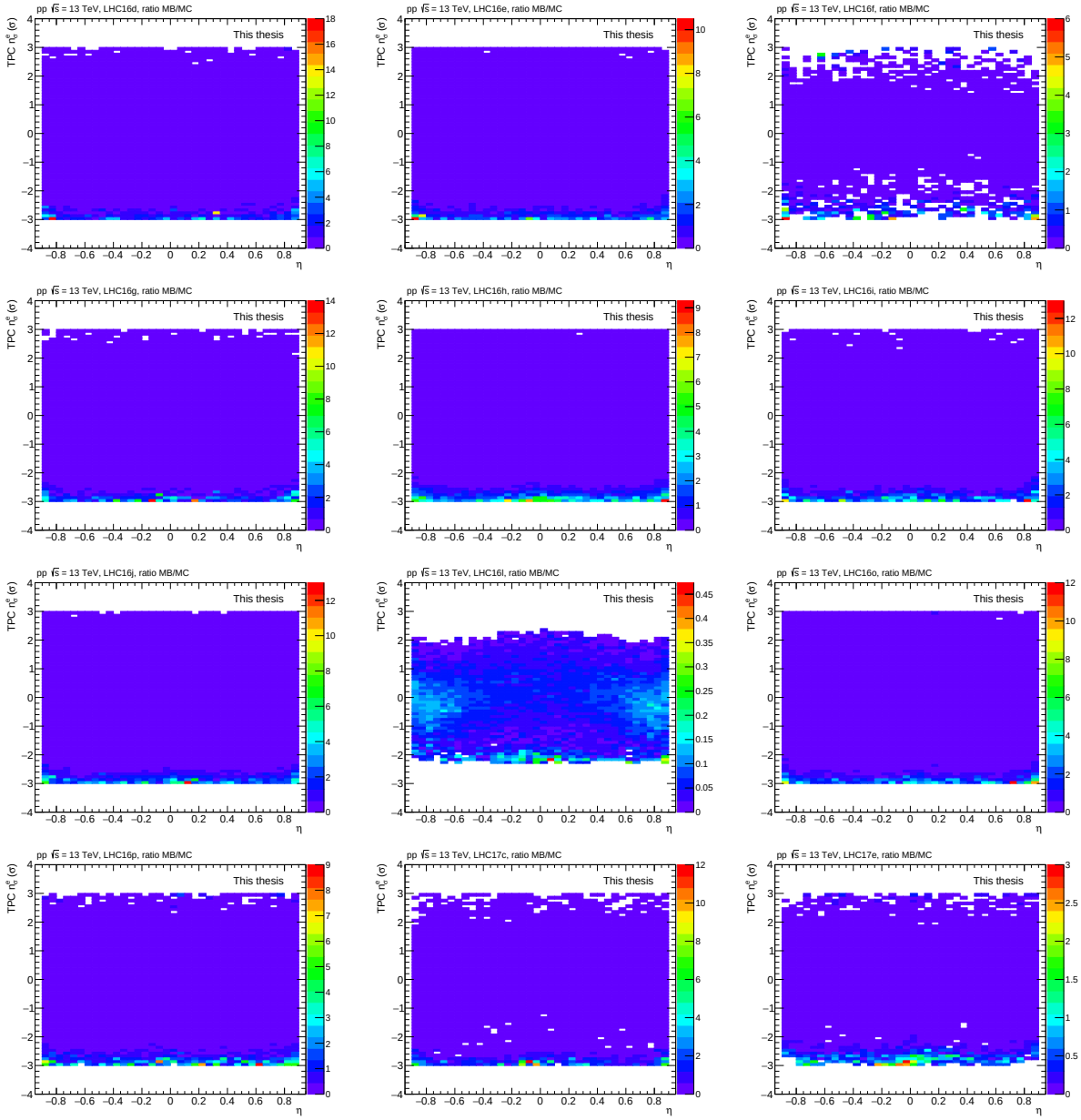

FIGURE B.23: Ratio data to MC of TPC $n\sigma_e$ vs η for periods LHC16d-p and LHC17c-e.

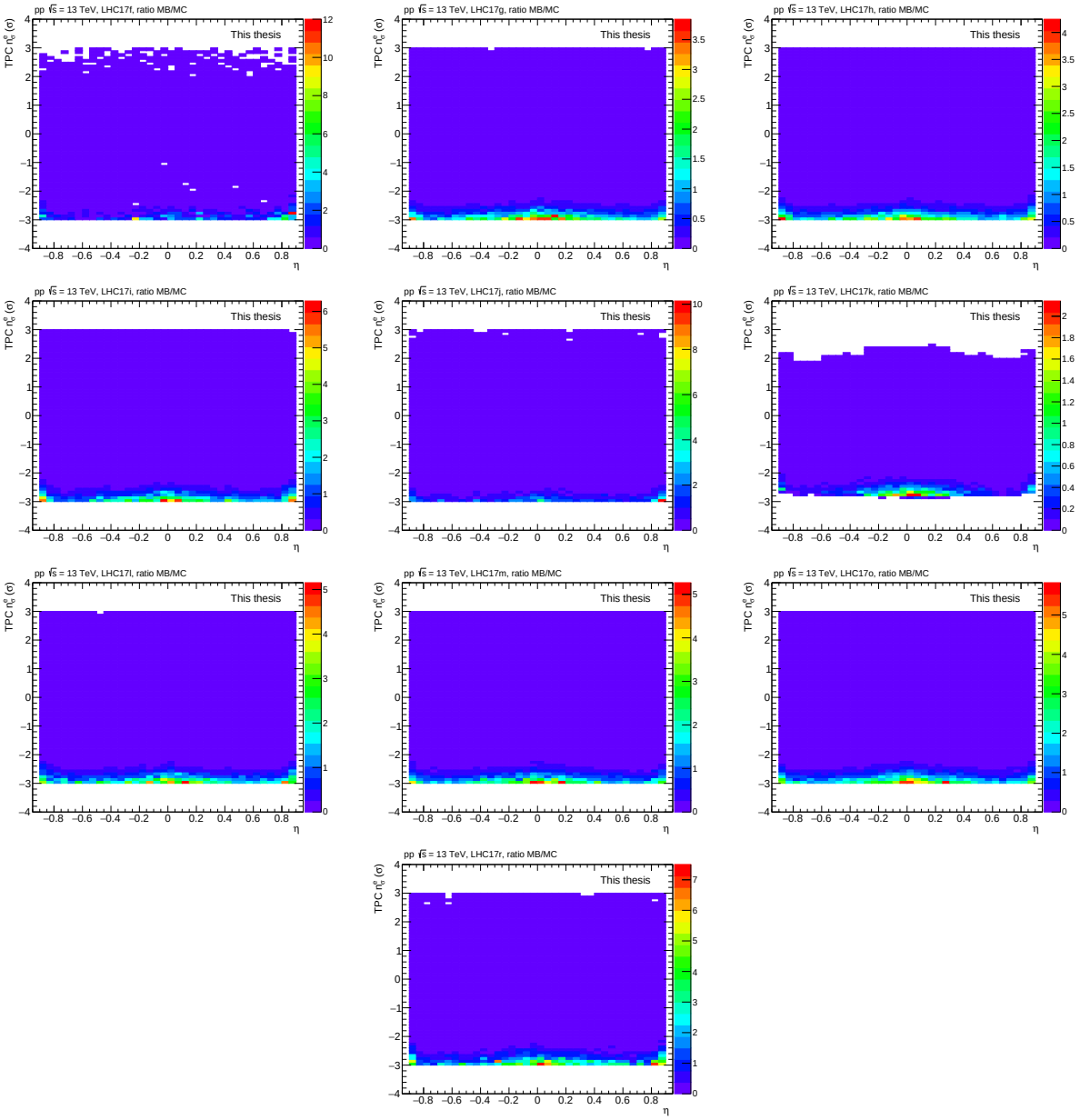

FIGURE B.24: Ratio data to MC of TPC $n\sigma_e$ vs η for periods LHC17f-r.

B.4.3 TPC $n\sigma_e$ vs momentum ratio between MC and data

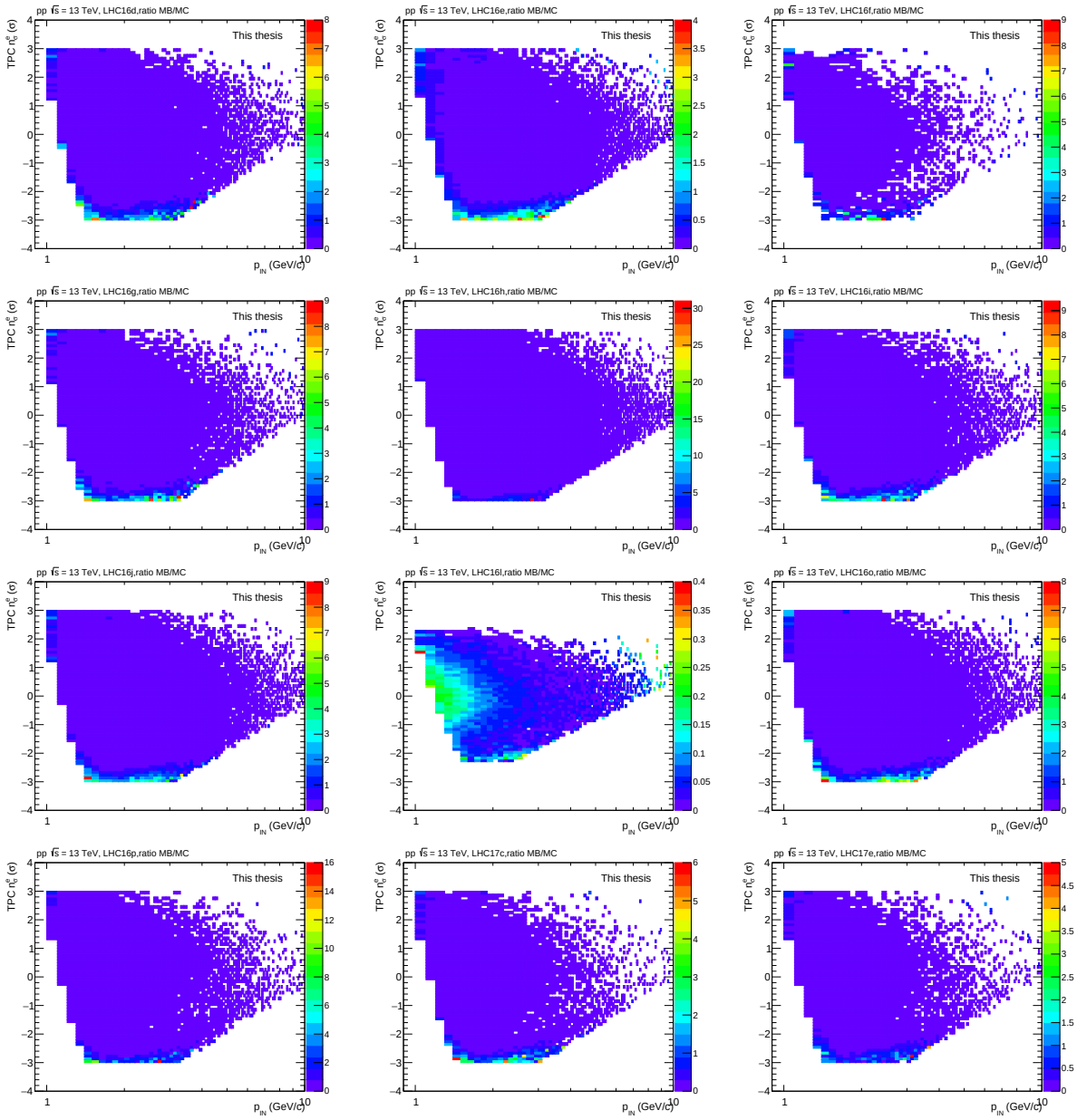

FIGURE B.25: Ratio data to MC of TPC $n\sigma_e$ vs momentum as reconstructed by the TPC for periods LHC16d-i and LHC17c-e.

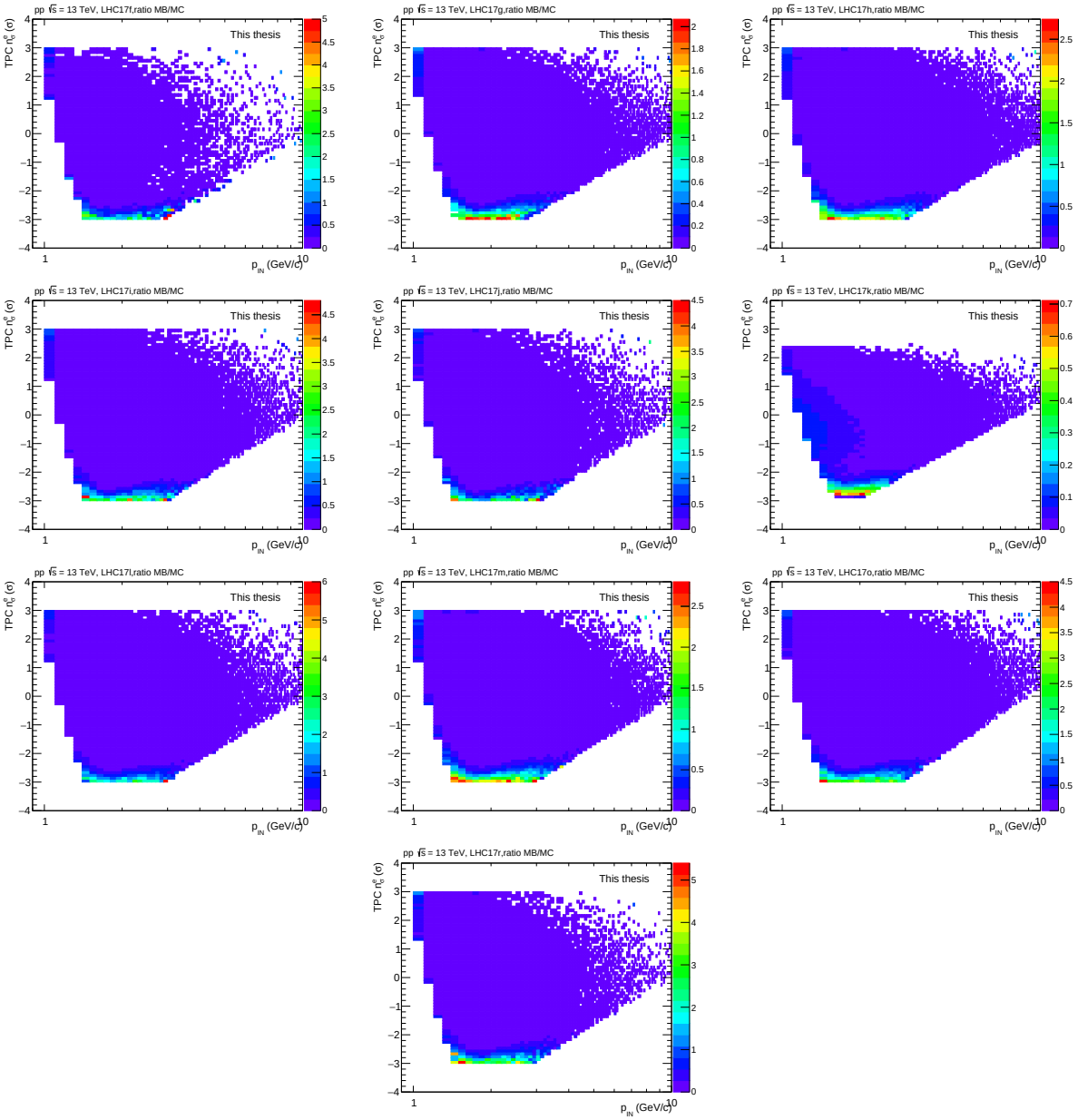

FIGURE B.26: Ratio data to MC of TPC $n\sigma_e$ vs momentum as reconstructed by the TPC for periods LHC17f-r.

B.4.4 TPC $n\sigma_e$ vs momentum

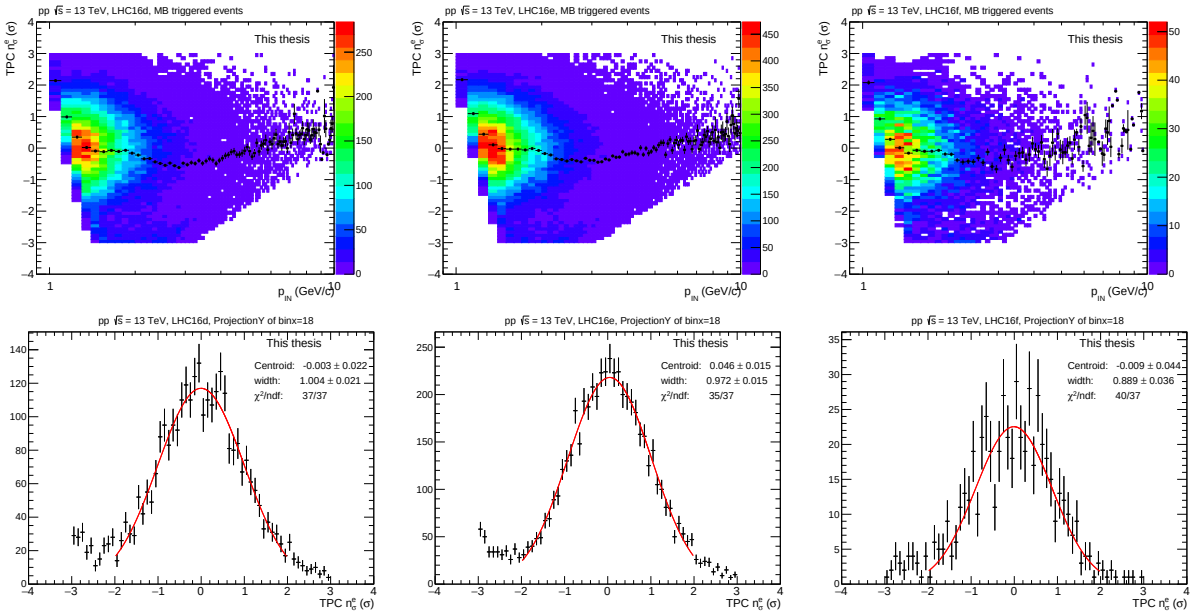

FIGURE B.27: Top: TPC $n\sigma_e$ vs momentum for period LHC16d (left), LHC16e (middle) and LHC16f (right). Bottom: Distribution of selected electron candidates as a function of $n\sigma_e$ in the momentum interval 1.7-1.8 GeV/c fitted with a gaus function for the same periods.

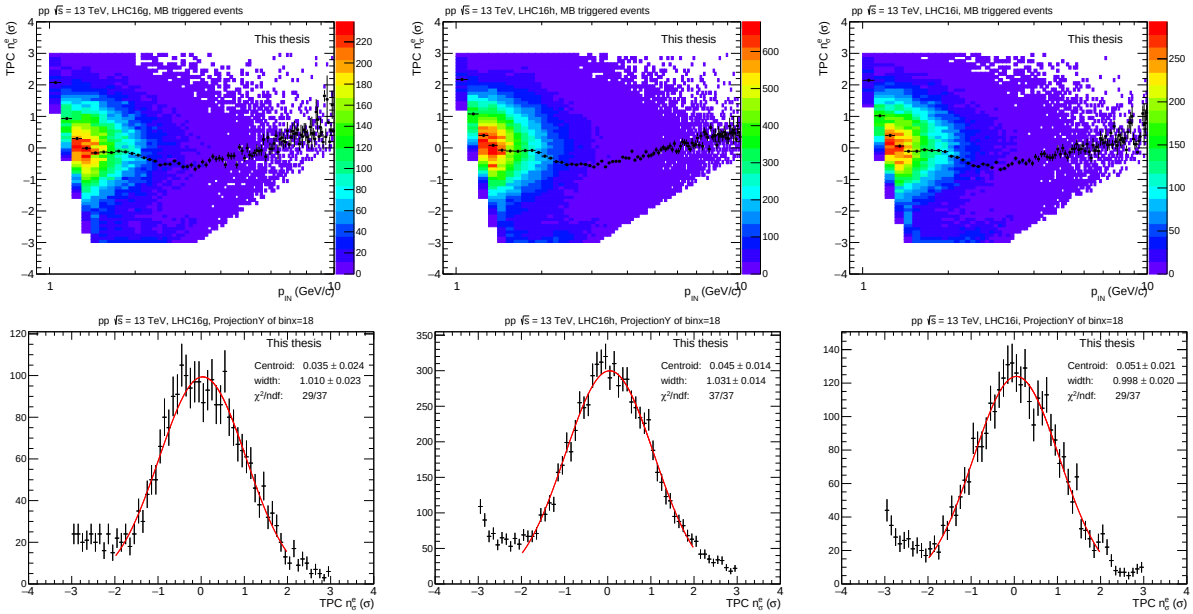

FIGURE B.28: Top: TPC $n\sigma_e$ vs momentum for period LHC16g (left), LHC16h (middle) and LHC16i (right). Bottom: Distribution of selected electron candidates as a function of $n\sigma_e$ in the momentum interval 1.7-1.8 GeV/c fitted with a gaus function for the same periods.

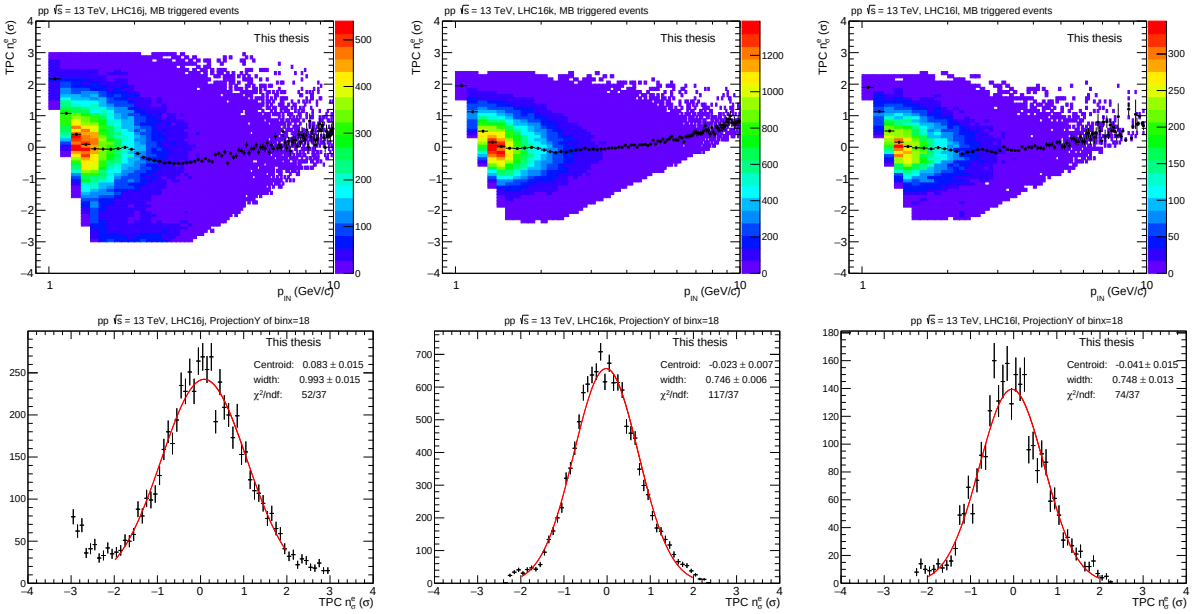

FIGURE B.29: Top: TPC $n\sigma_e$ vs momentum for period LHC16j (left), LHC16k (middle) and LHC16l (right). Bottom: Distribution of selected electron candidates as a function of $n\sigma_e$ in the momentum interval 1.7-1.8 GeV/c fitted with a gaus function for the same periods.

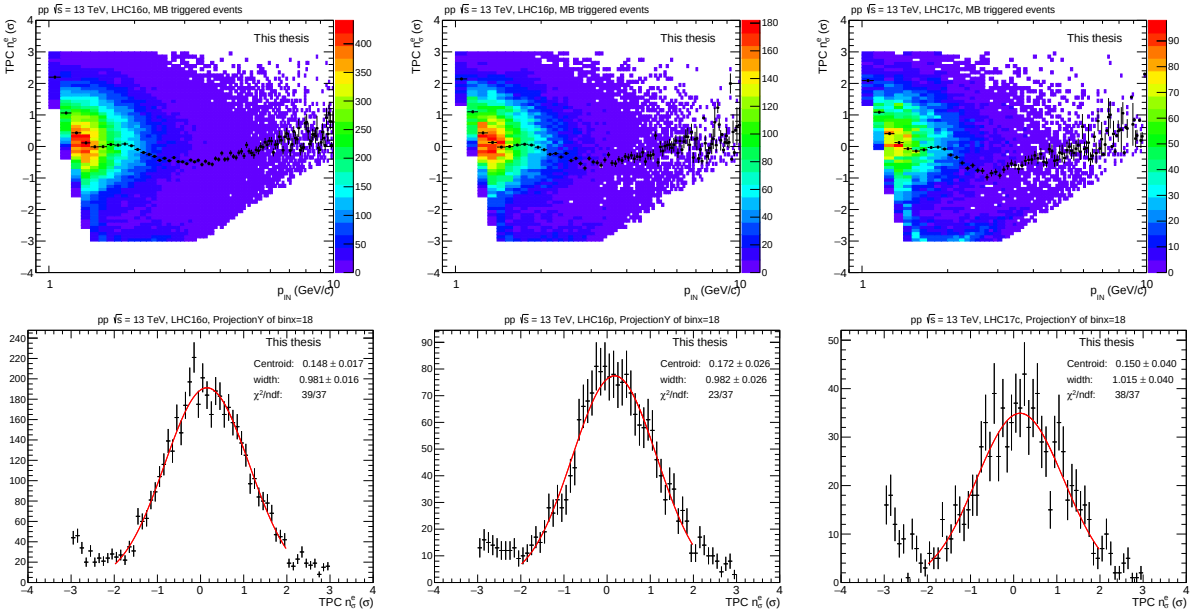

FIGURE B.30: Top: TPC $n\sigma_e$ vs momentum for period LHC16o (left), LHC16p (middle) and LHC17c (right). Bottom: Distribution of selected electron candidates as a function of $n\sigma_e$ in the momentum interval 1.7-1.8 GeV/c fitted with a gaus function for the same periods.

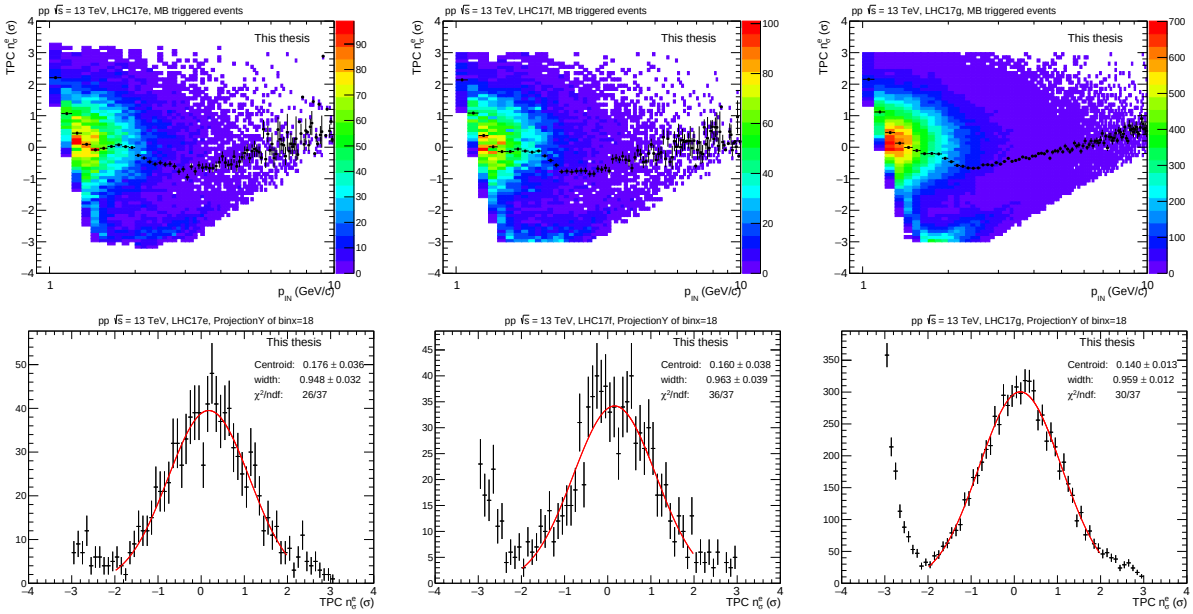

FIGURE B.31: Top: TPC $n\sigma_e$ vs momentum for period LHC17e (left), LHC17f (middle) and LHC17g (right). Bottom: Distribution of selected electron candidates as a function of $n\sigma_e$ in the momentum interval 1.7-1.8 GeV/c fitted with a gaus function for the same periods.

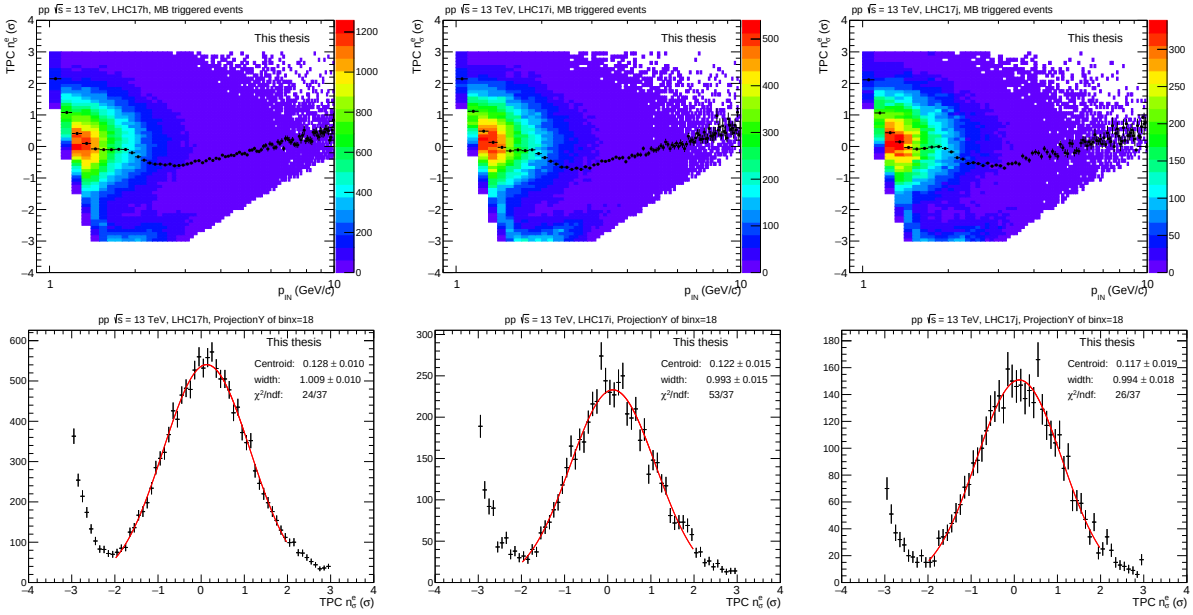

FIGURE B.32: Top: TPC $n\sigma_e$ vs momentum for period LHC17h (left), LHC17i (middle) and LHC17j (right). Bottom: Distribution of selected electron candidates as a function of $n\sigma_e$ in the momentum interval 1.7-1.8 GeV/c fitted with a gaus function for the same periods.

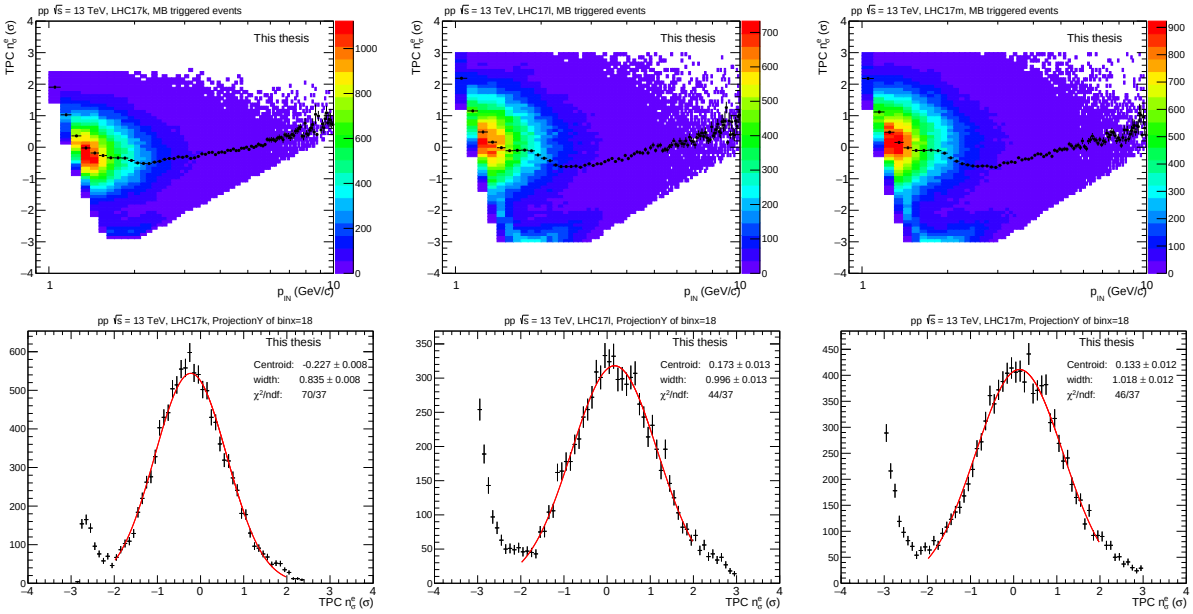

FIGURE B.33: Top: TPC $n\sigma_e$ vs momentum for period LHC17k (left), LHC17l (middle) and LHC17m (right). Bottom: Distribution of selected electron candidates as a function of $n\sigma_e$ in the momentum interval 1.7-1.8 GeV/c fitted with a gaus function for the same periods.

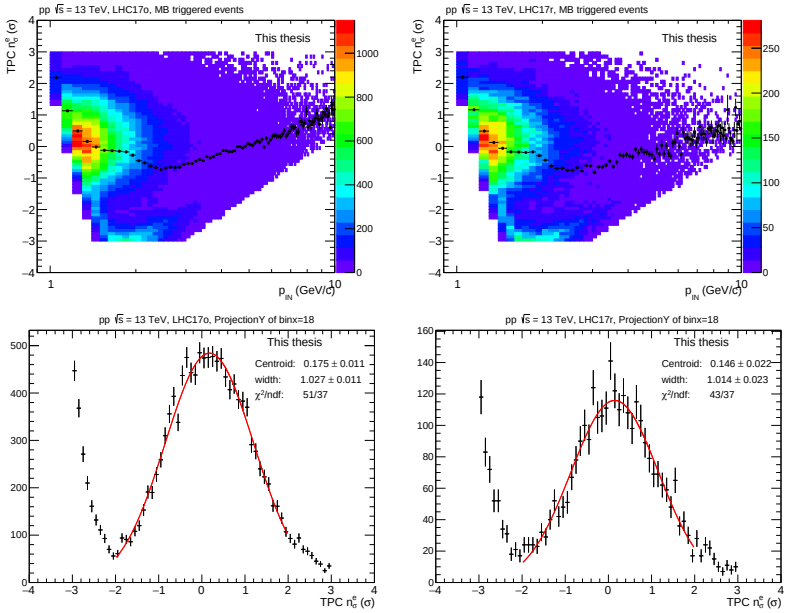

FIGURE B.34: Top: TPC $n\sigma_e$ vs momentum for period LHC17o (left) and LHC17r (right). Bottom: Distribution of selected electron candidates as a function of $n\sigma_e$ in the momentum interval 1.7-1.8 GeV/c fitted with a gaus function for the same periods.

B.4.5 Calibration maps

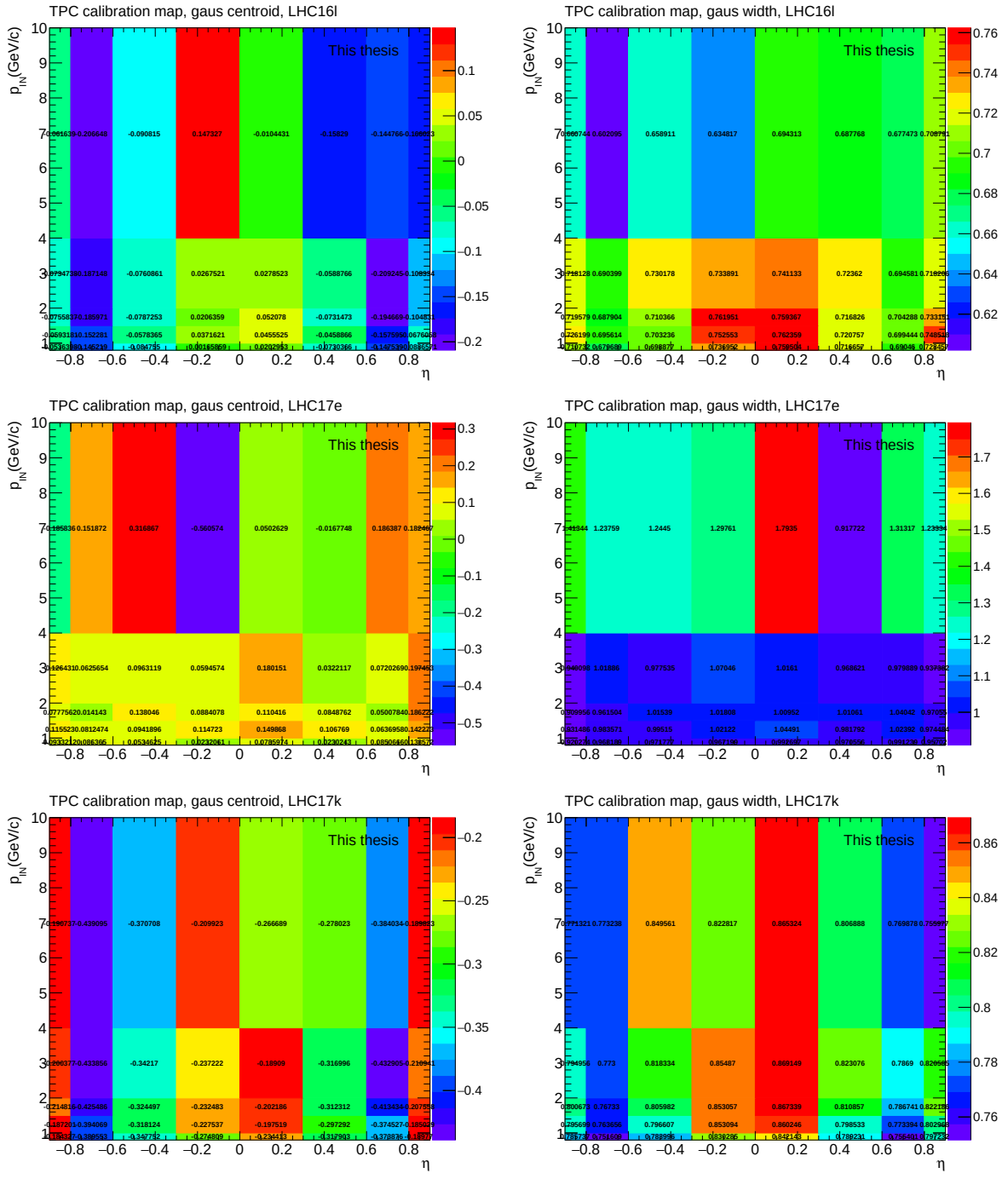

FIGURE B.35: TPC calibration maps. mean to the left and width to the right. From the top, maps for LHC16l, LHC17e, and LHC17k.

B.4.6 TPC $n\sigma_e$ vs momentum as reconstructed by the TPC after post calibration

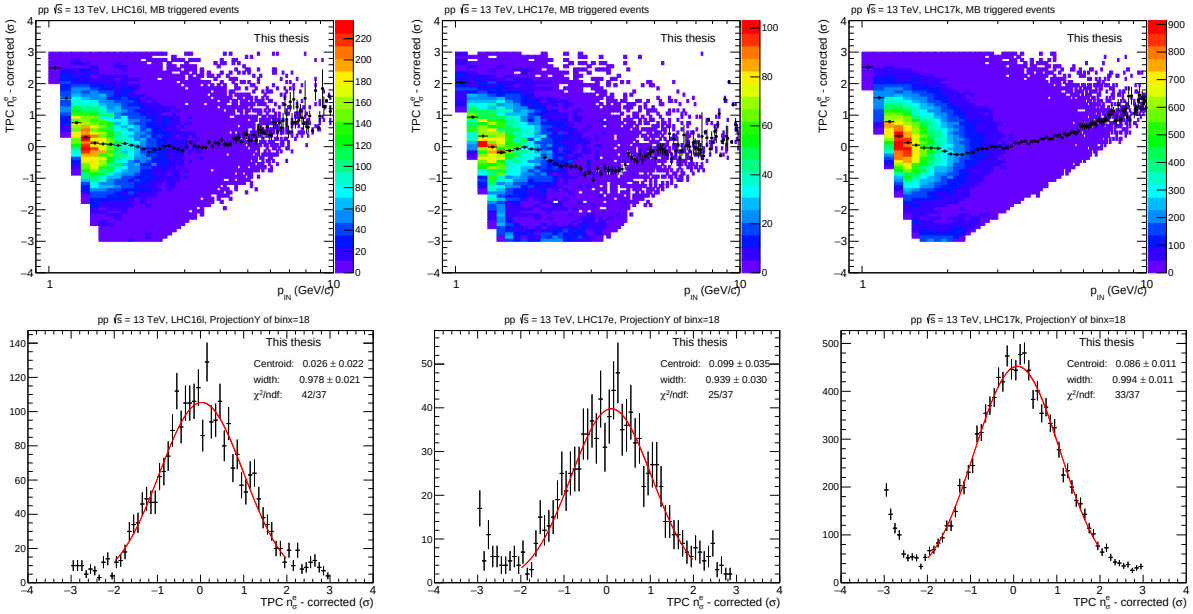

FIGURE B.36: Top: TPC $n\sigma_e$ versus momentum as reconstructed by the TPC after post calibration for period LHC16l (left), LHC17e (middle) and LHC17k (right). Bottom: Distribution of selected electron candidates as a function of $n\sigma_e$ in the momentum interval 1.7-1.8 GeV/c fitted with a gaus function for the same periods after post calibration.

Appendix C

p_{T} differential systematic uncertainty

C.1 Tracking cut variations

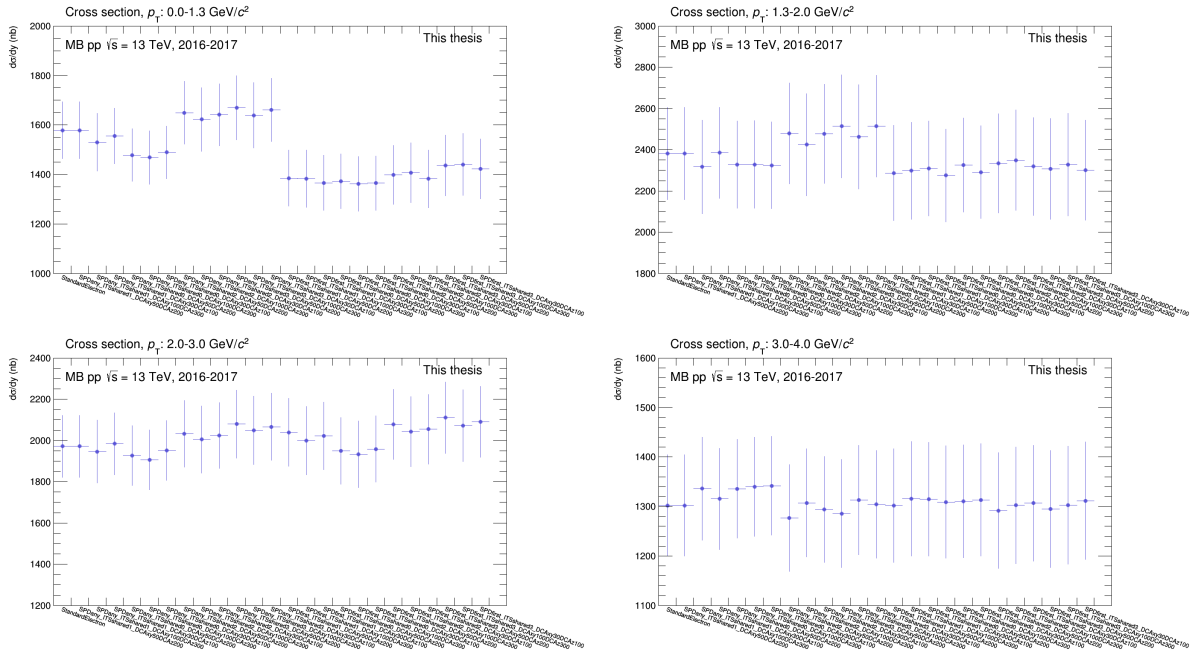

FIGURE C.1: Inclusive J/ψ cross section obtained for each tracking cut configuration, for p_{T} bins 0-4 GeV/c

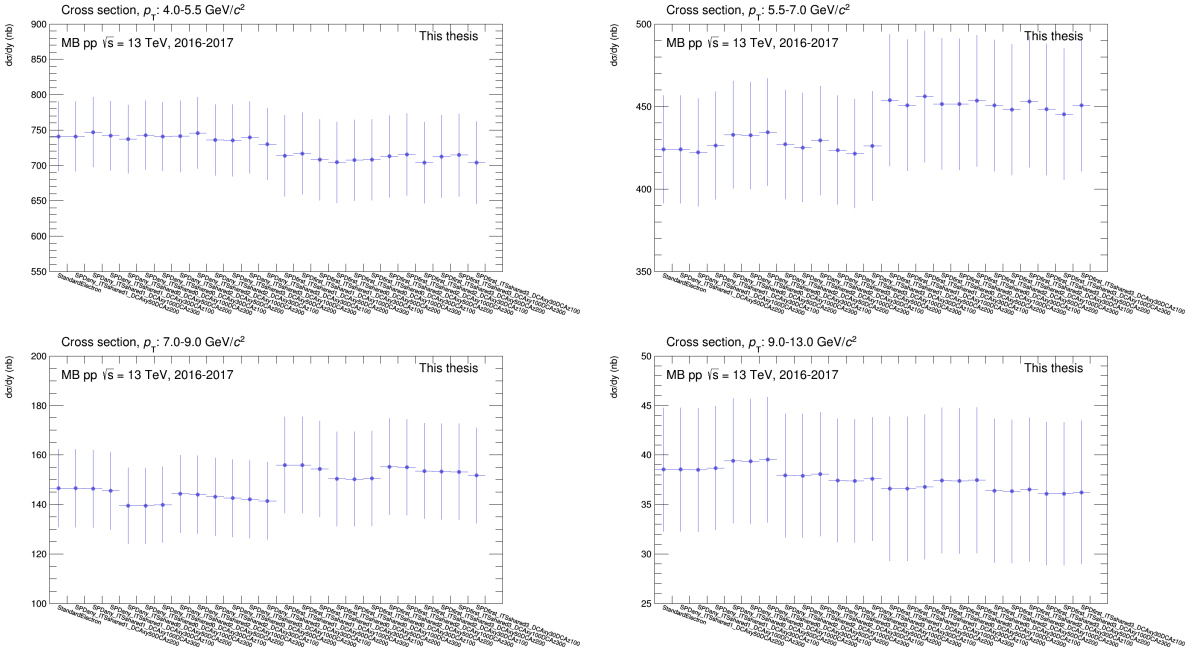

FIGURE C.2: Inclusive J/ψ cross section obtained for each tracking cut configuration, for all p_{T} bins 4-13 GeV/c

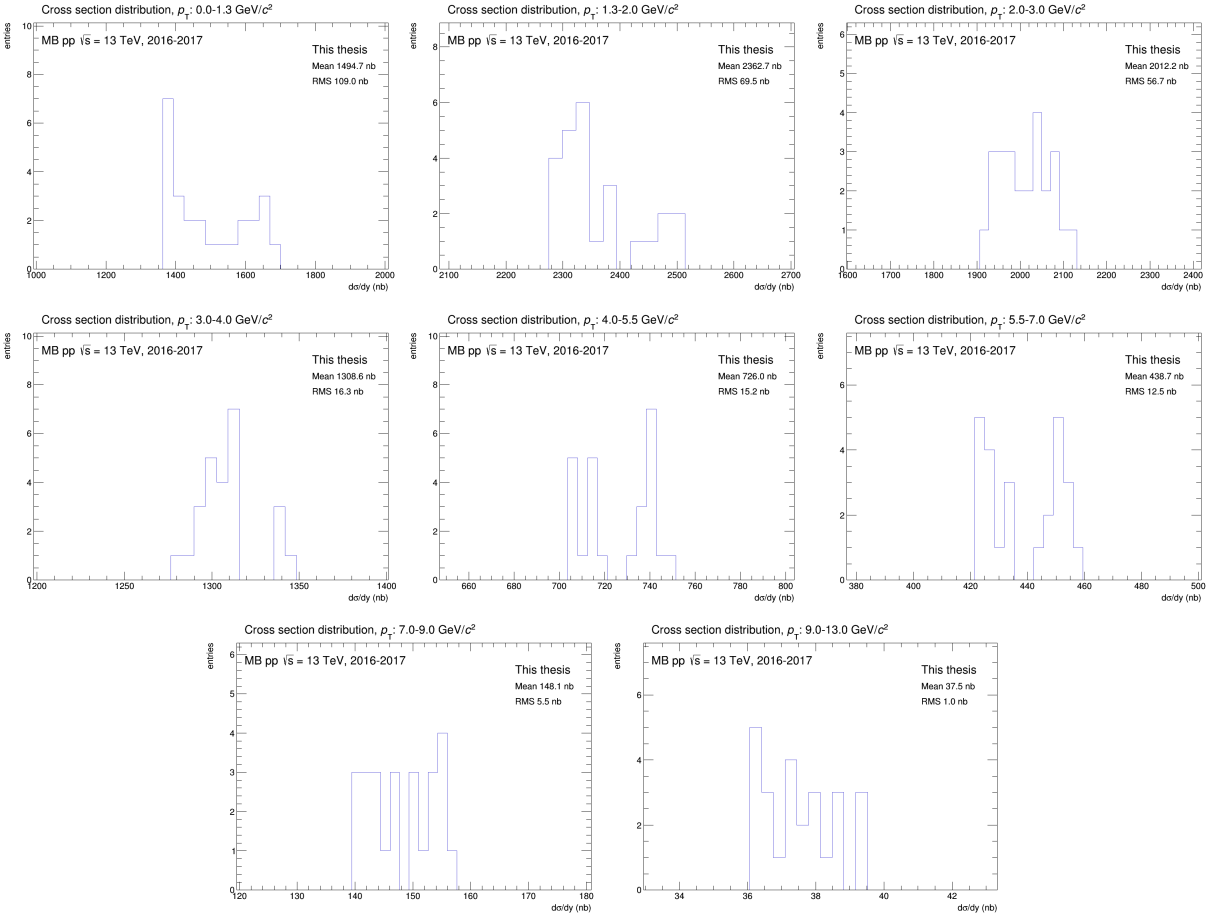

FIGURE C.3: Distribution of cross section for all considered track cut variations all p_{T} bins.

C.2 Signal window variations

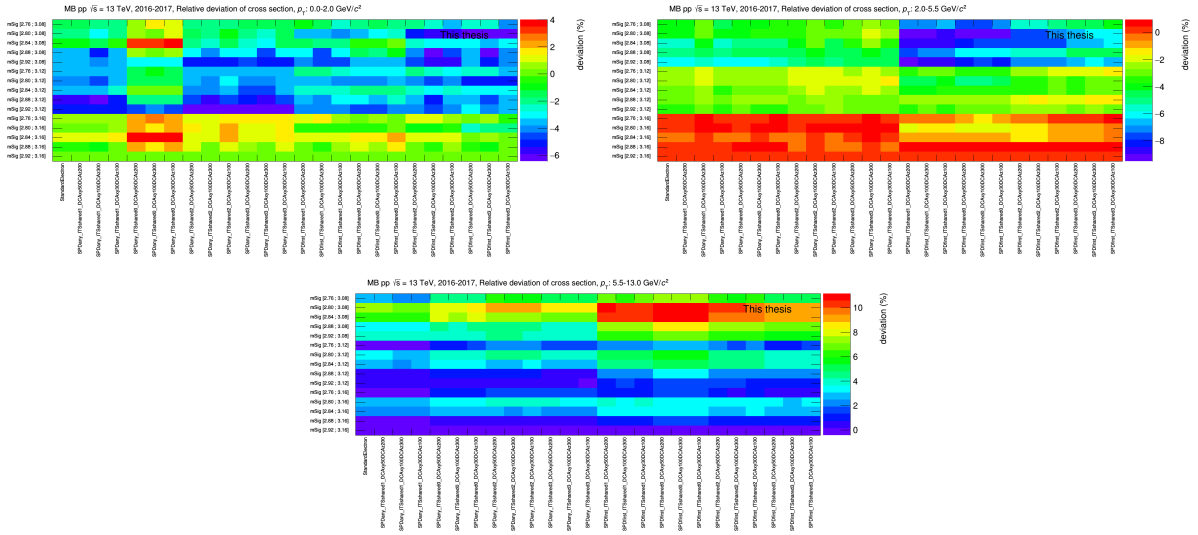

FIGURE C.4: The relative deviation in percent for each tracking cut variation along the x-axis and every signal extraction variation along the y-axis. The relative deviation is displayed for all p_{T} bins

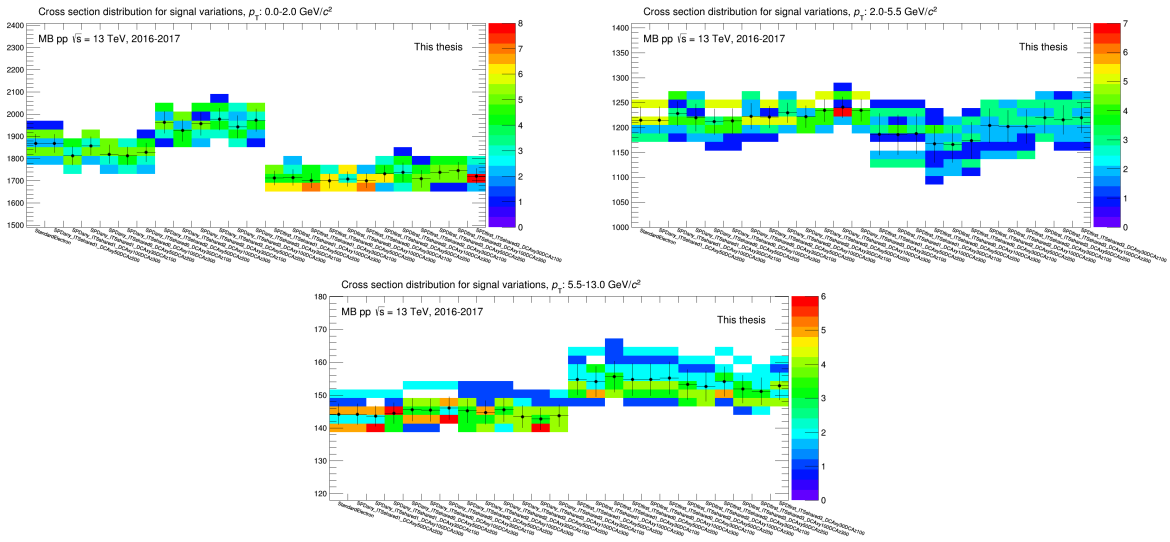

FIGURE C.5: The distribution of the inclusive J/ψ cross section obtained from variations of the signal window for each tracking variation for each p_{T} bin. The mean of the distribution is shown in black points where the uncertainty represents the RMS distribution.

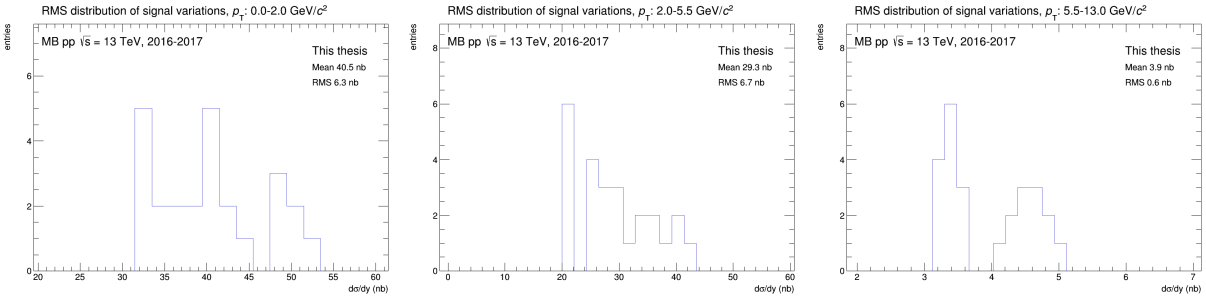

FIGURE C.6: The RMS distribution obtained from signal window variations for each p_{T} bin. Each of the considered tracking cut settings has one entry in the histograms.

C.3 Fit range variations

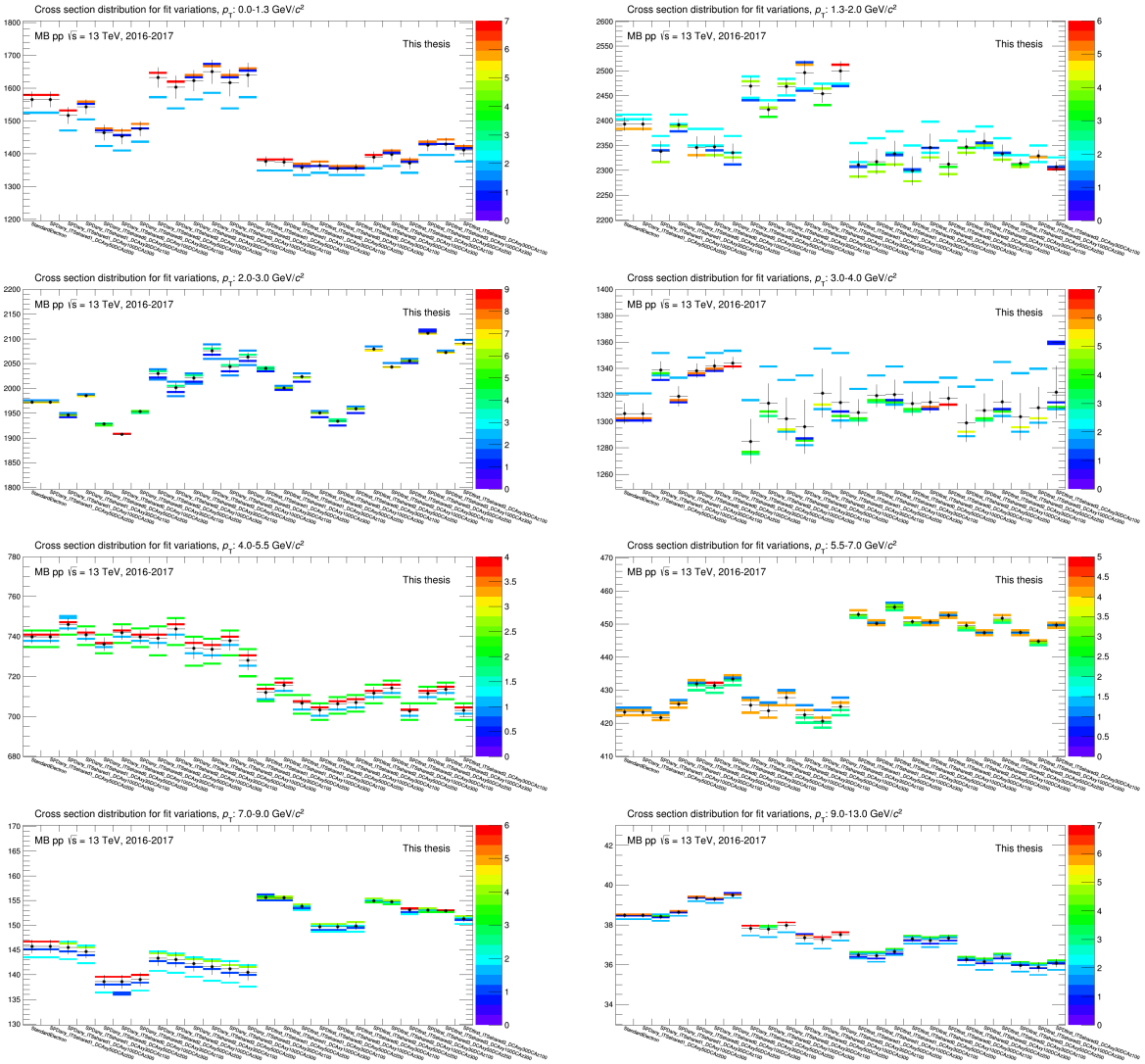

FIGURE C.7: The distribution of the inclusive J/ψ cross section obtained from variations of the fit ranges for each tracking variation for each p_{T} bin. The mean of the distribution is shown in black points where the uncertainty represents the RMS distribution.

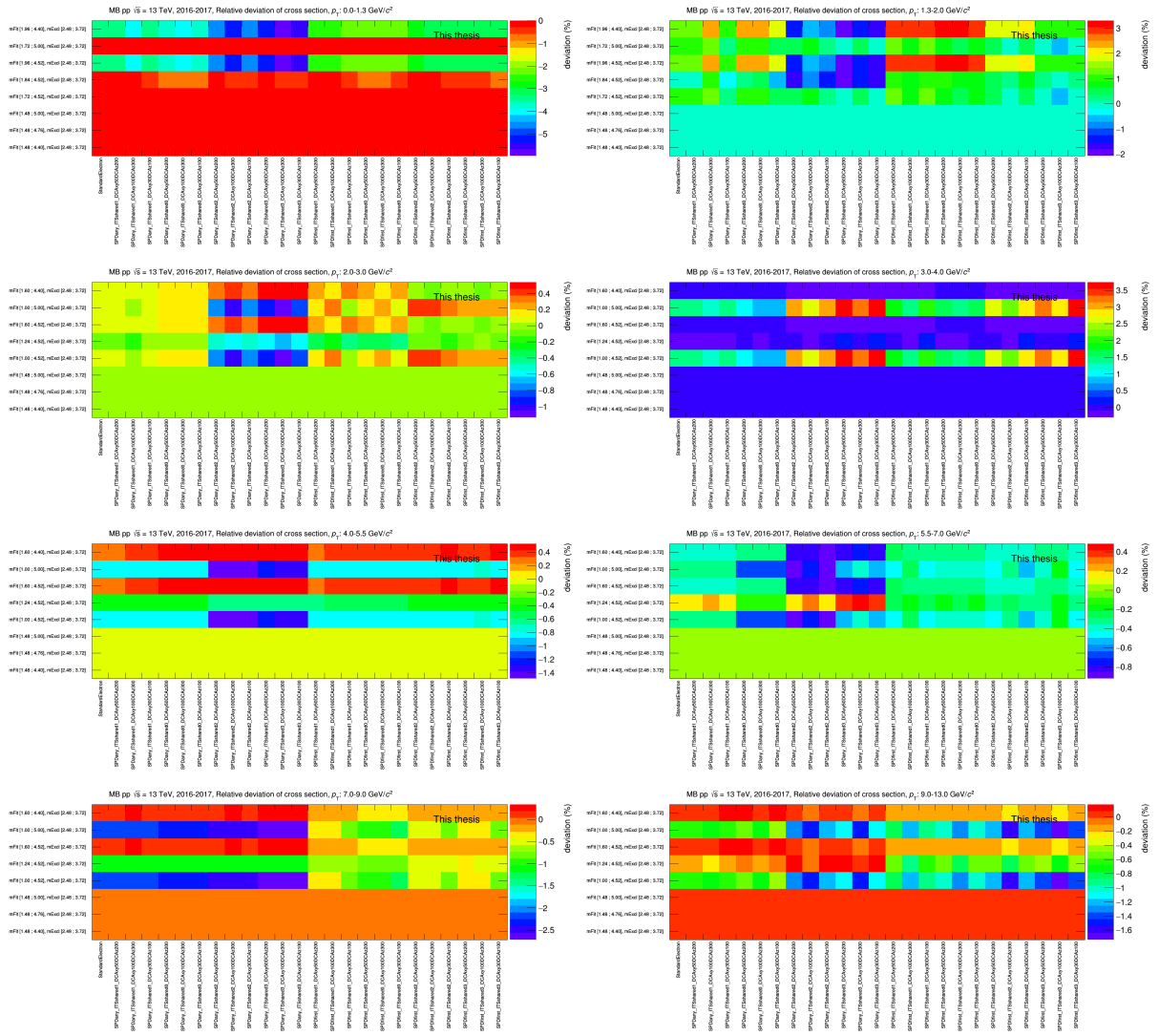

FIGURE C.8: The relative deviation in percent for each tracking cut variation along the x-axis and every signal extraction variation along the y-axis. The relative deviation is displayed for all p_T bins

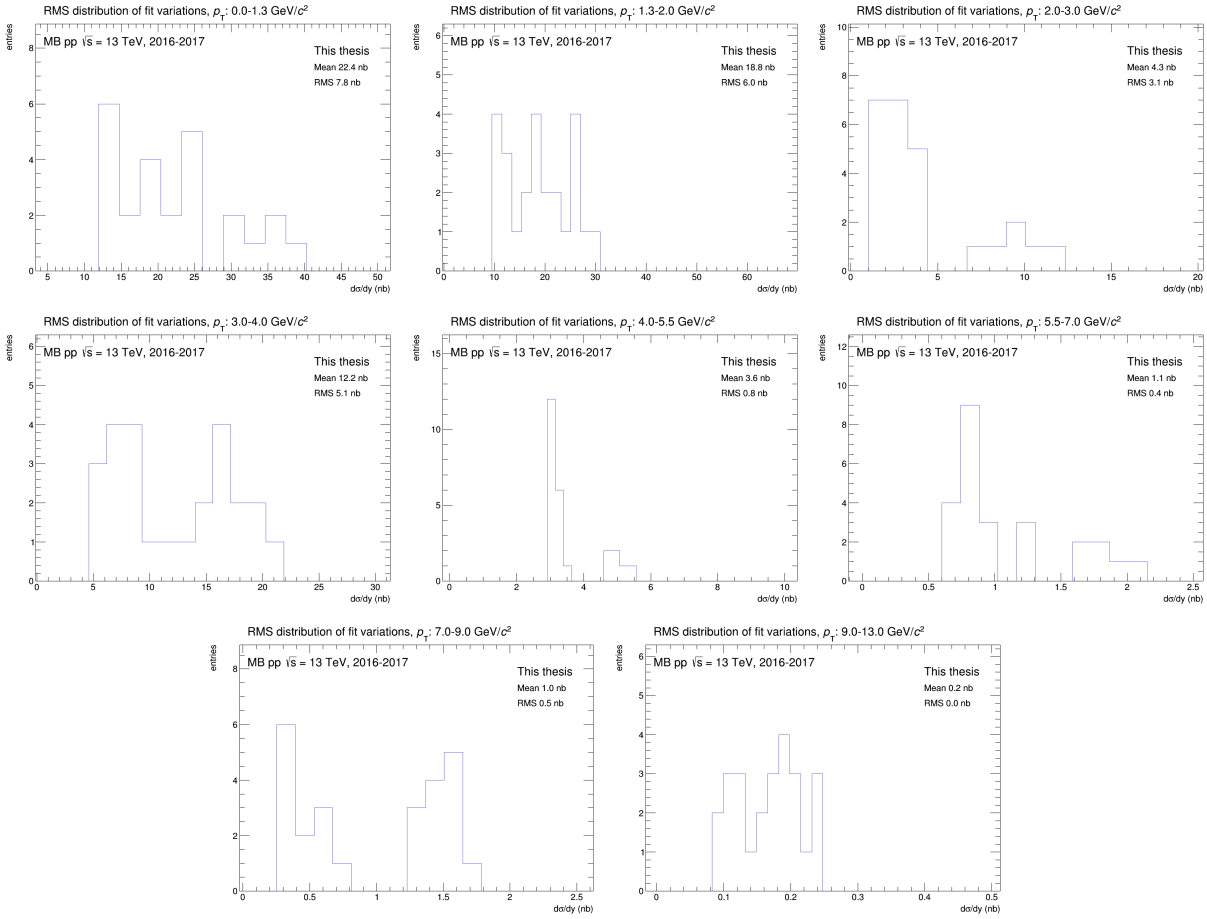

FIGURE C.9: The RMS distribution obtained from fit range variations for each p_{T} bin. Each of the considered tracking cut settings has one entry in the histograms.

C.4 PID cut variations

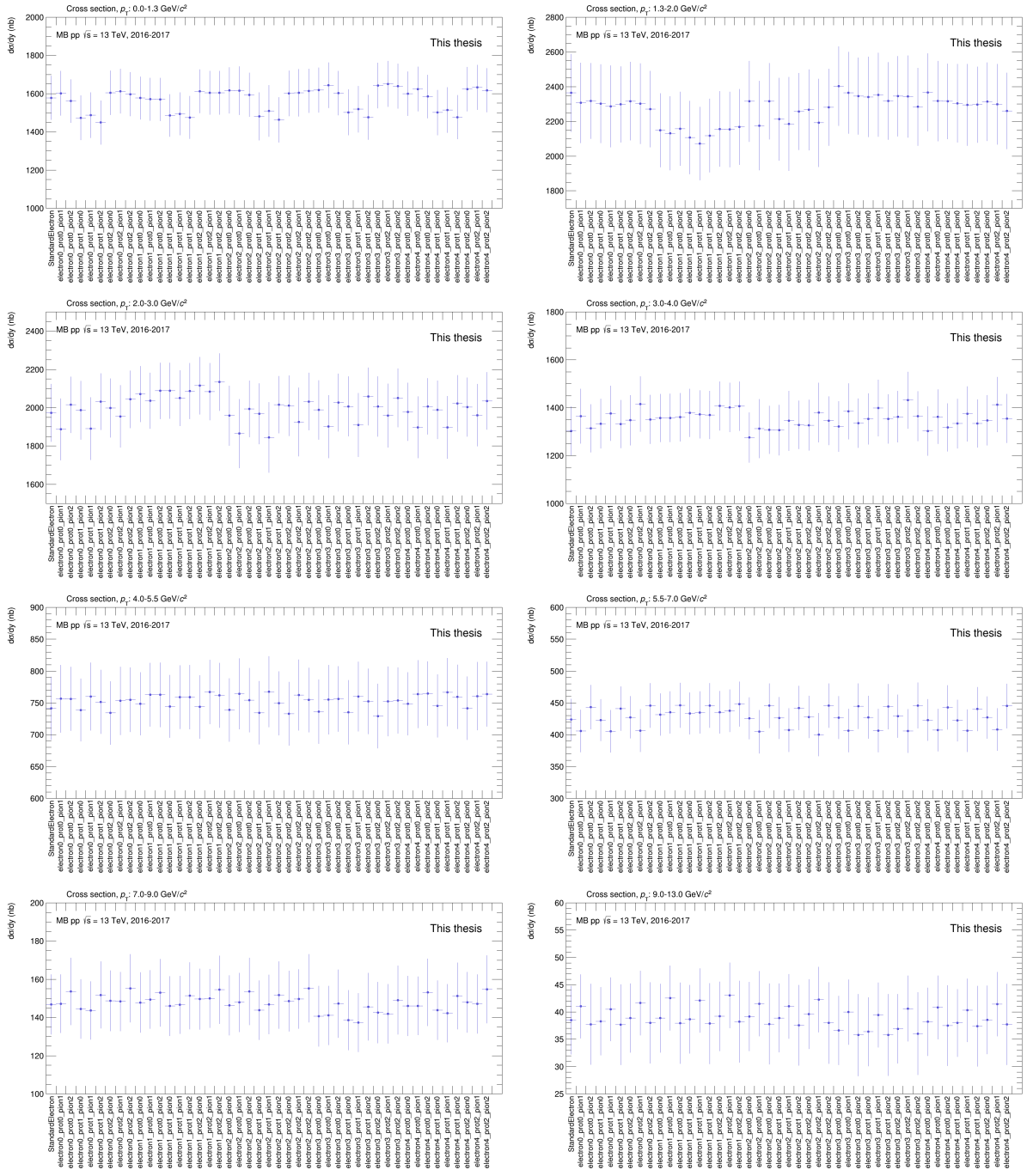

FIGURE C.10: Inclusive J/ψ cross section obtained for each tracking cut configuration, for all p_T.

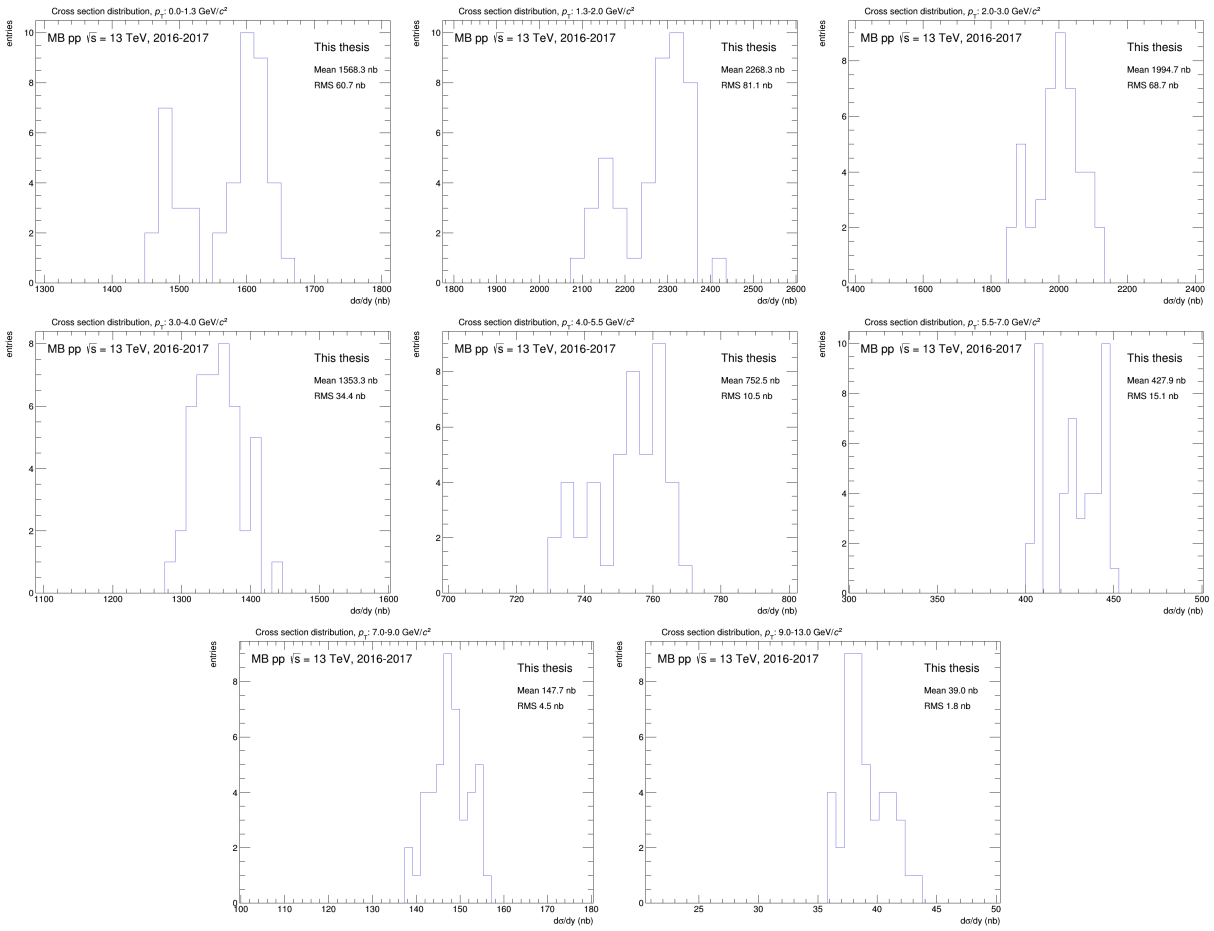

FIGURE C.11: Distribution of cross section for all considered track cut variations all p_T bins.

C.5 Signal extraction using the full fit method

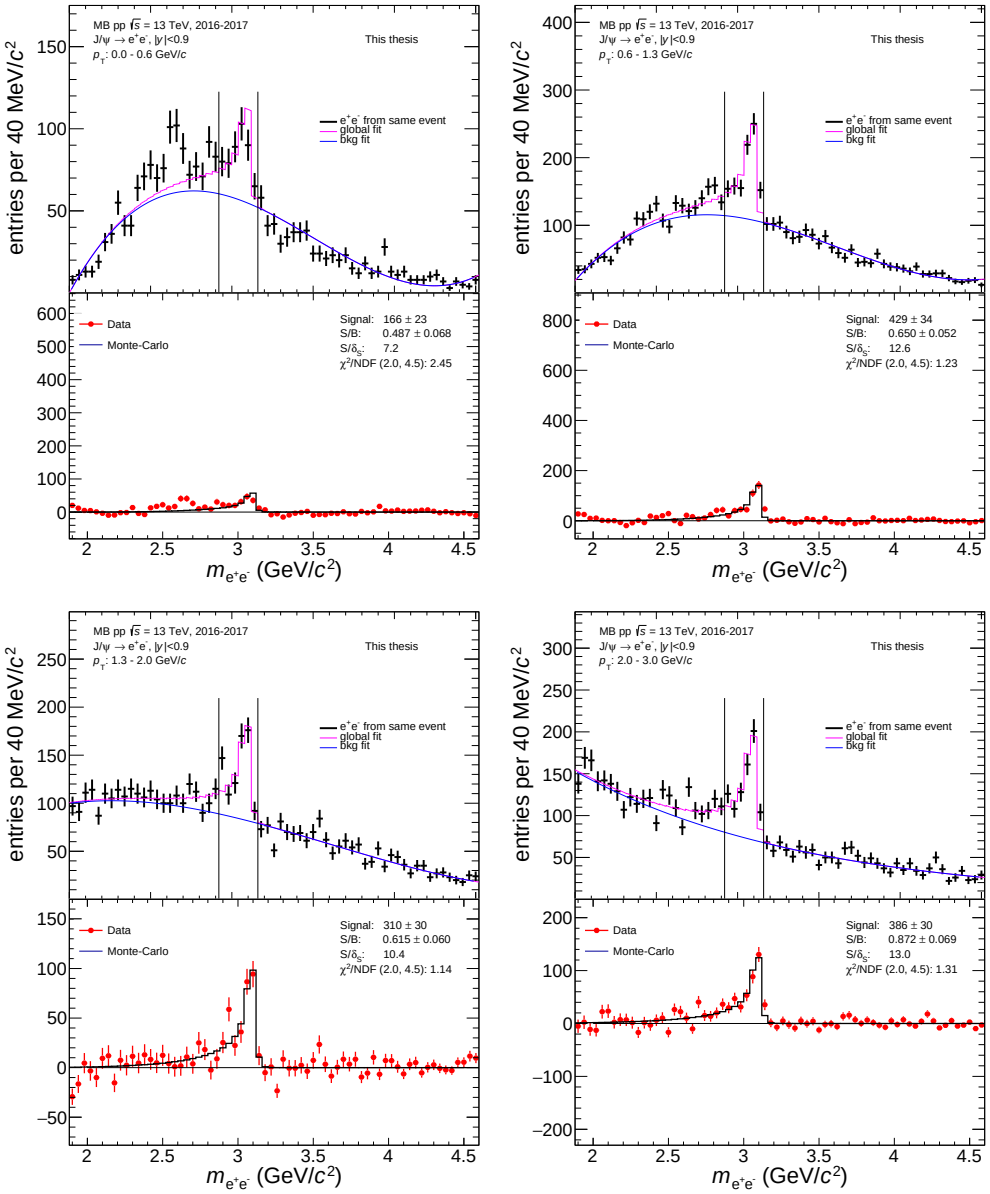

FIGURE C.12: Signal extraction using the full fit background method for p_{T} bins 0.0-0.6 GeV/c (top left), 0.6-1.3 GeV/c (top right), 1.3-2.0 GeV/c (bottom left), and 2.0-3.0 GeV/c (bottom right).

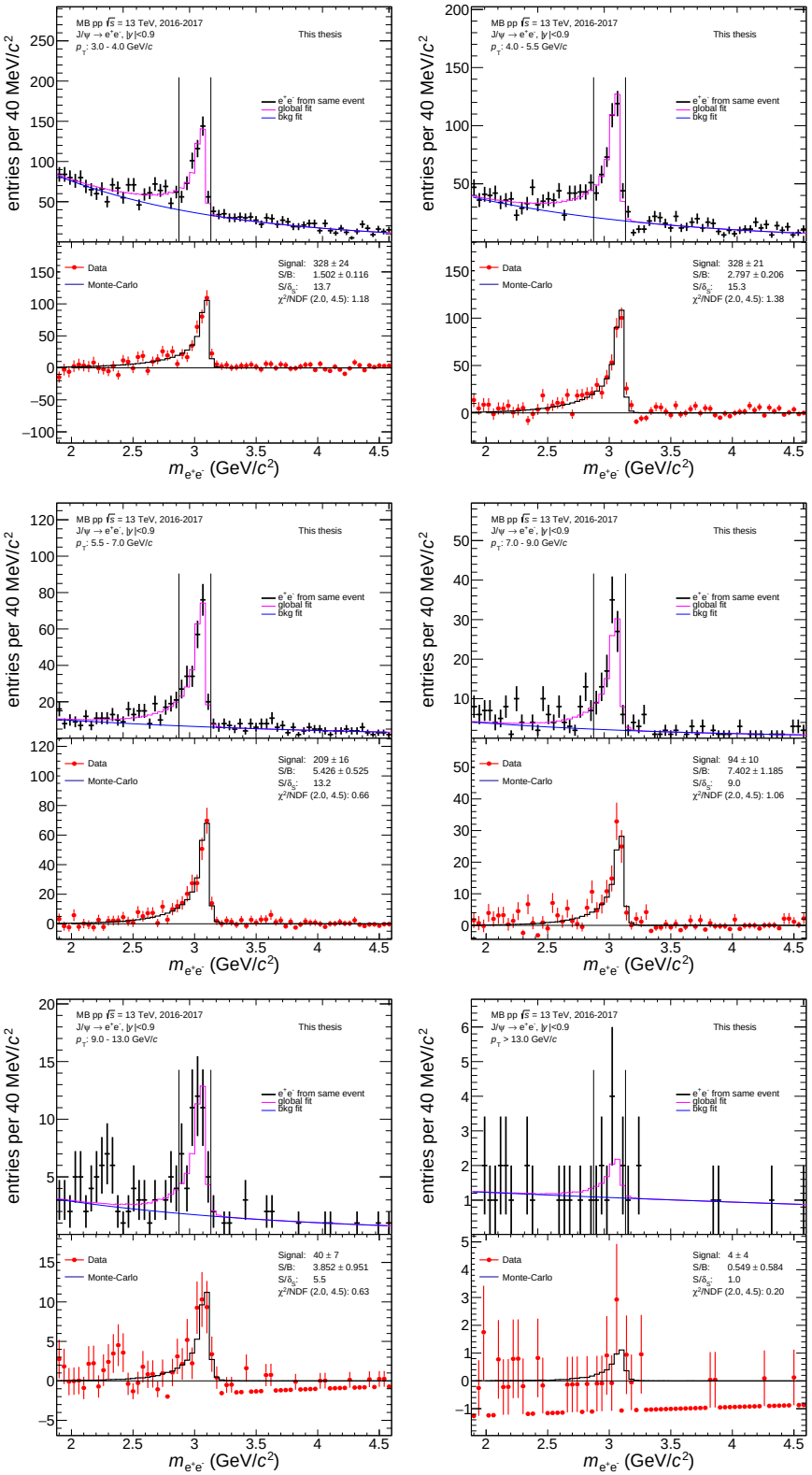

FIGURE C.13: Signal extraction using the full fit background method for p_T bins 3.0-4.0 GeV/c (top left), 4.0-5.5 GeV/c (top right), 5.5-7.0 GeV/c (middle left), 7.0-9.0 GeV/c (middle right), 9.0-13.0 GeV/c (bottom left), and >13.0 GeV/c (bottom right). For p_T >13.0 GeV/c only fluctuations are observed.

Appendix D

Acronyms and Technical Terms

ACORDE	ALICE cosmic ray detector
ALICE	A Large Ion Collider Experiment
ATLAS	A Toroidal LHC Apparatus
BNL	Brookhaven National Laboratory
CEM	Color-evaporation model
CERN	European Organization for Nuclear Research
CDF	Collider Detector at Fermilab
CGC	Color Glass Condensate
CMS	Compact Muon Solenoid experiment
CSM	Color-singlet model
DCA	distance of closest approach
DCal	Di-jet Calorimeter
DPG	ALICE Data Preparation Group
EMCal	Electromagnetic Calorimeter
ESD	Event Summary Data

FMD Forward Multiplicity Detector

FNAL Fermi National Accelerator Laboratory

FONLL Fixed-Order-Next-to-Leading Logarithm

HMPID High Momentum Particle Identification Detector

ITS Inner Tracking System

LHC Large Hadron Collider

LHCb LHC beauty experiment

LO Leading Order

LQCD Lattice QCD

MB Minimum Bias

MC Monte Carlo

MWPC multi-wire-proportional chambers

NLO Next-to-Leading Order

NNLO Next-to-Next-to Leading Order

NRQCD non-relativistic QCD

PDF Parton distribution function

PHOS Photon Spectrometer

RICH Ring Imaging Cherenkov detector

PDF parton distribution functions

PHENIX Pioneering High Energy Nuclear Interactions eXperiment

PID particle identification

PMD Photon Multiplicity Detector

QCD	Quantum Chromodynamics
QED	Quantum Electrodynamics
QGP	Quark-Gluon Plasma
RHIC	Relativistic Heavy Ion Collider
SDD	Silicon Drift Detectors
SLAC	Stanford Linear Accelerator Center
SM	Standard Model
SPD	Silicon Pixel Detectors
SPS	Super Proton Synchrotron
SSD	Silicon Strip Detectors
TZERO	Timing and Trigger detector at ALICE
TOF	Time-Of-Flight detector
TPC	Time Projection Chamber
TRD	Transition Radiation Detector
V0	VZERO
vdM	Van der Meer
ZDC	Zero Degree Calorimeter

Bibliography

[1] **ALICE**, K. Aamodt *et al.*, "The ALICE experiment at the CERN LHC", *JINST* **3** (2008) S08002.

[2] **ATLAS**, S. Akatsuka, "The Phase-1 Upgrade of the ATLAS Level-1 Endcap Muon Trigger", *Springer Proc. Phys.* **212** (2018) 341–345, arXiv:1806.09234.

[3] M. Thomson, "Modern particle physics", Cambridge University Press, New York, 2013.

[4] **CMS**, V. Khachatryan *et al.*, "Constraints on parton distribution functions and extraction of the strong coupling constant from the inclusive jet cross section in pp collisions at $\sqrt{s} = 7$ TeV", *Eur. Phys. J.* **C75** (2015), no. 6, 288, arXiv:1410.6765.

[5] R. Gupta, "Introduction to lattice QCD: Course", in "Probing the standard model of particle interactions. Proceedings, Summer School in Theoretical Physics, NATO Advanced Study Institute, 68th session, Les Houches, France, July 28-September 5, 1997. Pt. 1, 2", pp. 83–219. 1997. arXiv:hep-lat/9807028.

[6] E. Eichten, K. Gottfried, T. Kinoshita, J. Kogut, K. D. Lane, and T. M. Yan, "Spectrum of charmed quark-antiquark bound states", *Phys. Rev. Lett.* **34** Feb (1975) 369–372.

[7] D. J. Gross and F. Wilczek, "Ultraviolet Behavior of Nonabelian Gauge Theories", *Phys. Rev. Lett.* **30** (1973) 1343–1346, [,271(1973)].

[8] H. D. Politzer, "Reliable Perturbative Results for Strong Interactions?", *Phys. Rev. Lett.* **30** (1973) 1346–1349, [,274(1973)].

[9] E. Shuryak, "Quark-gluon plasma and hadronic production of leptons, photons and psions", *Physics Letters B* **78** (1978), no. 1, 150 – 153.

[10] R. Hagedorn, "Statistical thermodynamics of strong interactions at high-energies", *Nuovo Cim. Suppl.* **3** (1965) 147–186 CERN-TH-520.

[11] R. S. Bhalerao, "Relativistic heavy-ion collisions", Apr 2014 TIFR-TH-14-11, Comments: Updated version of the lectures given at the First Asia-Europe-Pacific School of

High-Energy Physics, Fukuoka, Japan, 14-27 October 2012. Published as a CERN Yellow Report (CERN-2014-001) and KEK report (KEK-Proceedings-2013-8), K. Kawagoe and M. Mulders (eds.), 2014, p. 219. Total 21 pages.

[12] S. Borsanyi *et al.*, "The QCD equation of state with dynamical quarks", *JHEP* **11** (2010) 077, arXiv:1007.2580.

[13] S. Borsanyi, Z. Fodor, C. Hoelbling, S. D. Katz, S. Krieg, and K. K. Szabo, "Full result for the QCD equation of state with 2+1 flavors", *Phys. Lett.* **B730** (2014) 99–104, arXiv:1309.5258.

[14] U. W. Heinz and M. Jacob, "Evidence for a new state of matter: An Assessment of the results from the CERN lead beam program", arXiv:nucl-th/0002042.

[15] **BRAHMS**, I. Arsene *et al.*, "Quark gluon plasma and color glass condensate at RHIC? The Perspective from the BRAHMS experiment", *Nucl. Phys.* **A757** (2005) 1–27, arXiv:nucl-ex/0410020.

[16] B. B. Back *et al.*, "The PHOBOS perspective on discoveries at RHIC", *Nucl. Phys.* **A757** (2005) 28–101, arXiv:nucl-ex/0410022.

[17] **STAR**, J. Adams *et al.*, "Experimental and theoretical challenges in the search for the quark gluon plasma: The STAR Collaboration's critical assessment of the evidence from RHIC collisions", *Nucl. Phys.* **A757** (2005) 102–183, arXiv:nucl-ex/0501009.

[18] **PHENIX**, K. Adcox *et al.*, "Formation of dense partonic matter in relativistic nucleus-nucleus collisions at RHIC: Experimental evaluation by the PHENIX collaboration", *Nucl. Phys.* **A757** (2005) 184–283, arXiv:nucl-ex/0410003.

[19] "Evolution of collisions and qgp". https://particlesandfriends.wordpress.com/2016/10/14/evolution-of-collisions-and-qgp/. 2018.10.10.

[20] J. Bjorken, "Highly Relativistic Nucleus-Nucleus Collisions: The Central Rapidity Region", *Phys.Rev.* **D27** Jan (1983) 140–151.

[21] P. Braun-Munzinger and J. Stachel, "The quest for the quark-gluon plasma", *Nature* **448** (2007) 302–309.

[22] J. J. Aubert *et al.*, "Experimental observation of a heavy particle j", *Phys. Rev. Lett.* **33** Dec (1974) 1404–1406.

[23] Augustin *et al.*, "Discovery of a narrow resonance in e^+e^- annihilation", *Phys. Rev. Lett.* **33** Dec (1974) 1406–1408.

[24] S. L. Glashow, J. Iliopoulos, and L. Maiani, "Weak interactions with lepton-hadron symmetry", *Phys. Rev. D* **2** Oct (1970) 1285–1292.

[25] G. S. Abrams *et al.*, "The Discovery of a Second Narrow Resonance in e+ e- Annihilation", *Phys. Rev. Lett.* **33** (1974) 1453–1455, [Adv. Exp. Phys.5,150(1976)].

[26] W. R. Innes *et al.*, "Observation of Structure in the Υ Region", *Phys. Rev. Lett.* **39** (1977) 1240–1242, [Erratum: Phys. Rev. Lett.39,1640(1977)].

[27] F. Abe *et al.*, "Identification of top quarks using kinematic variables", *Phys. Rev. D* **52** Sep (1995) R2605–R2609.

[28] I. I. Y. Bigi *et al.*, "Production and Decay Properties of Ultraheavy Quarks", *Phys. Lett.* **B181** (1986) 157–163.

[29] **Particle Data Group**, M. Tanabashi *et al.*, "Review of particle physics", *Phys. Rev. D* **98** Aug (2018) 030001.

[30] E. Eichten *et al.*, "Spectrum of charmed quark-antiquark bound states", *Phys. Rev. Lett.* **34** Feb (1975) 369–372.

[31] M. A. Winn and J. Stachel, "Inclusive J/ψ production at mid-rapidity in p-Pb collisions at $\sqrt{^sNN}$=5.02 TeV", PhD thesis, Feb 2016. Presented 28 Apr 2016. `https://cds.cern.ch/record/2151926`

[32] G. I. C.Brenner Mariotto, M.B. Gay Ducati, "Soft and hard QCD dynamics in hadroproduction of charmonium", *Eur.Phys.J.* **C23** (2002) 527–538 TSL/ISV-2001-0256.

[33] H.-S. Shao, "Heavy Quarkonium Production Phenomenology and Automation of One-Loop Scattering Amplitude Computations", Springer, Singapore, 2016.

[34] N. Brambilla. *et al.*, "Heavy quarkonium: progress,puzzles, and opportunities", *Eur.Phys.J.* **C71** (2011) 1534, `arXiv:1010.5827`.

[35] F. Abe and others., "Inclusive j/ψ ψ(2s), and b-quark production in p^{-}p collisions at $\sqrt{}$s =1.8 tev", *Phys. Rev. Lett.* **69** Dec (1992) 3704–3708.

[36] E. Braaten, S. Fleming, and T. C. Yuan, "Production of heavy quarkonium in high-energy colliders", *Annual Review of Nuclear and Particle Science* **46** (1996), no. 1, 197–235, `https://doi.org/10.1146/annurev.nucl.46.1.197`.

[37] J. Lansberg, "J/psi,psi' and Upsilon Production at Hadron Colliders: a review", *Int.J.Mod.Phys.* **A21** (2006) 3857–3916.

[38] J. P. Lansberg, "On the mechanisms of heavy-quarkonium hadroproduction", *Eur. Phys. J.* **C61** (2009) 693–703, arXiv:0811.4005.

[39] J. Amundson *et al.*, "Quantitative Tests of Color Evaporation: Charmonium Production", *Phys.Lett.* **B390** (1997) 323–328 MADPH-96-942.

[40] G. L. G.T. Bodwin, E.Braaten, " Rigorous QCD Analysis of Inclusive Annihilation and Production of Heavy Quarkonium", *Phys.Rev.* **D51** (1995) 1125–1171 ANL-HEP-PR-94-24.

[41] **ALICE**, S. Acharya *et al.*, "Energy dependenc of forward/rapidity J/ψ and ψ(2S) production in pp collisions at the LHC", *eur. Phys. J.* **C77** (2017), no. 6, 392, arXiv:1702.00557.

[42] **ALICE**, S. Acharya *et al.*, "Measurement of the inclusive J/ ψ polarization at forward rapidity in pp collisions at $\sqrt{\mathbf{s}} = \mathbf{8}$ TeV", *Eur. Phys. J.* **C78** (2018), no. 7, 562, arXiv:1805.04374.

[43] T. Matsui and H. Satz, "J/ψ Suppression by Quark-Gluon Plasma Formation", *Phys. Lett.* **B178** (1986) 416–422.

[44] H. Satz, "Charm and beauty in a hot environment", 2006 BI-TP 2006/06.

[45] **ALICE**, S. Acharya *et al.*, "Searches for transverse momentum dependent flow vector fluctuations in Pb-Pb and p-Pb collisions at the LHC", *JHEP* **09** (2017) 032, arXiv:1707.05690.

[46] **ALICE**, S. Acharya *et al.*, "Inclusive J/ψ production in Xe–Xe collisions at $\sqrt{s_{\rm NN}} = 5.44$ TeV", *Phys. Lett.* **B785** (2018) 419–428, arXiv:1805.04383.

[47] **PHENIX**, A. Adare *et al.*, "j/ψ suppression at forward rapidity in au + au collisions at $\sqrt{s_{NN}} = 200$ gev", *Phys. Rev. C* **84** Nov (2011) 054912.

[48] e. Evans, L. and e. Bryant, P., "LHC Machine", *JINST* **3** (2008) S08001.

[49] M. Benedikt, P. Collier, V. Mertens, J. Poole, and K. Schindl, "LHC Design Report. 3. The LHC injector chain", 2004.

[50] **ATLAS**, G. Aad *et al.*, "The ATLAS Experiment at the CERN Large Hadron Collider", *JINST* **3** (2008) S08003.

[51] **CMS**, S. Chatrchyan *et al.*, "The CMS Experiment at the CERN LHC", *JINST* **3** (2008) S08004.

[52] **LHCb**, A. A. Alves, Jr. *et al.*, "The LHCb Detector at the LHC", *JINST* **3** (2008) S08005.

[53] **ATLAS**, G. Aad *et al.*, "Observation of a new particle in the search for the Standard Model Higgs boson with the ATLAS detector at the LHC", *Phys. Lett.* **B716** (2012) 1–29, arXiv:1207.7214.

[54] **CMS**, S. Chatrchyan *et al.*, "Observation of a new boson at a mass of 125 GeV with the CMS experiment at the LHC", *Phys. Lett.* **B716** (2012) 30–61, arXiv:1207.7235.

[55] F. Marcastel, "CERN's Accelerator Complex. La chaîne des accélérateurs du CERN", Oct 2013 OPEN-PHO-CHART-2013-001, General Photo.

[56] **ALICE**, B. B. Abelev *et al.*, "Performance of the ALICE Experiment at the CERN LHC", *Int. J. Mod. Phys.* **A29** (2014) 1430044 CERN-PH-EP-2014-031, arXiv:1402.4476.

[57] **ALICE**, K. Aamodt *et al.*, "Production of pions, kaons and protons in pp collisions at $\sqrt{s} = 900$ GeV with ALICE at the LHC", *Eur. Phys. J* **C71** (2011) 1655.

[58] **ALICE**, "Alice webpage". http://aliceinfo.cern.ch/. 2018.10.10.

[59] F. Kramer, "J/ψ production in $\sqrt{s} = 7$ *tev* pp collisions", PhD thesis, Johann Wolfgang Goethe-Universitat in Frankfurt am Main, 2012. 2018.08.16. https://www.uni-frankfurt.de/48069284/PHD-Frederick_Kramer.pdf

[60] **ALICE**, "Aliroot". http://svnweb.cern.ch/world/wsvn/AliRoot/, a. 2018.10.08.

[61] **ALICE**, "Aliphysics". https://github.com/alisw/AliPhysics/, b. 2018.10.08.

[62] **ALICE**, "Root webpage". http://root.cern.ch/. 2018.10.08.

[63] T. Sjöstrand, S. Mrenna, and P. Z. Skands, "A Brief Introduction to PYTHIA 8.1", *Comput.Phys.Commun.* **178** (2008) 852–867, arXiv:0710.3820.

[64] **GEANT4**, S. Agostinelli *et al.*, "GEANT4: A Simulation toolkit", *Nucl.Instrum.Meth.* **A506** (2003) 250–303.

[65] **ALICE**, "ALICE technical design report of the computing", 2005.

[66] **ALICE**, "Analysis framework". http://alice-offline.web.cern.ch/Activities/Analysis/AnalysisFramework/index.html. 2018.21.09.

[67] **ALICE**, P. Saiz, L. Aphecetche, P. Buncic, R. Piskac, J. E. Revsbech, and V. Sego, "AliEn - ALICE environment on the GRID", *Nucl. Instrum. Meth.* **A502** (2003) 437–440.

[68] **ALICE**, D. P. Group, "List of good runs for run2 periods".

https://twiki.cern.ch/twiki/bin/viewauth/ALICE/AliDPGRunLists. 2018.10.08.

[69] E. Barberio, B. van Eijk, and Z. Was, "PHOTOS: A Universal Monte Carlo for QED radiative corrections in decays", *Comput. Phys. Commun.* **66** (1991) 115–128.

[70] **ALICE**, Data Preparation Group, "Central barrel simulation with injected J/ψ, anchored to 2016 periods from pp at 13 TeV".
https://alice.its.cern.ch/jira/browse/ALIROOT-7416. 2018.10.08.

[71] S. van der Meer, "Calibration of the effective beam height in the ISR", Tech. Rep. CERN-ISR-PO-68-31. ISR-PO-68-31, CERN, Geneva, 1968.

[72] **ALICE**, "ALICE luminosity determination for pp collisions at $\sqrt{s} = 13$ TeV", Jun 2016 ALICE-PUBLIC-2016-002.

[73] R. Barlow, "Systematic errors: Facts and fictions", in "Advanced Statistical Techniques in Particle Physics. Proceedings, Conference, Durham, UK, March 18-22, 2002", pp. 134–144. 2002. arXiv:hep-ex/0207026.

[74] I. Arsene *et al.*, "Inclusive Jpsi production cross-section in pp collisions at 5 TeV".
http://alice-notes.web.cern.ch/node/836. 2018.11.03.

[75] **ALICE**, Data Preparation Group, "DPG-AOT ITS-TPC matching systematics".
http://aliceinfo.cern.ch/. 2018.10.10.

[76] Y.-Q. Ma and R. Venugopalan, "Comprehensive Description of J/ψ Production in Proton-Proton Collisions at Collider Energies", *Phys. Rev. Lett.* **113** (2014), no. 19, 192301, arXiv:1408.4075.

[77] **PHENIX**, A. Adare *et al.*, "J/ψ Production vs Centrality, Transverse Momentum, and Rapidity in Au+Au Collisions at $\sqrt{s_{NN}} = 200$ GeV", *Phys. Rev. Lett.* **98** (2007) 232301, arXiv:nucl-ex/0611020.

[78] **CDF**, D. Acosta *et al.*, "Measurement of the J/ψ meson and $b-$hadron production cross sections in $p\bar{p}$ collisions at $\sqrt{s} = 1960$ GeV", *Phys. Rev.* **D71** (2005) 032001, arXiv:hep-ex/0412071.

[79] **ALICE**, B. Abelev *et al.*, "Inclusive J/ψ production in pp collisions at $\sqrt{s} = 2.76$ TeV", *Phys. Lett.* **B718** (2012) 295–306, arXiv:1203.3641, [Erratum: Phys. Lett.B748,472(2015)].

[80] **ALICE**, K. Aamodt *et al.*, "Rapidity and transverse momentum dependence of inclusive J/ψ production in pp collisions at $\sqrt{s} = 7$ TeV", *Phys. Lett.* **B704** (2011) 442–455, arXiv:1105.0380, [Erratum: Phys. Lett.B718,692(2012)].